Multiband Observations of Recurrent Novae

Michael Philip Maxwell

A thesis submitted in partial fulfilment
of the requirements for the degree of
Doctor of Philosophy

Jeremiah Horrocks Institute for Mathematics, Physics, and Astronomy
School of Computing, Engineering, and Physical Sciences
University of Central Lancashire

April 2014

Declaration

The work presented in this thesis was carried out in the Jeremiah Horrocks Institute for Mathematics, Physics, and Astronomy, School of Computing, Engineering, and Physical Sciences, University of Central Lancashire. Unless otherwise stated it is the original work of the author.

While registered for the degree of Doctor of Philosophy, the author has not been a registered candidate for another award of the University. This thesis has not been submitted in whole, or in part, for any other degree.

Abstract

Recurrent novae are binary systems which undergo outbursts due to a thermonuclear runaway on a timescale of decades. Two systems, U Scorpii and RS Ophiuchi, are the main focus of this thesis having gone into outburst in 2010 and 2006 respectively. Optical and near-IR spectroscopy of U Sco obtained with facilities including the Liverpool Telescope, the Very Large Telescope, and the Southern African Large Telescope, as well as ultra-violet and optical spectroscopy of RS Oph obtained with the Ultra-Violet and Optical Telescope, are presented here. Observations of U Sco obtained in outburst are used to determine the helium abundance of the ejecta, with observations in quiescence used to constrain the nature of the companion star and the accretion disc. Observations of RS Oph are used to produce lightcurves of the decline from maximum to the post-outburst minimum.

Analysis of optical and near-IR spectra following the 2010 outburst of U Sco leads to the determination of the reddening and the helium abundance. The reddening is found to be E(B-V) = 0.17 ± 0.14, consistent with previous estimates. The helium abundance, N(He)/N(H), is determined to be 0.122 ± 0.018, lower than previous estimates and suggesting that the companion is not helium rich.

The fitting of model stellar atmospheres to observations of U Sco in quiescence, obtained ∼18-30 months after the 2010 outburst, constrains the effective temperature of the companion and indicates that it is a cool F or hot G star. The accretion disc is found to be still in a state of development until at least ∼18 months after outburst, contrary to previous studies. The strength of the He II 4686Å line in quiescence is found to be consistent with a high mass white dwarf accreting solar-abundance material at a high rate. The He line strengths do not require an overabundance of helium, as has been previously suggested, consistent with the solar abundance of helium found in the ejecta of the 2010 outburst.

UVOT observations of RS Oph following the 2006 outburst are used to produce B and u' lightcurves of the decline to minimum. These lightcurves are used in conjunction with published V and B lightcurves to show the change in the colour of the system throughout the outburst. Spectra of RS Oph show the spectroscopic evolution during the initial decline, plateau, final decline, and post-outburst minimum phases.

SALT spectra obtained during the late decline phase of the 2011 outburst of a third recurrent nova, T Pyxidis, are used to derive a helium abundance of $N(\mathrm{He})/N(\mathrm{H}) = 0.161 \pm 0.013$, approximately twice the solar value. Very strong [O III] lines are also detected.

Contents

List of Tables

List of Figures

Acknowledgements

There are many people I would like to thank for their support and friendship throughout the last three and a half years. First of all I would like to thank Mark and Stew for their supervision. Mark's day to day advice on all things science was invaluable in teaching me all I know about novae and spectra, with Stew's watch over the direction of the project keeping it on the right track.

My time in Preston would have been a lot less enjoyable without Gareth, Caroline, Brad, Kate, and all the other sociable students, staff, and visitors who came and went throughout my time here. Their constant willingness to go to the pub was greatly appreciated.

I would never have got as far as starting a Ph.D. without the support of my parents and all the people in Manchester who helped me get my undergraduate degree.

Last but certainly not least I owe a huge amount of thanks to Nicky. From getting me up in the morning to chats about science and generally making each day better than it would otherwise have been, I count myself extremely lucky to have had her love and support over the last two and a half years.

Chapter 1

Introduction

Recurrent novae are some of the most unusual and important stellar phenomena in the Galaxy, the outbursts of which have implications for nuclear physics, chemical evolution studies of galaxies, and binary evolution; they are also a potential answer to the supernova progenitor problem for SN Ia types. Recurrent novae are related to classical novae, although there are only 10 confirmed recurrents in the Galaxy (Schaefer 2010). This introduction will include a review of recurrent and classical novae both in outburst and quiescence, a discussion of the physical processes involved in the outburst mechanism, and an in-depth look at the properties of the recurrents U Scorpii and RS Ophiuchi. Chapter 2 will cover the 2010 outburst of U Scorpii. Chapter 3 covers U Sco in quiescence. In Chapter 4 the return to quiescence of RS Ophiuchi following the 2006 outburst and subsequent observations are examined, together with observations of the 2011 outburst of T Pyxidis. Chapter 5 includes a review of the main results and possible directions for future research.

1.1 Overview of novae

Novae are binary systems in which a white dwarf (WD) accretes matter from a companion star (Webbink et al. 1987). The white dwarf can be characterised as either CO or ONe depending on its composition, with ONe dwarfs being less common since they evolve from massive stars (Gil-Pons et al. 2003). The matter stripped from the companion reaches the surface of the white dwarf via an accretion disc. This matter then builds up on the surface of the white dwarf until a critical pressure and density are reached, at which point a thermonuclear runaway occurs resulting in an outburst of material and electro-magnetic radiation (Starrfield 2008). This process repeats on a timescale dependent on the mass of the white dwarf. For recurrent novae this timescale is of the order $10 - 100$ years (Schaefer 2010); for classical novae it is of the order 10^5 years (Townsley & Bildsten 2005). In this section the properties of both recurrent and classical novae will be examined from an observational and theoretical perspective.

1.2 Star formation

The properties of a binary system are defined by the stars which make up the system: therefore it is crucial to understand the processes by which these stars are formed. Possible mechanisms for the formation of close binary systems (binary separation $\lesssim 1\,\mathrm{AU}$) are reviewed by Bonnell (2001) and include fission, capture, and fragmentation. For the fission mechanism it was suggested that a protostar could split into two distinct objects as it contracts and spins up. However simulations have shown that a circumstellar disc is formed instead (Bonnell 1994). In the capture scenario two stars, which formed independently, become locked in a binary orbit as they pass each other and are slowed down by a dense medium; this can be either a third star, a circumbinary disc, or the two stars can pass close enough to each other that tidal interactions occur. Finally, in the fragmentation scenario a collapsing body splits in two before reaching an equilibrium state (as happens in the fission scenario). In order for this to happen there must be two or more bodies within the collapsing cloud with a mass exceeding the Jeans mass (Jeans 1928) as defined by

$$M_J = \left(\frac{5R_gT}{2G\mu}\right)^{3/2}\left(\frac{4\pi\rho}{3}\right)^{-1/2}, \tag{1.1}$$

where R_g is the gas constant, T is the temperature, G is the gravitational constant, μ is the mean molecular weight, and ρ is the density. Bonnell (2001) also notes that it is possible to produce close binary systems through the evolution of an existing system rather than producing the system in situ. If a system forms as a wide binary with a circumbinary disc, then the system can spiral in through the transport of angular momentum to the circumbinary disc. Another possibility is that a system with multiple stars forms but then disintegrates, generally leaving the two most massive stars as a binary system (Sterzik & Durisen 1998).

1.3 Classical novae

Classical novae have been reviewed in detail by Warner (2003) and Bode & Evans (2008) amongst others. Records of observations of nova and supernova outbursts stretch back to several centuries B.C. in Chinese records (Bode & Evans 2008), with nova outbursts being observed at a rate of $1.37\,\mathrm{yr}^{-1}$ in the 20th century (Dürbeck et al. 1993). However many nova outbursts are missed due to factors such as interstellar extinction and selection effects such as weather, seasonal gaps, and rapid declines from maximum (Warner 1989). Estimates of the Galactic nova rate range from $29 \pm 17\,\mathrm{yr}^{-1}$ (Ciardullo et al. 1990) to $73 \pm 24\,\mathrm{yr}^{-1}$ (Liller & Mayer 1987). The nova rate in M31 has been estimated as $35^{+15}_{-12}\,\mathrm{yr}^{-1}$ by Darnley et al. (2008). Several large surveys of novae have now been conducted (see Shafter et al. (2011) or Walter et al. (2012) for examples), allowing nova outbursts to be classified both photometrically and spectroscopically. Compared to their recurrent counterparts classical novae have higher ejecta masses, lower white dwarf masses, lower mass accretion rates, and longer inter-outburst intervals. Amplitudes of nova outbursts tend to be in the range 8-12 magnitudes in the V band, though systems such as

CP Pup have been reported to have had outbursts with an amplitude as high as 16 mags.

Each nova system can be further classified depending on the orbital period, companion star, and the strength of the magnetic field, if detected. Short period novae are cataclysmic variables, whereas long period novae with giant secondaries are symbiotic stars. Cataclysmic variables (CVs) are binary systems with a period of minutes to hours and have main sequence companion stars. Symbiotic stars have orbital periods of years and have Roche-lobe filling giant companions. A schematic diagram of a CV can been seen in Fig 1.1; symbiotic systems are similar but with a giant rather than main sequence companion. CVs with strong magnetic fields are known as polars; those with weaker magnetic fields are intermediate polars. In the case of polars an accretion disc is not formed, as the magnetic field is strong enough that the accretion stream is directed onto the poles of the white dwarf. For intermediate polars the magnetic field is strong enough to disrupt the accretion disc, but not sufficiently strong to stop a disc forming, resulting in a warped disc as can be seen in Fig 1.2.

1.3.1 Photometric development

Photometrically novae are divided by speed class, with the number of days a nova outburst takes to fade from peak by either two (t_2) or three (t_3) magnitudes being the common metrics by which the speed of a nova is measured. The definitions of Gaposchkin (1957) are commonly used for both recurrent and classical novae. Gaposchkin (1957) classified outbursts as very fast, fast, moderately fast, slow, or very slow as shown in Table 1.1.

There is a relation between the absolute visual magnitude of the nova at maximum and the rate of decline (MMRD relation): brighter novae decline faster, as can be seen for Galactic novae in Figure 1.3 (Downes & Duerbeck 2000). The empirical

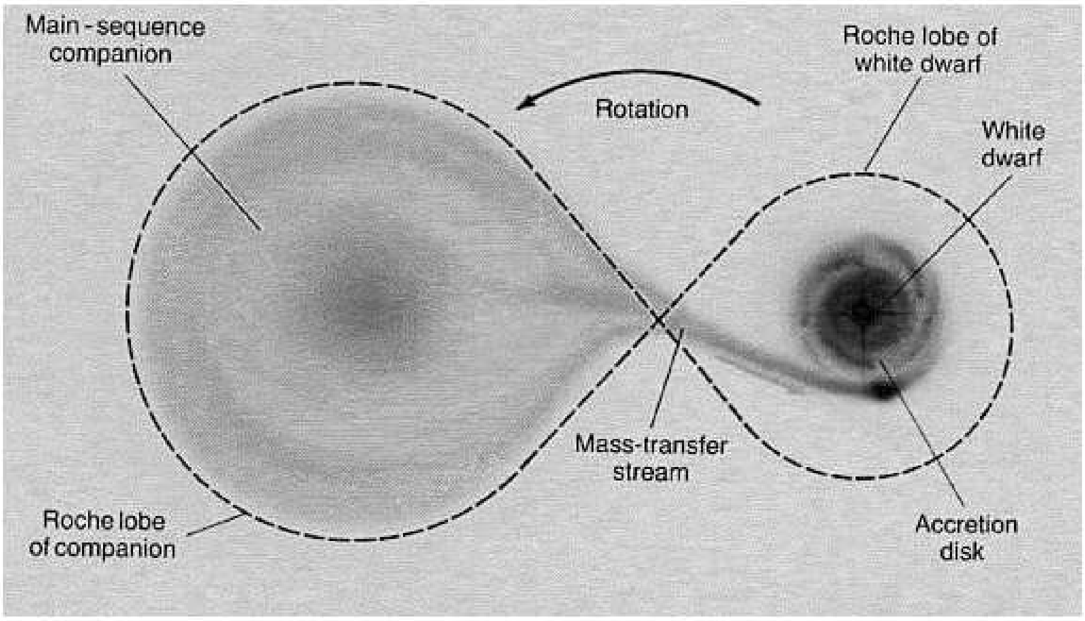

Figure 1.1: Schematic diagram of a cataclysmic variable system. Image courtesy of Penn State University (http://www2.astro.psu.edu/users/rbc/a1/lec16n.html).

Speed class	t_2 (days)
very fast	$\leq$10
fast	11-25
moderately fast	26-80
slow	81-150
very slow	151-250

Table 1.1: Nova speed classes as defined by Gaposchkin (1957)

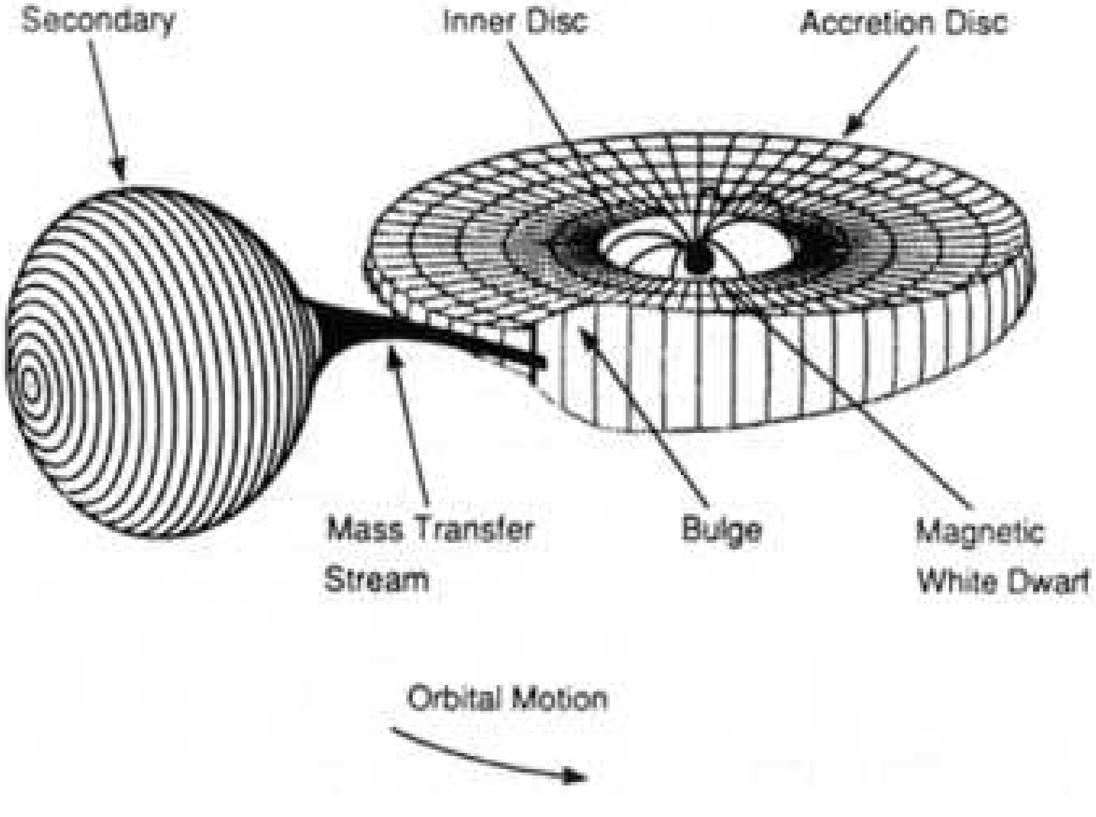

Figure 1.2: Schematic diagram of an intermediate polar system. Image courtesy of NASA (http://heasarc.gsfc.nasa.gov/docs/objects/cvs/cvstext.html).

fit to the data in Figure 1.3 is given by

$$M_V = -8.02 - 1.23 \arctan \frac{1.32 - \log t_2}{0.23}, \tag{1.2}$$

where M_V is the magnitude at maximum and t_2 is the time it takes for the nova to fade by two magnitudes from peak. Darnley et al. (2006) observed 20 novae in M31 with Sloan r′ and i′ filters and produce good fits to the MMRD in both filters. Other MMRD relationships have been derived by Capaccioli et al. (1989),

$$M_V = -7.89 - 0.81 \arctan \frac{1.32 - \log t_2}{0.19}, \tag{1.3}$$

Cohen (1985),

$$M_V = -10.70 + 2.41 \log t_2, \tag{1.4}$$

and Arp (1956) (Figure 1.4). A scatter of $\sim 0.5 - 1$ mag is typical indicating that either there is not a tight correlation or that accurately determining either the maximum magnitude or the rate of decline is difficult, particularly in the case of fast novae (Darnley et al. 2006). Fast, faint novae, which were predicted to exist by Yaron et al. (2005), are now being found (Kasliwal et al. 2011), casting further doubt on the validity of the MMRD relation. Schaefer (2010) determines the distance to each recurrent nova using the MMRD relationship of Downes & Duerbeck (2000). However several of the distances derived place the nova outside of the Galaxy and the author notes that large systematic errors are likely; it is unclear how useful the MMRD is in determining the distance to a recurrent nova. Some recurrents, including T Pyx (Sokoloski et al. 2013), RS Oph (Hjellming et al. 1986), and U Sco (Schaefer 2010), have independent distance estimates.

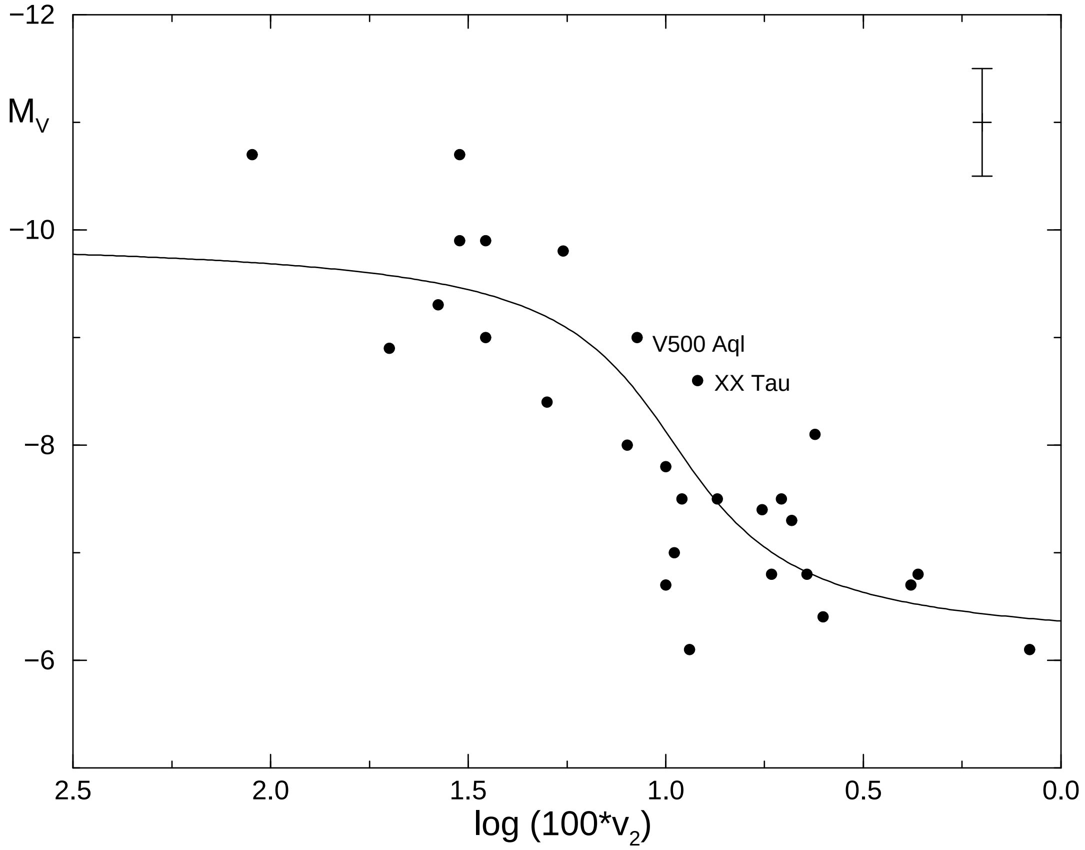

Figure 1.3: MMRD relation from Fig. 17 of Downes & Duerbeck (2000). Typical error bar shown in upper-right corner. V_2 is the average daily decline in mags from maximum to 2 mags from maximum.

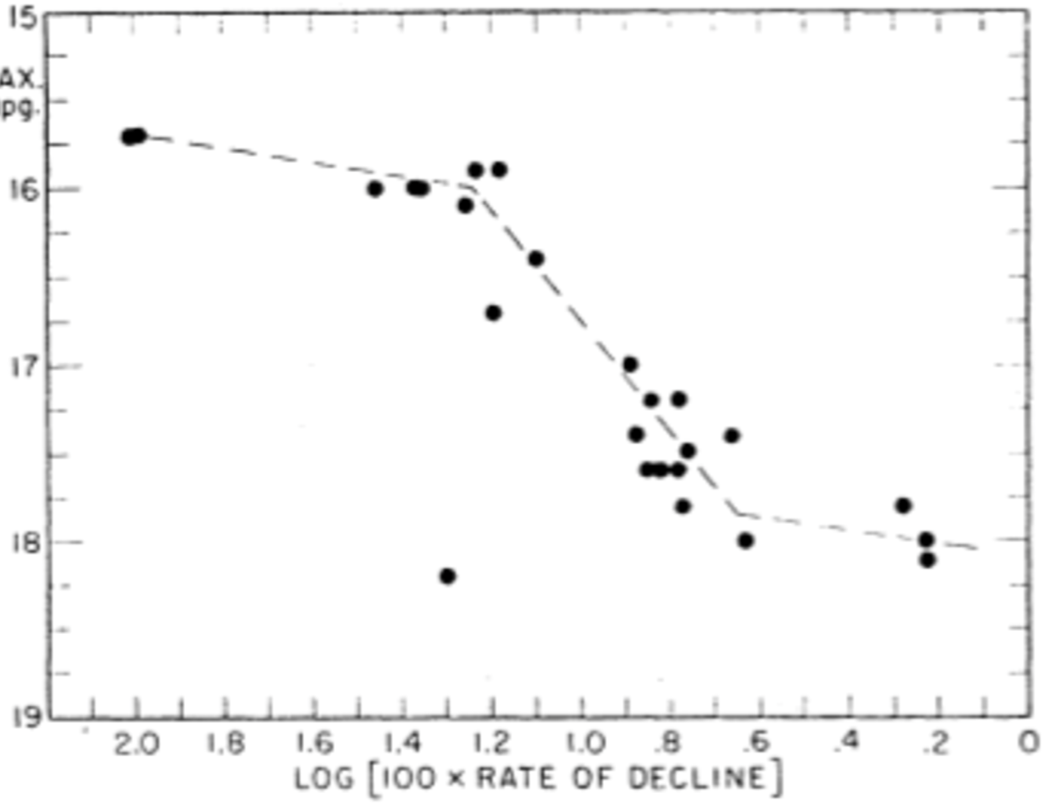

Figure 1.4: MMRD relation from Arp (1956)

1.3.2 Spectroscopic development

Novae are classified spectroscopically in terms of the emission lines present in their outburst spectra. Williams et al. (1981) defined two classes, Fe II or He/N, depending on the dominant species in the ejecta in the early stages of the outburst. He/N novae tend to evolve faster than Fe II novae (Williams et al. 1981). Some novae, such as the recurrent nova T Pyx, have displayed both He/N type and Fe II type behaviour (Imamura & Tanabe 2012). In the case of T Pyx the spectrum evolves from He/N type to Fe II type during the pre-maximum stage; other novae such as V5558 Sgr have also been seen to display this behaviour (Imamura & Tanabe 2012). The width of these emission lines is linked to the speed class of the nova; the width of a line is determined by the velocity of the material from which that line arises, with faster novae having higher velocity (larger width) emission lines.

Outbursts of novae tend to evolve through four phases: neutral, auroral, coronal, and nebular (Williams 1990), although neon novae, which are characterised by strong forbidden [Ne II] lines in the infra-red (IR; Gehrz et al. 1985), evolve directly from the neutral to the nebular phase.

Coronal lines are formed by highly ionised ions formed in high temperature environments, and are so named due to lines fitting this description often being observed in the solar corona. An informal definition of coronal emission is given by Greenhouse et al. (1990) as emission from ground-state transitions in species with an ionisation potential of over 100 eV. Auroral lines are lines such as [O III] and [N II] that are frequently seen in observations of aurorae on Earth. Nebular lines are lines which are often observed in the spectra of emission nebulae. Permitted lines are formed via dipole transitions as defined by the selection rules of quantum mechanics; which transitions are allowed by these rules will vary from atom to atom and from molecule to molecule. Forbidden lines are formed via improbable quadropole or magnetic dipole transitions, and are only observed in low density environments as these states will become collisionally de-excited in high density environments.

Williams et al. (1991) then builds on this and defines coronal (C), permitted-line (P), auroral (A), and nebular (N) phases. Phase C is the coronal phase and occurs when forbidden [Fe X] 6375Å emission is present and stronger than the forbidden [Fe VII] 6087Å emission. The coronal phase can also be characterised by strong Si lines in the IR, as observed in V4643 Sgr (Ashok et al. 2006). Phase P is the permitted-line phase and is defined as when the strongest observed non-Balmer line is from a permitted transition, as is the case in the spectra of the 2010 outburst of U Sco which are presented in Chapter 2. Phase A is the auroral phase and occurs whenever a forbidden auroral line has a greater flux than the strongest observed non-Balmer permitted line as seen in V4743 Sgr (Morgan et al. 2003). Finally the spectrum is in phase N if it is not in phase C or A and the strongest observed non-Balmer line is a forbidden nebular line, as observed in T Pyxidis (Shore et al. 2013b). Forbidden lines only form in very low density environments; the critical density for the commonly observed [O III] 5007Å line is $\sim10^{6}\,\mathrm{cm}^{-3}$ (Appenzeller & Oestreicher 1988), whereas for comparison the density of air on Earth is $\sim10^{19}\,\mathrm{cm}^{-3}$. Each of these phases can then be further defined based on the strength of the strongest non-Balmer line, which will usually be due to He, C, N, O, Ne, Ca, or Fe.

Recurrent novae are seen to enter a high ionisation phase within one month of outburst where either [Fe X] or He II lines are remarkably strong. Williams et al. (1991) notes that the evolution from one stage to the next is determined by changing densities and the thinning out of the ejecta in the nova envelope, with some novae not experiencing all four phases.

The usefulness of this classification system has come into question over the years as more and more new novae are observed that do not fit into this classification scheme, either because they skip some number of phases or have prominent lines which are not included within this scheme. Also, understanding the physics behind the formation of emission lines and their evolution, rather than engaging in debates on nomenclature and taxonomy, leads to a better understanding of nova systems.

1.4 Recurrent novae

The ten confirmed Galactic recurrents, summarised in Table 1.2, can be placed into three groups: T Pyx type, U Sco type, and RS Oph type. T Pyx type systems have orbital periods of a few hours and have main sequence companions, U Sco types have orbital periods of a few days and, in order for Roche-lobe overflow to occur, must have subgiant companions (Anupama & Dewangan 2000; Johnston & Kulkarni 1992), and RS Oph types have orbital periods of ∼1 year and giant companions. Other systems such as KT Eri (Jurdana-Šepić et al. 2012), and some extra-galactic systems such as Nova LMC 2007 (Bode et al. 2009), are suspected to be recurrent. CP Pup is not suspected to be recurrent, although it is suspected to be an intermediate polar (Mason et al. 2013). Nova outbursts occur in several stages: the rise to maximum brightness, an initial decline, and a final decline to the pre-outburst magnitude, as shown schematically in Figure 1.5. A plateau phase, a period of very slow decline during which the V band magnitude drops by less than one magnitude, can also occur between the initial and final declines.

1.5 Binary evolution

The evolution of a binary system up to the point that it undergoes a nova outburst plays a major part in determining the characteristics of the outburst. There are several conditions which must be fulfilled in order for a binary system to evolve into a nova; for example these conditions are different for long period RS Oph type recurrent nova systems compared to the more compact U Sco and T Pyx type systems. The conditions for compact recurrent nova systems, as discussed by Bode

Nova	First observed outburst	No. observed outbursts	Orbital period (days)	Speed class	Distance
U Sco	1863 (Pogson 1865)	10	1.23	Very fast	12 kpc
T CrB	1866 (Walter 1867)	2	228	Very fast	0.9 kpc
T Pyx	1890 (Pickering 1913)	6	0.076	Moderately fast	3.5 kpc
RS Oph	1898 (Pickering 1905)	8	457	Very fast	1.6 kpc
V2487 Oph	1900 (Pagnotta et al. 2009)	2	1.0	Very fast	12 kpc
CI Aql	1917 (Reinmuth 1925)	3	0.62	Fast	5 kpc
IM Nor	1920 (Bailey 1920b)	2	0.102	Moderately fast	3.4 kpc
V745 Sco	1937 (Plaut 1958)	2	510	Very fast	7.8 kpc
V394 CrA	1949 (Erro 1949)	2	1.52	Very fast	10 kpc
V3890 Sgr	1962 (Dinerstein & Hoffleit 1973)	2	519.7	Very fast	7 kpc

Table 1.2: Known Galactic recurrents. Data from Schaefer (2010).

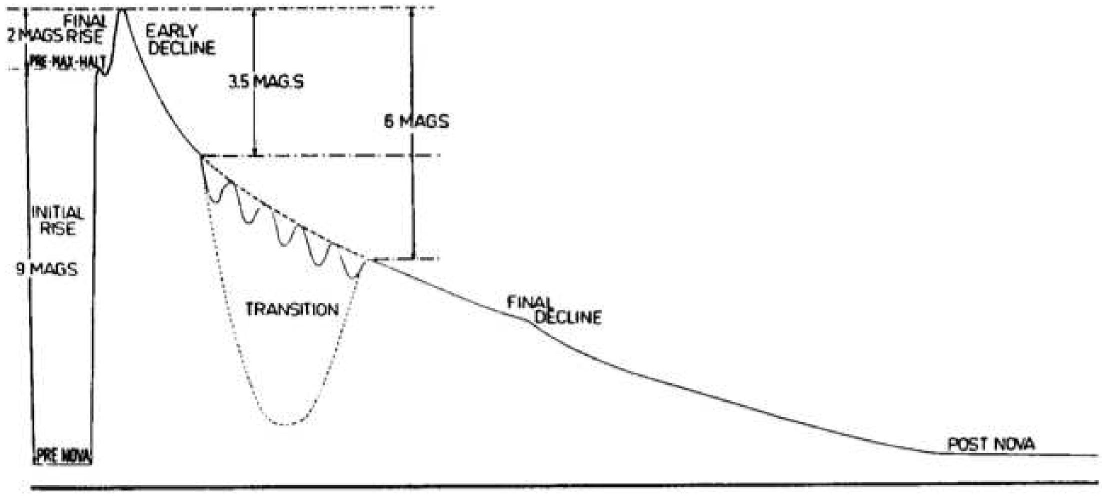

Figure 1.5: Schematic diagram of a nova lightcurve from McLaughlin (1960).

& Evans (2008), include: that the mass of the primary is high enough such that it will develop a H/He depleted core within the Hubble time; that the core evolves to this state before the primary fills its Roche lobe; and that a common-envelope phase occurs when the primary fills its Roche lobe, leading to a reduction in the orbital separation allowing mass transfer to occur and a nova outburst to happen within the Hubble time.

In order for any nova outburst to occur within the Hubble time the mass transfer rate must be $\geq 10^{-11}\,\mathrm{M}_{\odot}\,\mathrm{yr}^{-1}$. This condition is clearly fulfilled in recurrent novae since several outbursts have been observed.

The conditions for the formation of longer period symbiotic stars (WD + red giant systems) are different from the conditions required for the formation of a cataclysmic variable. In the case of these longer period systems, such as RS Oph, one of the following three scenarios is required: that the masses of the two stars are close enough that the binary separation does not change significantly upon the Roche lobe becoming filled; that the primary becomes a white dwarf without filling its Roche lobe; or that a common-envelope phase does not occur due to the primary becoming an AGB star with a dusty wind. A common-envelope phase would result in the binary orbit shrinking and a shorter period binary being formed.

1.6 Accretion

Accretion is central to the nature of novae; it is the mechanism by which the primary gains mass and it is primarily the accreted material that is ejected in the outburst. Accretion can be via either Roche-lobe overflow (RLO) or wind accretion. In the RLO case the companion fills its Roche-lobe and matter is transferred through the inner Lagrangian point, L1, and forms an accretion disc around the primary. If the companion does not fill its Roche-lobe, but it has a wind, then the primary accretes from the wind and a disc is also formed. Both wind accretion (as in RS Oph; Walder et al. 2008) and RLO (as in U Sco; Thoroughgood et al. 2001) are capable of producing outbursts on a timescale of decades. The matter loses angular momentum as it passes through the disc until it reaches the inner edge at which point it is deposited onto the WD; this inner edge is known as the boundary layer. For accretion via RLO the point at which the accretion stream strikes the disc is known as the bright spot; it is not clear if a bright spot forms in the case of accretion via a wind (Zamanov et al. 2010). If a sufficiently strong magnetic field is present, as has been tentatively suggested for the recurrent nova T Pyx (Patterson et al. 1998; Shahbaz et al. 1997), then material is deposited onto the poles of the primary. During an outburst the accretion disc is destroyed but then reforms; the resumption of optical flickering, as defined by Gromadzki et al. (2006), is an indicator of accretion having restarted (Worters et al. 2010). Accretion discs grow to fill the space between the primary and the companion, although whether these discs grow from the centre to the outer edge (inside out) or vice-versa (outside in) is not certain. Accretion discs can vary on timescales of hours; it is discs that are largely responsible for the varying brightness in quiescence, both photometrically and spectroscopically, due to discs dominating the quiescent light (e.g. $L_{disc} \sim 50 - 150\,L_{\odot}$; Zamanov 2011).

1.7 Novae in outburst

The characteristics of a nova outburst vary depending on factors such as the speed of the nova, the composition of the white dwarf, and the metallicity of the accreted material. Nova outbursts are powered by thermonuclear runaways on the surface of the primary (Starrfield 2008). The ejecta are optically thick in the initial outburst state, before becoming optically thin on a timescale linked to the speed of the nova.

1.7.1 Physical processes

In a thermonuclear runaway (TNR) hydrogen-rich material builds up in a layer on the surface of the white dwarf. This hydrogen undergoes nuclear fusion via the proton-proton chain until the pressure, density, and temperature in the accreted layer reach critical values such that the energy from nuclear fusion cannot be effectively radiated away (Townsley 2008). The increase in temperature, which reaches $\geq 10^8\,\mathrm{K}$, causes nuclei capable of doing so to capture a proton. This causes them to become β^+ unstable resulting in non-solar abundance ratios in the ejecta due to these nuclei limiting the rate at which energy can be generated (Starrfield 2008). Some of the nuclei involved in the CNO cycle, which becomes the dominant form of energy generation once temperatures reach $\sim 2\times10^6\,\mathrm{K}$, such as ^{14}O and ^{13}N, have long half-lives which is the cause of this upper limit as these nuclear processes are independent of temperature. The energy release from β decays then causes the accreted material to be ejected. A full description of a thermonuclear runaway is provided by Starrfield (2008) and is summarised below.

The rate of energy production in the TNR is limited only by the half-lives of nuclei which undergo β^+ decay and the abundances in the envelope at temperatures above $10^8\,\mathrm{K}$. Once the temperature has exceded this value most nuclei which can capture a proton (such as ^{12}C, ^{13}C, and ^{14}N), do so, with the rate of energy generation capable of reaching 10^{13} to 10^{15} $\mathrm{erg\,g^{-1}\,s^{-1}}$ (10^9 to $10^{11}\,\mathrm{W\,kg^{-1}}$) depending on the abundances. Isotopic ratios of C, N, O, Ne, and Mg in the ejected material are different from those found in studies of equilibrium burning of these elements. This is due to convection bringing isotopes of these elements to the outer layers of the envelope, where the hydrodynamic expansion time is shorter than the half-lives of these isotopes, which decay when the temperature in the envelope decreases to the point that no further proton captures can occur. These nuclei decay throughout the envelope which flattens the temperature gradient and turns off convection, with the energy from these decays eventually causing the material to be ejected from the surface of the WD.

In a typical classical nova outburst the ejected mass is $\sim 10^{-4}\,\mathrm{M}_{\odot}$ (Gehrz et al. 1998; Heywood et al. 2005; Hack et al. 1993); generally this value is much lower for recurrent nova outbursts. Nova ejecta masses can be estimated using radio (Heywood et al. 2005), X-ray (Vaytet et al. 2011), and optical (Shore et al. 2013a) observations. One important factor is if dredge-up occurs during the inter-outburst period; dredge-up is where material from the underlying white dwarf mixes with the accreted material and is then involved in the TNR and resultant outburst. Starrfield et al. (2012) state that a white dwarf accreting solar-abundance material always results in a TNR if there is no mixing with core material, and the lack of CNO or heavier element enrichment in recurrent nova outbursts suggests that there is no significant mixing with core material during the accretion phase. However, Mason (2011) suggests that in the case of U Sco the high Ne abundance indicates that mixing occurs with an underlying ONeMg white dwarf. Since the mass of accreted material is inversely proportional to the WD mass (MacDonald et al. 1985), and a critical pressure must be reached at the base of the accreted layer for a TNR to occur (Fujimoto 1982b,a), the critical mass (M_{crit}) and pressure (P_{crit}) required for a TNR are related by

$$P_{crit} = \frac{GM_{WD}M_{crit}}{4\pi R_{WD}^4}, \tag{1.5}$$

(Starrfield 2008) where G is the gravitational constant and M_{WD} and R_{WD} are the mass and radius of the white dwarf. Given that white dwarf masses in recurrent novae tend to be close to the Chandrasekhar limit (Thoroughgood et al. 2001; Sokoloski et al. 2006), if P_{crit} is considered constant at $\sim 10^{19}$ Pa (Starrfield 2008), then this pressure can be reached with a lower accreted mass than for classical novae where the white dwarf is less massive.

1.8 Supernova Ia progenitors

Because of the high white dwarf masses in recurrent novae, these systems are potential progenitors of Type Ia Supernovae. SNe Ia occur when a white dwarf reaches the Chandrasekhar limit, there being two main scenarios for this to occur. In the first scenario, known as the double degenerate scenario, a pair of white dwarfs with a total mass over $1.4\,M_{\odot}$ merge (Webbink 1984). In the second scenario, known as the single degenerate scenario, an accreting white dwarf builds up mass over time until it reaches the Chandrasekhar mass (Han & Podsiadlowski 2004). Recurrent novae are candidates for single degenerate progenitors, although in order for a white dwarf to become a supernova in line with the single degenerate scenario the primary must be a CO white dwarf rather than an ONe white dwarf; this is due to ONe dwarfs undergoing accretion induced collapse upon reaching the Chandrasekhar mass (Nomoto & Kondo 1991). Studies including Schaefer (2011) and Hachisu (2003) suggest that, if the underlying white dwarf is a CO dwarf, recurrent novae are good candidates for SNe Ia progenitors.

1.9 U Scorpii

U Scorpii is the most prolific recurrent nova with 10 observed outbursts, the most recent of which was in January 2010. The American Association of Variable Star Observers (AAVSO[1]) lightcurve for this outburst is shown in Figure 1.6. U Sco is found to be at a distance of 12 ± 2 kpc from the size and effective temperature of the companion star, well out of the galactic plane at a height of ∼4.5 kpc (Schaefer 2010). Distances to RS Oph type recurrents are determined in the same way by Schaefer (2010). Other methods for determining the distance to a nova include radio observations of H I absorption (RS Oph, Hjellming et al. 1986), light echoes (T Pyx, Sokoloski et al. 2013), and the use of a 3D geometrical model (CI Aql, Lederle & Kimeswenger 2003).

The nature of the binary orbit in U Sco has been discussed in detail by Schaefer & Ringwald (1995). They find the orbital period to be 1.2305631 ± 0.0000030 days with an eclipse minimum time of HJD (heliocentric Julian date) 2,447,717.6061 ± 0.0032. This is determined from 21 nights of photometry which includes several eclipses. As a high-inclination eclipsing system (i∼83 degrees, Thoroughgood et al. 2001) the orbital period of U Sco has been tightly constrained (Schaefer & Ringwald 1995); inclination is defined such that at $i=90^\circ$ the observer is in the plane of the orbit and at $i=0^\circ$ the orbit is perpendicular to the observer. During eclipses of the primary the egress is slower than the ingress; this asymmetry is attributed to the bright spot. Due to the lack of an extended minimum and the time resolution of their observations, Schaefer & Ringwald (1995) determine that if there is a total eclipse of the primary then it lasts for at most 45 minutes.

Estimates of the mass of the white dwarf have been made by Thoroughgood et al. (2001); Johnston & Kulkarni (1992) and Dürbeck et al. (1993). Thoroughgood et al. (2001) determine the white dwarf mass to be $1.55 \pm 0.24\,\mathrm{M}_\odot$ using radial

---

[1] www.aavso.org

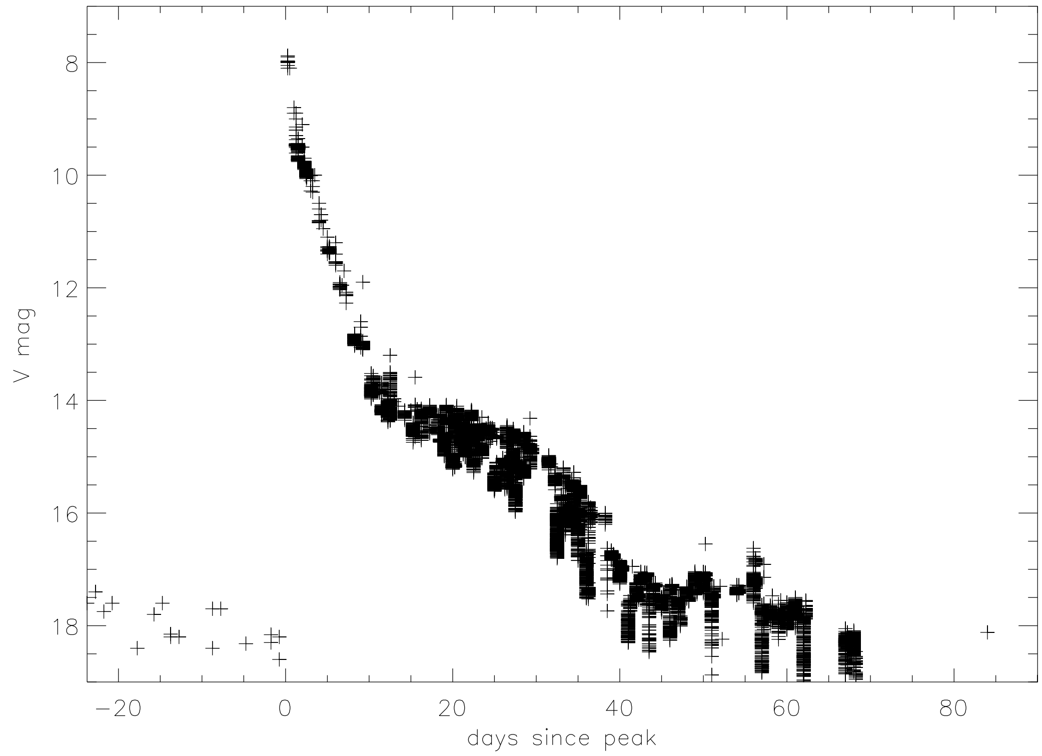

Figure 1.6: V band lightcurve of U Sco from 05/01/2010 to 22/04/2010. Data from AAVSO. Day zero is taken to be at January 28.19.

velocity measurements; they also determine the mass and radius of the companion, as discussed later. Dürbeck et al. (1993) also find a high white dwarf mass of $1.16 \pm 0.69\,\mathrm{M}_{\odot}$, whereas Johnston & Kulkarni (1992) find a low white dwarf mass of $0.23 - 0.60\,\mathrm{M}_{\odot}$; however these two works suffer from poor phase coverage and low resolution data respectively. Simulations such as those by Starrfield et al. (2012) and Hachisu & Kato (2012) have suggested that outbursts of recurrent novae are often best reproduced by models with a white dwarf mass close to the Chandrasekhar limit, therefore the mass of the white dwarf in U Sco is taken to be $1.4\,\mathrm{M}_{\odot}$ in this thesis.

The nature of the companion is much less well determined than the primary, but estimates have been made of its mass, radius, and spectral type through a variety of diagnostic tools. Thoroughgood et al. (2001) find a companion mass of $0.88 \pm 0.17\,\mathrm{M}_{\odot}$ and radius of $2.1 \pm 0.2\,\mathrm{R}_{\odot}$, indicating that the companion is evolved although they do not make an estimate of the spectral type. Hachisu et al. (1999) suggest that the companion and therefore the material accreted by the primary in this system is He-rich. Schaefer & Ringwald (1995) estimate that the companion is a G star from the colours at the minimum B band magnitude. Johnston & Kulkarni (1992) suggest a spectral type of F8 ± 2 based on the observed ratio of the strengths of calcium lines and Hδ, whereas Hanes (1985) estimates G0 ± 5V from Ca and Mg absorption features. Anupama & Dewangan (2000) use Mg, Ca, and Fe absorption features to derive a spectral type of K2. Clearly there is no consensus as to the spectral type of the companion.

Spectroscopic observations of U Sco in quiescence are not abundant. However some observations have been taken by Thoroughgood et al. (2001); Johnston & Kulkarni (1992) and Dürbeck et al. (1993). Thoroughgood et al. (2001) took 5 nights of spectra ~ 280 days after the 1999 outburst (Fig 1.8), in which the He II emission lines at 4686Å and 5411Å are prominent. Hβ is weakly in emission, and there is a complex of lines from $\sim 4900 - 5100$Å. Due to blending between all the lines in this complex the line identifications are uncertain, but the authors identify several species of O, N, and He within this wavelength region, including some forbidden lines. However Mason et al. (2012) attribute these features to multi-peaked lines of a single ion (see Fig 1.9). Detections of C IV and Mg I are also claimed, but it is not clear if these lines are definitely present. The presence of a complex of high excitation emission lines would suggest that the system has not returned to quiescence spectroscopically at this time. Dürbeck et al. (1993) obtained an optical spectrum of U Sco in 1992, five years after the outburst in 1987 (Figure 1.7). This spectrum, which covers $\sim 3800 - 5500$Å, shows fewer features. He II 4686Å is the dominant feature with Hβ and He II 5411Å also present. They also note the presence of features which can be attributed to the companion, specifically Ca II H and K lines in absorption. Mason et al. (2012) followed the 2010 outburst until 125 days after maximum (Figs 1.9 and 1.10) by which time the spectra began to resemble those of Thoroughgood et al. (2001).

Johnston & Kulkarni (1992) obtained 18 spectra on several nights throughout 1990 and 1991, again several years after the peak of the previous outburst. These spectra cover a similar wavelength range to that of Dürbeck et al. (1993) and closely resemble their observation; He II 4686Å is again the dominant feature with Hβ and He II 5411Å also present but weak. There is a clear difference between the observations of Thoroughgood et al. (2001), taken $\sim 200 - 250$ days after the previous outburst, and the observations of Dürbeck et al. (1993) and Johnston & Kulkarni (1992) which were taken 2-3 years after the previous outburst. Helium-rich ejecta were reported following the outbursts in 1979 (Barlow et al. 1981) and 1999 (Anupama & Dewangan 2000; Evans et al. 2001; Iijima 2002), with N(He)/N(H) ratios[2] of up to 4.5 suggested, indicating that helium is highly over-abundant in the ejecta.

---

[2] In this thesis He/H refers to the ratio of the number of atoms or ions, according to the context, of the two elements.

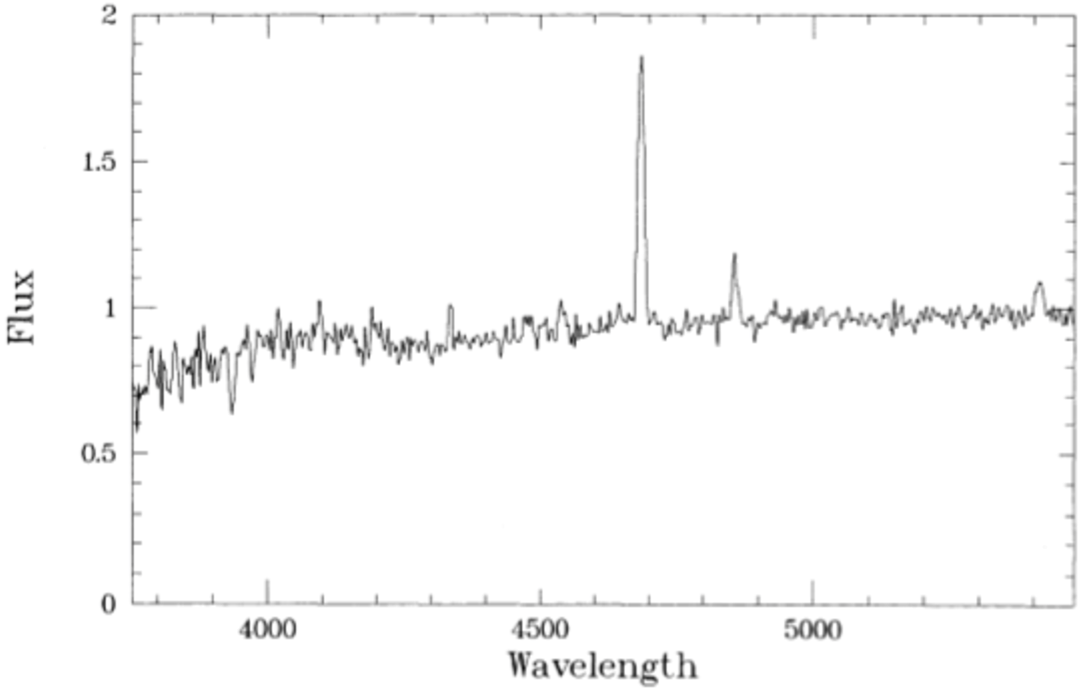

Figure 1.7: Spectrum of U Sco from Dürbeck et al. (1993) taken in 1992.

However, the wide range of values combined with incomplete wavelength or temporal coverage means further work is required to properly constrain the ejecta abundances.

1.10 RS Ophiuchi

RS Ophiuchi has undergone 8 recorded outbursts, most recently on 2006 February 12.83 (Hirosawa et al. 2006) which is taken as day 0 for this outburst. Adamakis et al. (2011) use a Bayesian analysis of the long-term lightcurve of RS Oph from 1933 to 2008 to confirm the 1945 outburst initially suggested by Oppenheimer & Mattei (1993). The white dwarf in this system has a mass close to the Chandrasekhar limit ($\sim 1.4\,\mathrm{M}_\odot$), with the companion star being a red giant of spectral type M2-III (Rosino et al. 1982) with a mass of 0.60 - $0.80\,\mathrm{M}_\odot$ (Brandi et al. 2009). Distance estimates to RS Oph are reviewed by Barry et al. (2008), with the distance derived by Hjellming et al. (1986) of 1.6 kpc being most commonly used. RS Oph has

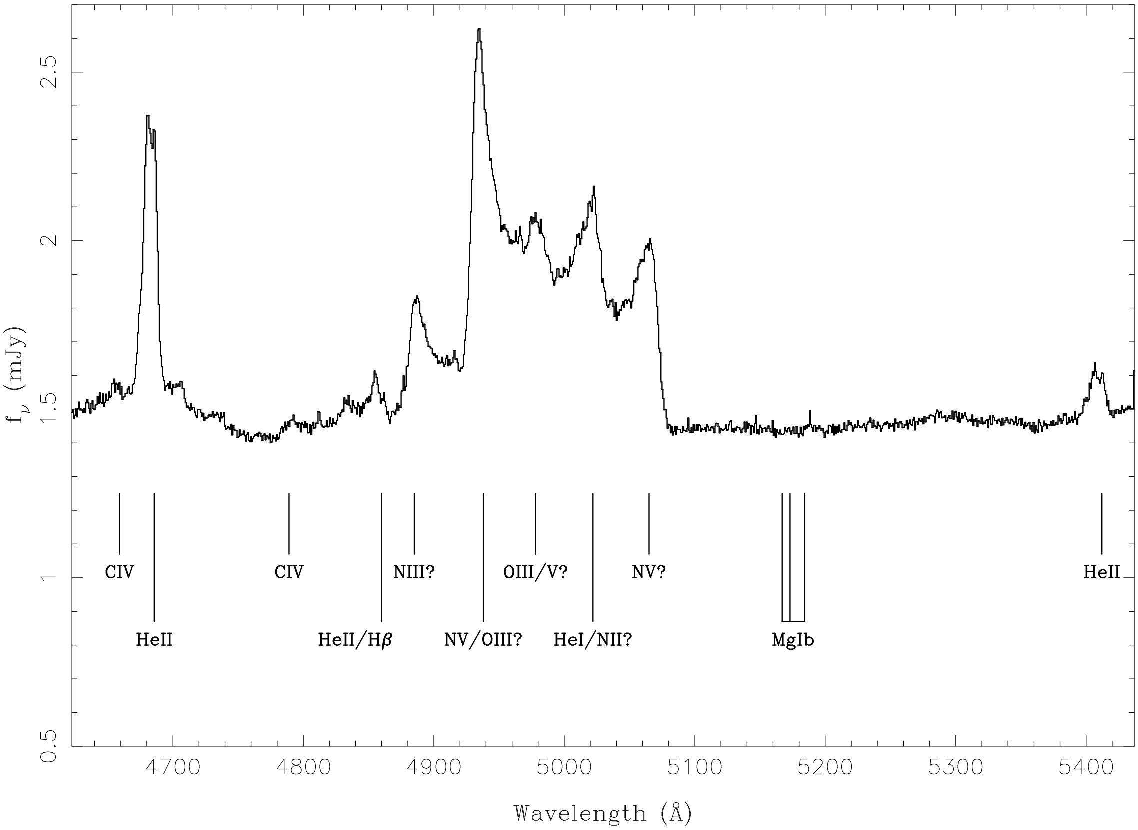

Figure 1.8: Phase averaged spectrum of U Sco from Thoroughgood et al. (2001) taken ∼280 days after the 1999 outburst. Note that $1\,\mathrm{mJy} = 10^{-29}\,\mathrm{Wm^{-2}Hz^{-1}}$.

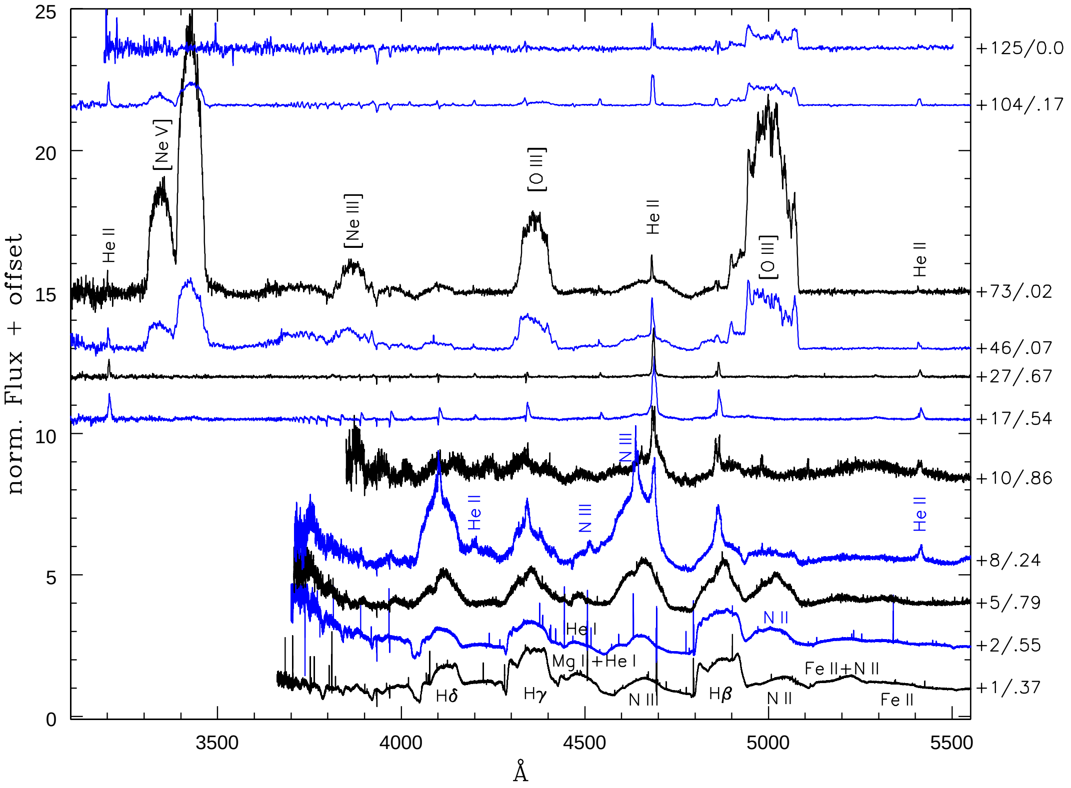

Figure 1.9: Spectra of U Sco from Mason et al. (2012) taken up to 125 days after the 2010 outburst. Labels are the number of days since the optical peak and the orbital phase.

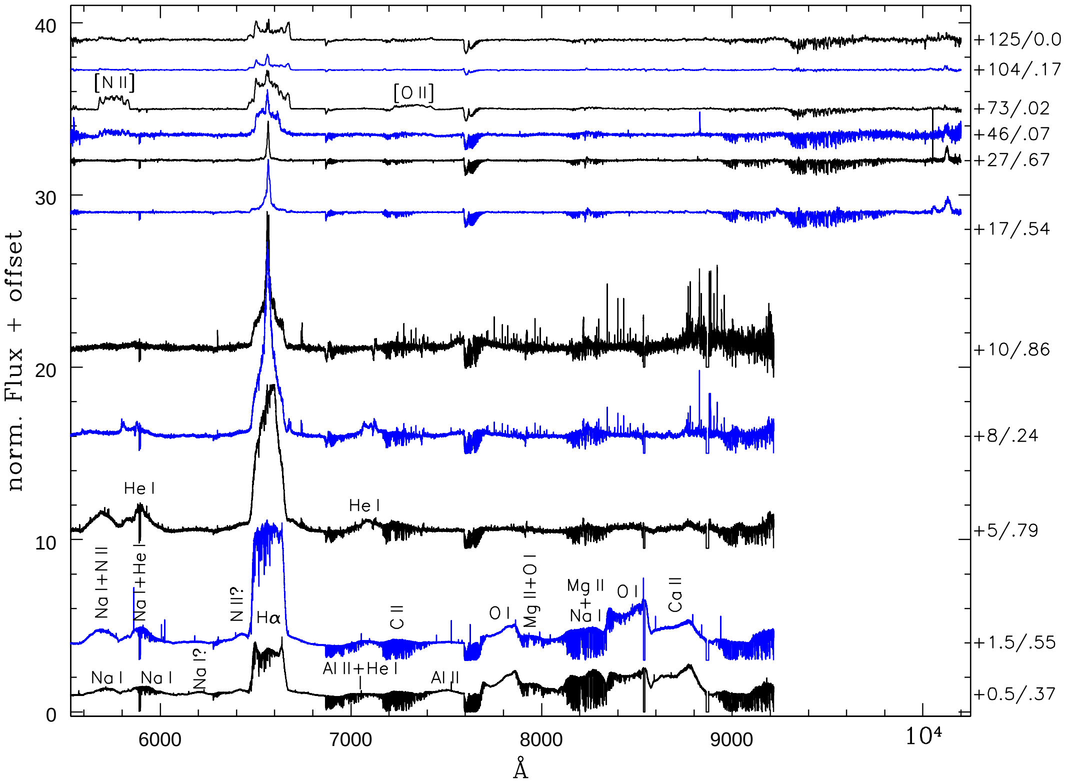

Figure 1.10: Spectra of U Sco from Mason et al. (2012) taken up to 125 days after the 2010 outburst. Labels are the number of days since the optical peak and the orbital phase.

an inclination of $39^{\circ}{}^{+1}_{-10}$ (Ribeiro et al. 2009) and an orbital period of ∼460 days (Dobrzycka & Kenyon 1994). Because of the nature of the companion in this system there are several differences between the outburst properties in RS Oph compared to systems like U Sco; collisions between the outburst ejecta and the red giant wind cause shocks to occur, resulting in hard X-rays being emitted (Bode et al. 2006). Interactions between the ejecta and the red giant wind also caused radio emission to be detected shortly after the optical peak (Eyres et al. 2009). The interactions between nova ejecta and a wind are modelled by Moore & Bildsten (2012) who determine the radius and velocity of shocks in RS Oph type systems.

The radio emission in RS Oph has both thermal and non-thermal components in a bi-polar outflow, with jets also being observed (Eyres et al. 2009; Rupen et al. 2008; Sokoloski et al. 2008; O'Brien et al. 2006). Sokoloski et al. (2008) suggest that the jets come from one of three possible sources: either the ejecta expand into an inhomogeneous environment, the mass ejection is initially asymmetric, or the jets are driven by a collimated outflow. Rupen et al. (2008) note that the angular size evolution of the radio emission matches the velocities derived from X-ray and IR observations and derive a distance estimate of 2.45 kpc. Eyres et al. (2009) show that the radio lightcurve had two peaks: the first on day 13 and the second on day 40 after a decline from the initial radio peak; an ejected mass estimate of $4\pm2\times10^{-7}\,\mathrm{M}_{\odot}$ is also derived.

Hounsell et al. (2010) observed a pre-maximum halt in the rise to optical maximum of RS Oph; a pre-maximum halt is a dip in the optical lightcurve of a nova as it approaches maximum (see Fig 1.5). A change in the mass loss rate is given as a possible explanation, with an alternative explanation being a pre-nova UV flash due to the recession of convection from the photosphere (Y. Hillman, private communication). Iijima (2009) obtained optical spectra covering the first 100 days of the 2006 outburst, observing previously unseen phenomena such as a rapid rise in the strength of He I lines and splitting of narrow emission line components. Bode et al. (2007) obtained Hubble Space Telescope (HST) imaging of RS Oph 155 days after outburst. Their detection of both [O III] 5007Å and [Ne V] 3426Å in a double-ring structure is consistent with the bi-polar interpretation of the radio emission and they suggest that this is due to interaction with pre-existing circumstellar material. The optical lightcurve is shown in Figure 1.11.

The 2006 outburst of RS Oph was extremely well covered in the X-ray by the Swift, Chandra, and XMM-Newton satellites. The hard X-rays (up to 50 keV) observed are the result of shocks between the ejected material and the wind from the red giant companion (Bode et al. 2006; Hernanz & Tatischeff 2012). The ejecta in this outburst were expelled at a speed of $\sim$6000 kms^{-1} (Vaytet et al. 2011; Luna et al. 2009) and the ejected mass estimates are $10^{-6}\,M_\odot$ (Drake et al. 2009), $10^{-7}\,M_\odot$ (Sokoloski et al. 2006), and $2-5\times10^{-7}\,M_\odot$ (Vaytet et al. 2011). The hard X-ray count rate peaks in the early stages of the outburst and has fallen to $\leq$1 count by day $\sim$20. The Swift-XRT (Gehrels et al. 2004a) X-ray lightcurve (Fig. 1.12) shows three stages in terms of hardness ratio (HR), which is the ratio of flux in the 0.6 - 2 keV band to the flux in the 0.3 - 0.6 keV band. The HR is initially hard, $\sim$10, before declining to $\sim$0.1 by day 30; a super-soft source (SSS, 0.3-0.6 keV) was first observed on day $\sim$30 and turned off on day $\sim$90 as reported by Hachisu et al. (2007) and Osborne et al. (2011). The hardness ratio stays below 1 until day $\sim$100 at which point it begins a steady rise (Osborne et al. 2011). The appearance of the supersoft source coincides with the plateau phase in the optical lightcurve, but no physical link between the two has been established. The hardness ratio is an indication of the source of the emission. Since the hard X-rays come from shocks and the soft X-rays come from the surface of the WD (Osborne et al. 2011), the hardness ratio shows which mechanism is dominant at any given time. The rise of the supersoft source, around day 35, is initially variable as shown in the inset of Figure 1.12,

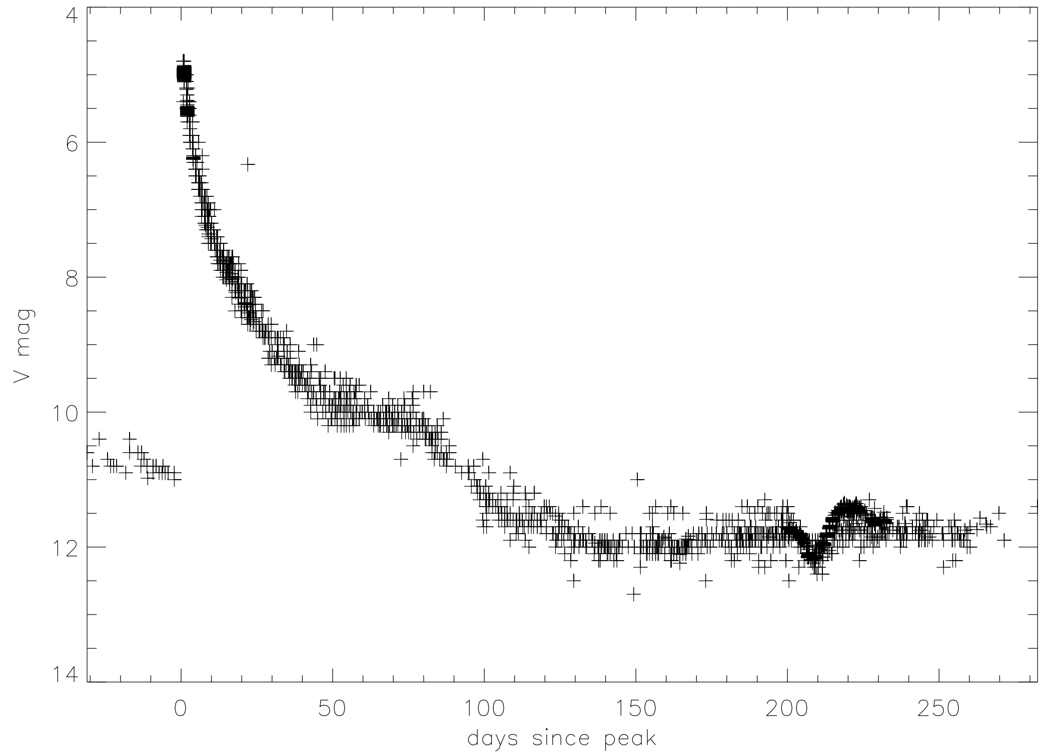

Figure 1.11: V band lightcurve of RS Oph from 12/01/2006 to 12/11/2006. Data from AAVSO. See Adamakis et al. (2011) for a detailed characterisation of the decline. Day zero is taken to be at February 12.83.

and begins to decline on day ∼65. X-ray spectra were also taken during the 2006 outburst of RS Oph, taken at times indicated by marks at the top of Figure 1.12: coloured arrows mark the time of Swift-XRT spectra (see Osborne et al. 2011), X and C mark the times of XMM-Newton and Chandra observations (Ness et al. 2007) respectively.

IR observations of RS Oph show that the companion is a red giant (Pavlenko 2008; Rushton et al. 2010; Rosino et al. 1982) with an effective temperature of 4000 - 4400K (Rushton et al. 2010; Pavlenko 2008). The C^{12}/C^{13} ratio in this system, a diagnostic of evolutionary state, is 16 ± 3 (Pavlenko et al. 2010) which is consistent with the giant having evolved beyond the first dredge-up stage.

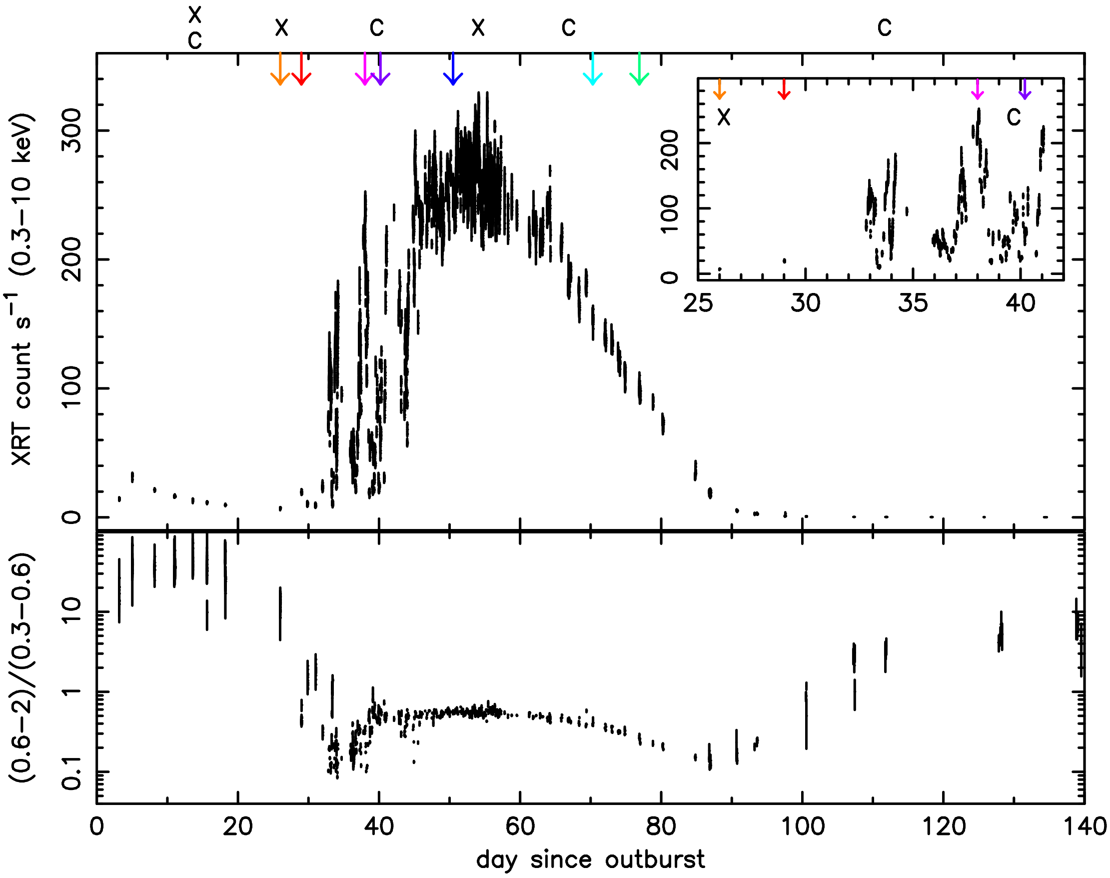

Figure 1.12: X-ray lightcurve of the 2006 outburst of RS Oph from Osborne et al. (2011). Coloured arrows, X, and C mark the times of Swift, XMM-Newton, and Chandra spectra respectively. The initial rise of the super-soft source is inset. Note 1 keV = 1.602 $\times 10^{-16}$ J.

Silicate dust, which forms in the red giant wind, has been observed in quiescence and shortly after the 2006 eruption, indicating that dust survives the outburst (Woodward et al. 2008; Evans et al. 2007b). Dust is not formed in the aftermath of the outburst since the temperature of the ejecta ($\sim 10^4$ K; Evans et al. 2007a) is much higher than the dust condensation temperature ($\sim$600 K; Evans et al. 2007b). IR spectra of RS Oph show an excess due to dust at wavelengths $\geq 5\mu$m; an excess at these wavelengths requires dust at a temperature of $\sim$500 K (Rushton et al. 2010). Banerjee et al. (2009) took near-IR (NIR) spectrophotometry covering the first 94 days of the 2006 outburst and observe emission lines with broad wings and a narrow component consistent with a bi-polar outburst as observed in other wavebands.

Swift/UVOT observations of the 2006 outburst of RS Oph are covered in Chapter 4; although there are significant problems with the calibration of this instrument there is still much that can be learned from these unique observations.

1.11 T Pyxidis

T Pyxidis has undergone six observed outbursts, the most recent of which occurred at 2011 April 14.29 (Waagan et al. 2011). T Pyx has a short orbital period, $\sim$1.83 hours, a main sequence companion of mass $0.14\pm0.03\,M_\odot$, with the primary having a mass of 0.7 ± 0.2 $M_\odot$ (Uthas et al. 2010). From light echoes the distance to T Pyx has been determined to be 4.8 ± 0.5 kpc (Sokoloski et al. 2013).

T Pyx has an unusual outburst history. Since the first observed outburst the recurrence time has been increasing over time. The B band magnitude has also been increasing (becoming fainter) over time as shown in Figure 1.13. It has been suggested that these two factors are not independent, and that the first observed outburst was actually a classical nova outburst which triggered a period of increased mass transfer leading to a series of outbursts (Schaefer 2010).

T Pyx is a slower nova than RS Oph or U Sco as can be seen in Figure 1.14.

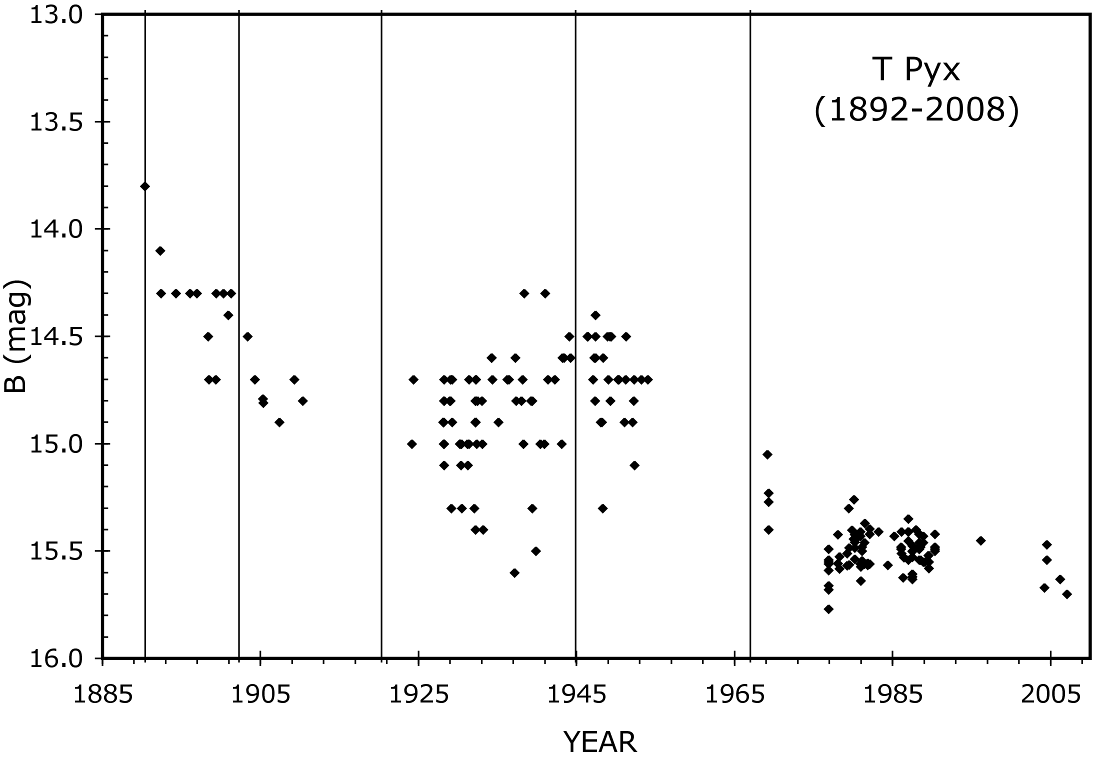

Figure 1.13: Long term B band lightcurve of T Pyx from Schaefer (2010). The times of outbursts are indicated by vertical lines.

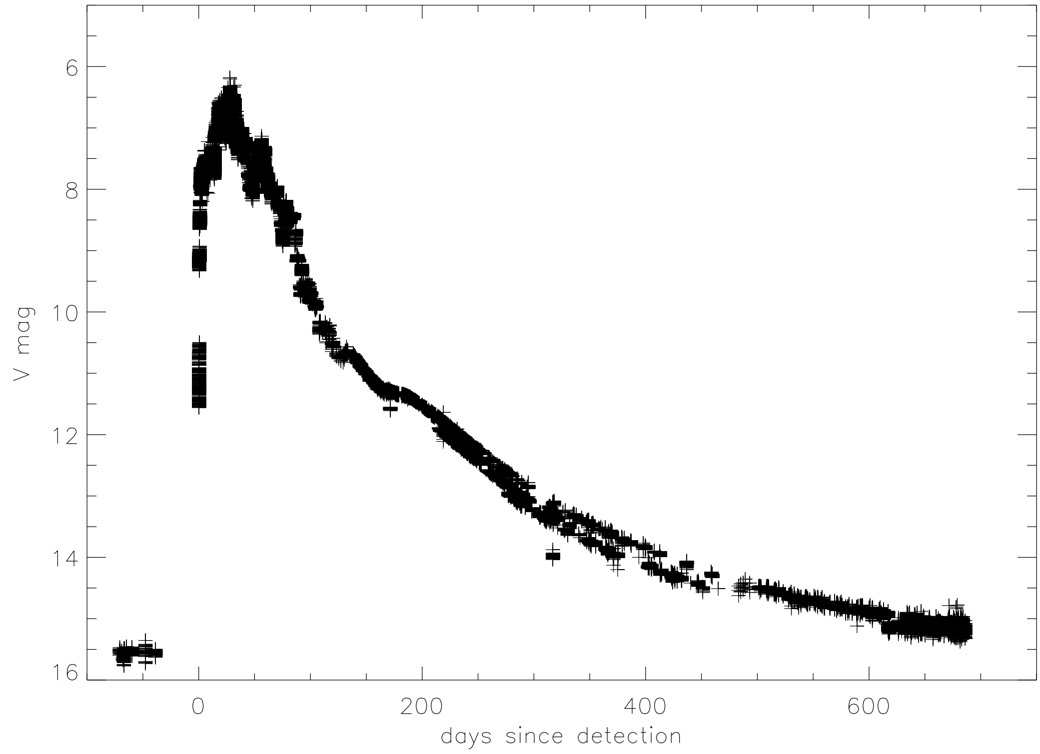

Figure 1.14: V band AAVSO lightcurve of the 2011 eruption of T Pyxidis. Day zero is taken to be at April 14.29.

There is a period of variability following the optical peak followed by a steep initial decline and a long, shallow decline to minimum.

Radio observations of the 2011 outburst have shown that the mass ejection may not be instantaneous, and evidence has been found of a mass ejection ~100 days after the optical peak (Nelson et al. 2012). IR observations of the 2011 outburst showed that pre-existing dust, with a mass of $\sim 10^{-4}\mathrm{M}_{\odot}$ was heated by the ejected material, to a temperature of 45±5 K (Evans et al. 2012). The UV and optical spectroscopic evolution was followed by Shore et al. (2011, 2013b), who derive an ejected mass of $\sim 2 \times 10^{-6}\mathrm{M}_{\odot}$ which was ejected in a bipolar manner, a distance of ≥3.5 kpc, and reddening of $\mathrm{E}_{B-V} = 0.5 \pm 0.1$. SALT RSS spectroscopy of the late decline phase of the 2011 outburst is presented in Chapter 4.

Chapter 2

The 2010 outburst of U Scorpii

2.1 Introduction

As discussed in Chapter 1, previous studies of the helium abundance in the ejecta of U Sco have suggested that the ejecta are He-rich (Iijima 2002; Barlow et al. 1981; Anupama & Dewangan 2000; Evans et al. 2001). Since the ejected material consists primarily of the material accreted from the companion, any enrichment in the ejecta is an indicator of the composition of the companion. Therefore these studies have led to the suggestion that the companion is He-rich (Hachisu et al. 1999). Strong He lines in quiescence (Johnston & Kulkarni 1992) have supported this claim. The composition of the accreted material has major implications for the development of the TNR (Starrfield 2008). Hence determining if the ejecta in the 2010 outburst are enriched or not is an important question. In this Chapter optical and near-infrared spectroscopy of the ejecta of the 2010 outburst are analysed and the helium abundance of the ejecta is determined. The work included in this Chapter, and in Maxwell et al. (2012), is the work of the author of this thesis except where clearly stated otherwise. The contributions of the other authors were primarily data acquisition, as noted in the relevant observing logs, and the discussion of the results and their implications.

2.1.1 Outburst history

The outburst history of U Sco was described in detail by Schaefer (2010). Outbursts were observed in 1863, 1906, 1917, 1936, 1945, 1969, 1979, 1987, 1999, and 2010. It is likely that some outbursts were missed; given the mean recurrence time between the last five outbursts either some outbursts were missed between 1863 and 1906 or nova theory does not properly describe what determines the recurrence interval.

2.1.2 Photometry

The previous four outbursts of U Sco have sufficient photometry for a profile of the outburst lightcurve to be built up. In each case the rise from quiescence to the peak is missed, as is typical for a nova, but following the discovery of each outburst there is good coverage, as can be seen in Figure 1.6 for the 2010 outburst. Following the peak there is an initial decline lasting $\sim$10 days before a plateau phase. Finally, there is a further decline back to the quiescent magnitude for $\sim$20 days. Each outburst follows this pattern closely. The peak of the 2010 outburst of U Sco was at January 28.19 ± 0.17 UT (Schaefer et al. 2010). The outburst was predicted by Schaefer (2005) to occur at 2009.3 ± 1.

2.1.3 Spectroscopy

Optical (Iijima 2002; Anupama & Dewangan 2000; Munari et al. 1999) and IR (Evans et al. 2001) spectra of U Sco were taken in the immediate aftermath of the 1999 outburst. Iijima (2002) took three spectra on days 0.65, 10.64, and 16.61, with the prominent features in the spectrum on day 0.65 being H Balmer lines, He I, and N II lines. By day 10.64 He II 4686Å had become stronger than Hβ. Iijima (2002) notes that the same features were seen in observations of previous outbursts (Barlow et al. 1981; Sekiguchi et al. 1988; Rosino et al. 1982). Munari et al. (1999) took eleven optical spectra covering the first 23 days of the outburst and observed a decrease rate of 270 km s^{-1} day^{-1} of the FWZI of Hα, whilst also noting that their spectra and those from previous outbursts only resemble each other generally. Anupama & Dewangan (2000) took five spectra with good wavelength coverage up to day 43 of the outburst. They also observe strong, broad emission features in the immediate post-outburst spectrum, followed by the rise of He II lines. Triple-peaked line profiles were observed by day 11, in agreement with Munari et al. (1999). By day ∼43 the only lines present in the spectrum were Hα, He II 4686Å, and He II 5411Å. This spectrum is noted to be similar to late-time spectra of the 1979 outburst presented by Barlow et al. (1981). Evans et al. (2001) took five NIR spectra from day 2.34 to day 27.28, observing H Paschen and H Brackett lines as well as He I and He II lines.

2.1.4 Spectral line formation

Emission and absorption lines form via the excitation and de-excitation of electrons in ions or atoms. When an excited electron decays to a lower energy level a photon of specific energy, and therefore wavelength, is emitted. The wavelength at which the photon is emitted will be red or blue shifted from the rest wavelength depending on the velocity of the ion along the line of sight. An emission line will become prominent if many of the same species of ion have electrons excited to the same energy levels, e.g. an emission line will form at 4341Å if hydrogen atoms are present with electrons excited to the n=5 level which then de-excite to the n=2 level, producing the Hγ line. An absorption line will form at the same wavelength if electrons at the n=2 level absorb photons at the energy required to excite them to the n=5 level. There are two methods by which an electron can become excited that are relevant to this thesis: absorption of a photon and collisional excitation. Collisional excitation occurs when free electrons collide with the ion or atom, causing a bound electron to gain energy and become excited. Absorption of a photon will lead to ionisation if the energy gained by the electron is higher than the binding energy; otherwise the electron becomes excited.

Emission line strengths and profiles are a product of the environment in which they are produced. There are two idealised cases when discussing line formation, case A and case B (Baker & Menzel 1938), which describe the optical depth of the line. Case A recombination occurs when lines are produced in high density environments, where they are affected by self-absorption and so measuring the strength of these lines does not give an accurate direct determination of the fluxes, i.e. the lines are optically thick. In the case B scenario the lines are optically thin and so the measured line strengths can give an accurate measure of the flux. The ratios of lines often agree with theoretical values, allowing parameters such as the reddening and elemental abundances to be determined. Throughout this thesis, and in other works on novae, the optical depth of the lines and the consistency of line ratios with the case B ratios are crucial factors. If the line ratios are not in agreement with the case B values then the line is not optically thin, and so if these ratios are used to derive results then those results will have a large error associated with them.

When measuring the abundance of helium relative to hydrogen it is possible to use blended lines via the Pickering series method, which was first implemented by Castor & van Blerkom (1970). The Pickering series of ionised Helium lines is generated by decays to the n=4 energy level. Lines formed by decays from n=6 and n=8 are blended with hydrogen lines, whereas lines formed by decays from n=5, n=7, and n=9 are not. This means that the ratio of the fluxes of blended and non-blended lines gives $(\mathrm{H}^{+} + \mathrm{He}^{++})/\mathrm{He}^{++}$. This method is valid since the product of the transition probability and the statistical weight of the blended H I and He II lines is comparable (Castor & van Blerkom 1970), and the method was employed by Barlow et al. (1981) to determine the helium abundance in the ejecta of the 1979 outburst of U Sco.

Note that throughout this thesis line fluxes are measured in either $\mathrm{W/m^2}/\lambda$ or erg/cm^2/s/λ. A factor of 1000 is required to convert from the former to the latter, i.e. 1 W/m^2/λ = 1000 erg/cm^2/s/λ, assuming the wavelength units are the same.

2.1.5 Helium abundance

Several estimates of the helium abundance in U Sco have previously been made. Barlow et al. (1981) find the helium abundance by number relative to hydrogen to be $\sim$2 following the 1979 outburst using the Pickering series method as discussed above, whereby alternate members of the He II Pickering series are blended with H Balmer lines such that the ratio of the fluxes between blended and non-blended lines gives H^{+}+He^{2+}/He^{2+}. However, this method only applies to narrow component emission and does not account for broad component emission, which in U Sco is significant as material is ejected at speeds $\sim 10^4$ km/s (Banerjee et al. 2010). Evans et al. (2001) find a mean abundance of 4.5 ± 1.7, assuming case B recombination applies. However several of the spectra used in this analysis were taken in the first few days after outburst, at which time the emission lines were optically thick, which prohibits an abundance determination. Evans et al. (2001) also use the Saha equation to determine the distribution of ionisation states. However the Saha equation method is dependent on the electron density and strongly dependent on temperature ($\propto e^{-\epsilon/kT}$), and so these parameters must be extremely well constrained in order to produce an accurate abundance determination. Iijima (2002) reports an abundance of 0.16 ± 0.02, but in this analysis Hα is used, a line which is prone to optical depth effects. Iijima (2002) also assumes that all the helium emission is due to He I and uses a spectrum taken within 24 hours of the outburst. Anupama & Dewangan (2000) find the mean helium abundance to be 0.40 ± 0.06, although individual ratios range from 0.03-1.48 depending on the lines used. Diaz et al. (2012) took a series of spectra in the aftermath of the 2010 outburst and derived a lower limit on the helium abundance of 0.2.

2.1.6 Previous published results on the 2010 outburst

Following the outburst of U Scorpii in 2010 several datasets, covering a variety of wavelength regimes and from the initial hours of the outburst to several weeks after, were obtained and reported by a number of different authors. Here the corresponding reported results are discussed. The initial few days after outburst were observed by Mason et al. (2012), Imamura & Tanabe (2012), Kafka & Williams (2011), Yamanaka et al. (2010), Banerjee et al. (2010), and Diaz et al. (2010), with the evolution over the following days and weeks being observed by Diaz et al. (2010), Banerjee et al. (2010), Mason et al. (2012), and Orio et al. (2012). These observations were largely in the optical, with Banerjee et al. (2010) observing the NIR evolution and Orio et al. (2012) observing the X-ray evolution.

Optical spectra obtained in the first few days after outburst, as can be seen in Figs 2.1-2.2, show strong, broad Balmer line emission, with broad emission lines of N, O and He being prevalent along with some contribution from other elements. P Cygni profiles were observed in the early stages of the outburst. Velocities up to $\sim$6000 $\mathrm{kms^{-1}}$ are derived from the Balmer lines. Flat top line profiles are observed immediately after outburst, as can be seen on day 1.38 in Fig 2.1, which evolve into multi-component Gaussian profiles after a few days. The NIR emission observed by Banerjee et al. (2010) (Fig 2.3) shows strong Paschen line emission, with high velocities up to 10,000 $\mathrm{kms^{-1}}$ being observed. X-ray observations by Orio et al. (2012) (Fig 2.4) from days $\sim$20-40 reveal strong N and O emission, with Ne and C also present, with modelling of the latest observed spectrum suggesting a temperature of $\sim 10^6$ K, consistent with a WD of mass $\geq 1.3\mathrm{M_\odot}$.

As well as spectroscopy, extensive photometry of the outburst and its evolution was obtained by Schaefer et al. (2011). Observations covering the first 67 days after the outburst show that the colour does not change significantly throughout the outburst and that by the end of these observations the magnitude had returned to

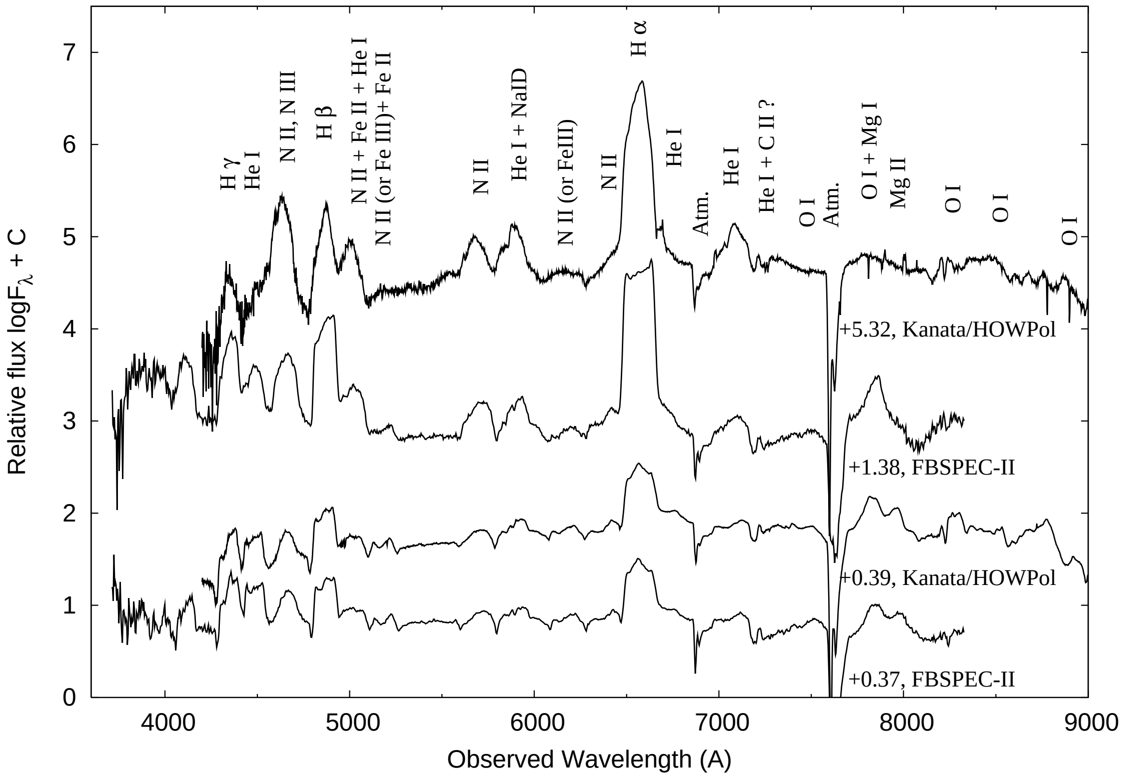

Figure 2.1: Early time spectra of the 2010 outburst of U Sco, from Yamanaka et al. (2010). Labels such as '+1.38' indicate the time in days since outburst.

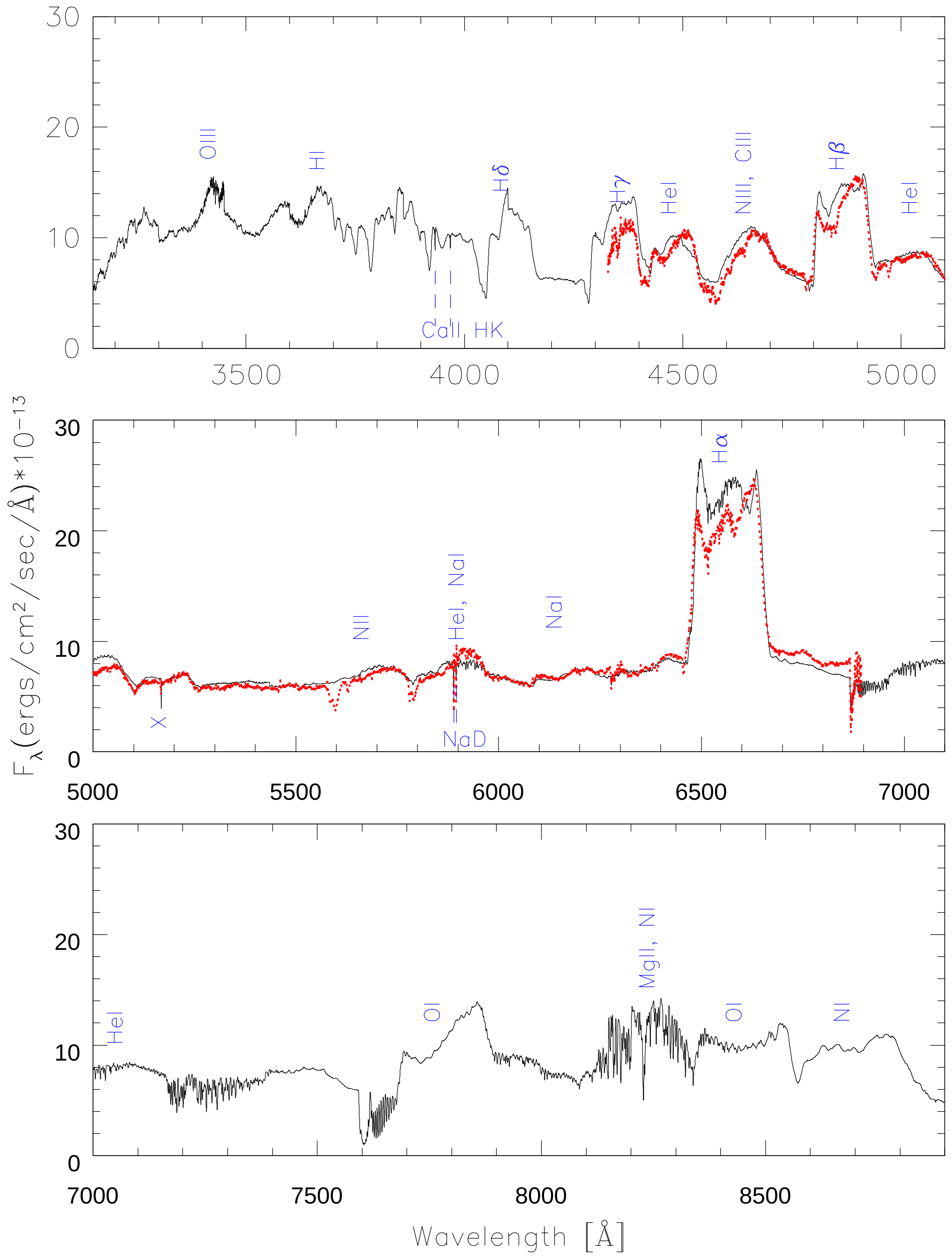

Figure 2.2: Spectrum of U Sco taken one day after the 2010 outburst, from Kafka & Williams (2011). N.B. Throughout this thesis fluxes are measured in either $W/m^2/\lambda$ or $erg/cm^2/s/\lambda$. A factor of 1000 is required to convert from the former to the latter, i.e. $1\ W/m^2/\lambda = 1000\ erg/cm^2/s/\lambda$, assuming the wavelength units are the same.

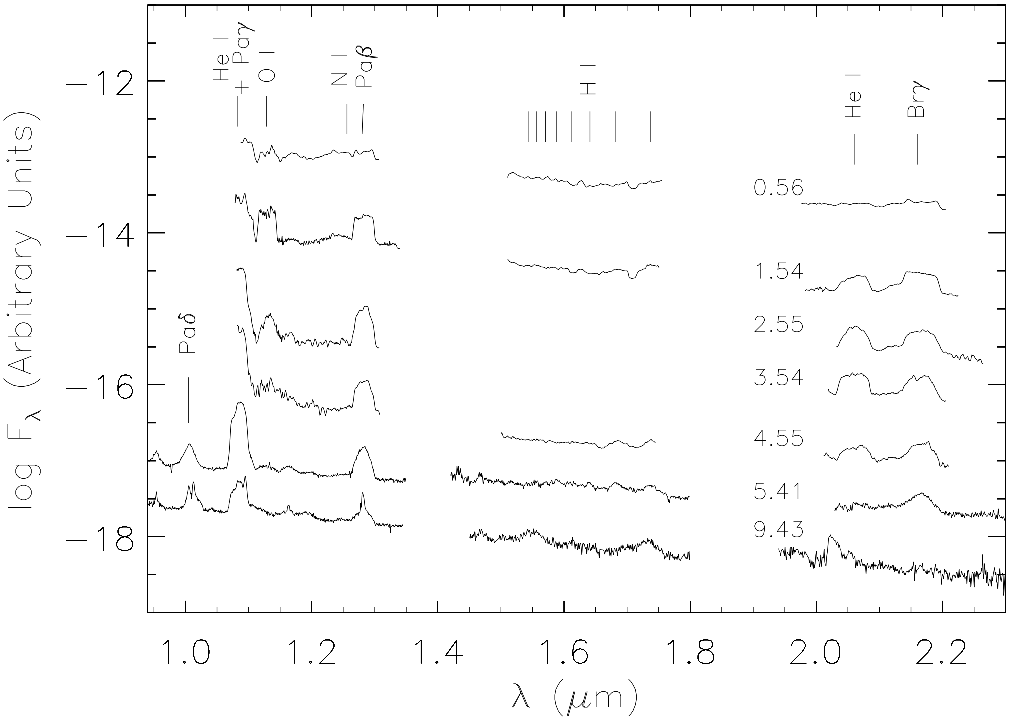

Figure 2.3: Early time NIR spectra of the 2010 outburst of U Sco, from Banerjee et al. (2010).

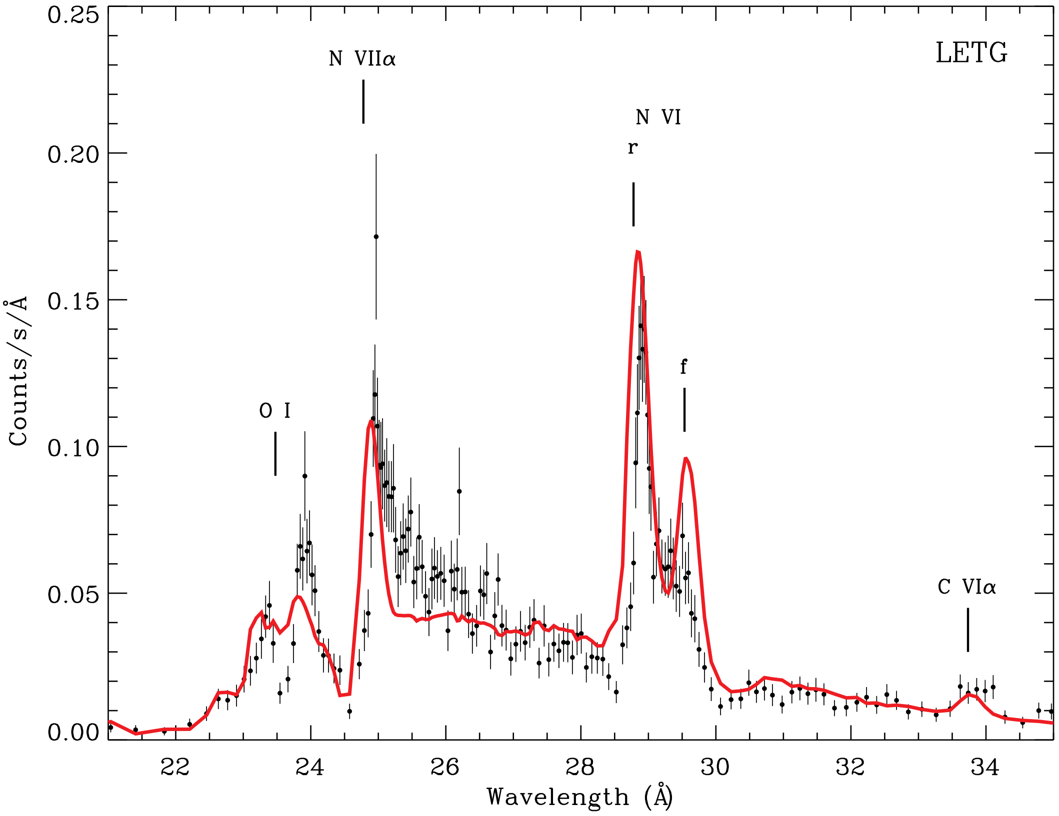

Figure 2.4: X-ray spectrum of the 2010 outburst of U Sco, from Orio et al. (2012). The red line is a two component fit using a WD atmosphere and an optically thin plasma with temperature kT=93 eV.

the pre-outburst level. An X-ray eclipse study by Takei et al. (2013) suggests that the optical and X-ray emitting regions are co-extensive approximately two weeks after the optical peak, and that the ejected mass was of order 10^{-7}-$10^{-6}M_{\odot}$.

2.2 Observations

In addition to the observations of the 2010 outburst reported by other authors and discussed above, following the 2010 outburst optical and near-infrared spectroscopy were obtained by various colleagues and collaborators of the present author, using the FRODOSpec spectrograph (resolving power, $R=\lambda/\Delta\lambda$, $\sim$5000) at the Liverpool Telescope (LT), the grating spectrograph (R$\sim$1000) at the 1.9m telescope at the South African Astronomical Observatory (SAAO), the SOFI spectrograph (R$\sim$1000) at the New Technology Telescope (NTT), and the R-C spectrograph (R$\sim$1500) at the Cerro Tololo Inter-American Observatory (CTIO). The observing log is displayed in Table 2.1. LT data were flux calibrated using an observation of the standard star HD19445 taken on 26/1/2010. Unfortunately standard star observations were not taken simultaneously with the SAAO observations of the outburst of U Sco. The dates and exposure times (start and duration) of the observations are given in Table 2.1. However in the following sections, observations will be referred to by the observation start times, in terms of the number of days since the peak of the outburst at January 28.19 2010 (hereafter 'day' number). All times are in UTC, and in each instance the 'day' is the number of days since the peak of the outburst in UTC to the start of the first exposure for that observation in UTC, such that the first exposure for the observation labelled 'day 1.94' began 1.94 days, in UTC, since the peak of the outburst at 28.19 January 2010.

Table 2.1: Observing Log. The 'day' column indicates the number of days, in UTC, from the peak of the outburst to the start time of the first exposure of that observation.

Date	Start time (UTC)	Day	λ range (Å)	Facility	Instrument	PI	Exposure (s)	Airmass
30/1/10	03:13:16	1.94	3500-7250	SAAO	Grating Spectrograph	T. Kouwenhoven	1180	1.190
2/2/10	03:16:43	4.95	3500-7250	SAAO	Grating Spectrograph	T. Kouwenhoven	715	1.335
3/2/10	02:54:35	5.93	3500-7250	SAAO	Grating Spectrograph	T. Kouwenhoven	1700	1.422
3/2/10	08:30:44	6.16	9950-24000	NTT	SOFI	M. Rushton	1360	1.741
4/2/10	06:12:28	7.07	3900-7900	LT	FRODOSpec	M. Bode	620	1.900
5/2/10	02:25:34	7.91	3500-7250	SAAO	Grating Spectrograph	T. Kouwenhoven	3500	1.548
5/2/10	05:33:20	8.04	3900-7900	LT	FRODOSpec	M. Bode	540	2.257
6/2/10	02:20:12	8.91	3500-7250	SAAO	Grating Spectrograph	T. Kouwenhoven	2600	1.558
6/2/10	05:25:39	9.04	3900-7900	LT	FRODOSpec	M. Bode	6480	2.307
6/2/10	09:11:13	9.19	4000-4800	CTIO	SMARTS	F. Walter	900	1.317
6/2/10	09:10:25	9.19	9950-24000	NTT	SOFI	M. Rushton	3000	1.517
7/2/10	02:14:20	9.90	3500-7250	SAAO	Grating Spectrograph	T. Kouwenhoven	5330	1.571
8/2/10	02:35:52	10.92	3500-7250	SAAO	Grating Spectrograph	T. Kouwenhoven	2900	1.417
9/2/10	02:04:46	11.90	3500-7250	SAAO	Grating Spectrograph	T. Kouwenhoven	3500	1.583
9/2/10	05:24:34	12.04	3900-7900	LT	FRODOSpec	M. Bode	2700	2.170
10/2/10	06:23:53	13.08	3900-7900	LT	FRODOSpec	M. Bode	5400	1.684

Table 2.2: IRAF tasks and their usage

FLATCOMBINE	combines multiple flatfield images to produce a master flat
IMCOMBINE	combines multiple science images to produce a master science frame
IMARITH	performs arithmetic operations on images
APALL	extracts a 1D spectrum from an image
IDENTIFY	mark arc lamp lines to produce a wavelength solution
DISPCOR	applies the wavelength solution to the science spectrum
STANDARD	adds a standard star to the input file for sensfunc
SENSFUNC	generates a sensitivity function for the standard star
CALIBRATE	flux calibrates the science frame using the sensitivity function generated by sensfunc

2.2.1 Data reduction

The data from both LT and SAAO were reduced by the present author, using standard routines in IRAF[1] (Image Reduction and Analysis Facility). In each case the data had been partially reduced by the author's collaborators using the reduction pipeline of that facility (see Barnsley et al. (2012) for LT. SAAO manuals can be found at the SAAO website[2]), but several steps were still needed to be completed before the data could be used. These steps include: combining flat-field CCD images to make a master flat; combining the science CCD frames; dividing the science frames by the master flat; extracting the 1-D spectrum; generating a wavelength scale using an arc lamp; and applying this solution to the spectrum. These steps are repeated for a spectrophotometric standard star which can then be used to flux calibrate the science spectrum. The tasks used to perform these steps and their usage are listed in Table 2.2.

The NTT and CTIO data were obtained and reduced by Dr Mark Rushton

---

[1] http://iraf.noao.edu/

[2] http://www.saao.ac.za/observing/operating-manuals/19-m-telescope-instruments/

(UCLan) and Dr Fred Walter (Stony Brook University) respectively. LT and SAAO data were obtained by a resident astronomer, who in each case performed the initial reductions using the appropriate reduction pipeline. The extraction and wavelength calibration for the LT and SAAO data were successfully completed by the author. Flux standards were not observed for SAAO data. SAAO data were wavelength calibrated using a CuAr lamp, LT data with a Ne lamp. An observation of an arc lamp was taken after each LT and SAAO observation. Although an absolute flux calibration was not determined for the LT data, a pixel-to-pixel (relative sensitivity) calibration was possible using an observation of the standard star HD19445, utilising the IRAF tasks STANDARD, SENSFUNC, and CALIBRATE as outlined in Table 2.2. Since determining parameters such as the reddening and elemental abundances relies only on ratios of relative line fluxes rather than absolute line fluxes, a pixel-to-pixel calibration is considered to be sufficient for this work. The fact that no flux calibration was possible for the SAAO data is more of an issue; since the sensitivity across the detector cannot be determined this will add a significant source of error to the results. Fortunately all the lines present in the SAAO data which will be used in this analysis are observed by the same grating and detector, so the relative sensitivity of different detectors is not an issue, and none of the lines are within ∼100Å of the detector edge, where the sensitivity tends to drop off. Figure 9.15 of the SAAO observing manual[3] also indicates that the sensitivity of the detector does not vary by a substantial amount in the range 4000-5500Å. A conservative estimate of the accuracy of a flux calibration is 20%. Here, therefore, the error on measurements of SAAO line strengths shall be assumed to be 20% since the other sources of uncertainty on line strengths are small compared with the flux calibration uncertainty. Errors on measured line fluxes in LT data, and in datasets in later Chapters, are standard 1σ (internal) errors for a Gaussian profile.

---

[3] http://www.saao.ac.za/wp-content/uploads/sites/5/spmanv6.4.1.pdf

2.2.2 Spectroscopy

Figures 2.5 and 2.6 show the dereddened (E_{B-V}=0.2, see section 2.3) optical spectra of U Sco covering most of the first 13 days of the outburst. The strong emission lines are due to H I, He I, N III, and, at later times, He II. The He I lines fade as the He II lines develop and are no longer detectable by day 12.04. N III and Hγ also fade and are very weak or undetectable by this time. Hδ and He II 4686Å are both blended with N III. Figures 2.7 and 2.8 show near-IR spectra of U Sco; they show the Paschen series of hydrogen in emission along with O I, He I, and He II emission lines. Paschen γ and Paschen δ are blended with He I and He II respectively. Figure 2.7 also shows a spectrum from the outburst in 1999 taken at a similar time after maximum to the first NTT spectrum; the spectra are very similar with the same emission features present and similar relative line strengths.

The FWZI of each line present in the spectra is measured, with some lines also showing narrow components; in these cases the FWHM of that component is also measured. The contribution of instrumental resolution was not found to be very significant, accounting for only ~6% of the spectral resolution $\Delta\lambda$. Velocities and the associated errors were measured by fitting Gaussian profiles and a first order polynomial using the ELFINP procedure in DIPSO (Howarth et al. 2004). When determining the FWZI of a line the zero-point is considered to be at the point that the value of the Gaussian profile drops below the value of the first order polynomial. Gaussian profiles are used for convenience, as they can be easily combined to fit a blend of lines, give appropriate errors at the 68% confidence interval, and Doppler broadening of an emission line is modelled well by a Gaussian profile. The Hα velocity is consistent with previous outbursts at similar times (Iijima 2002) at 8000$-$9000 km s^{-1}. The width of each line can be seen in Tables 2.3-2.5, and can be seen to be changing with time. Also, the profile of each line is changing rapidly as can be seen in Figures 2.5 and 2.6. Tables 2.4 and 2.5 show the evolution of the narrow

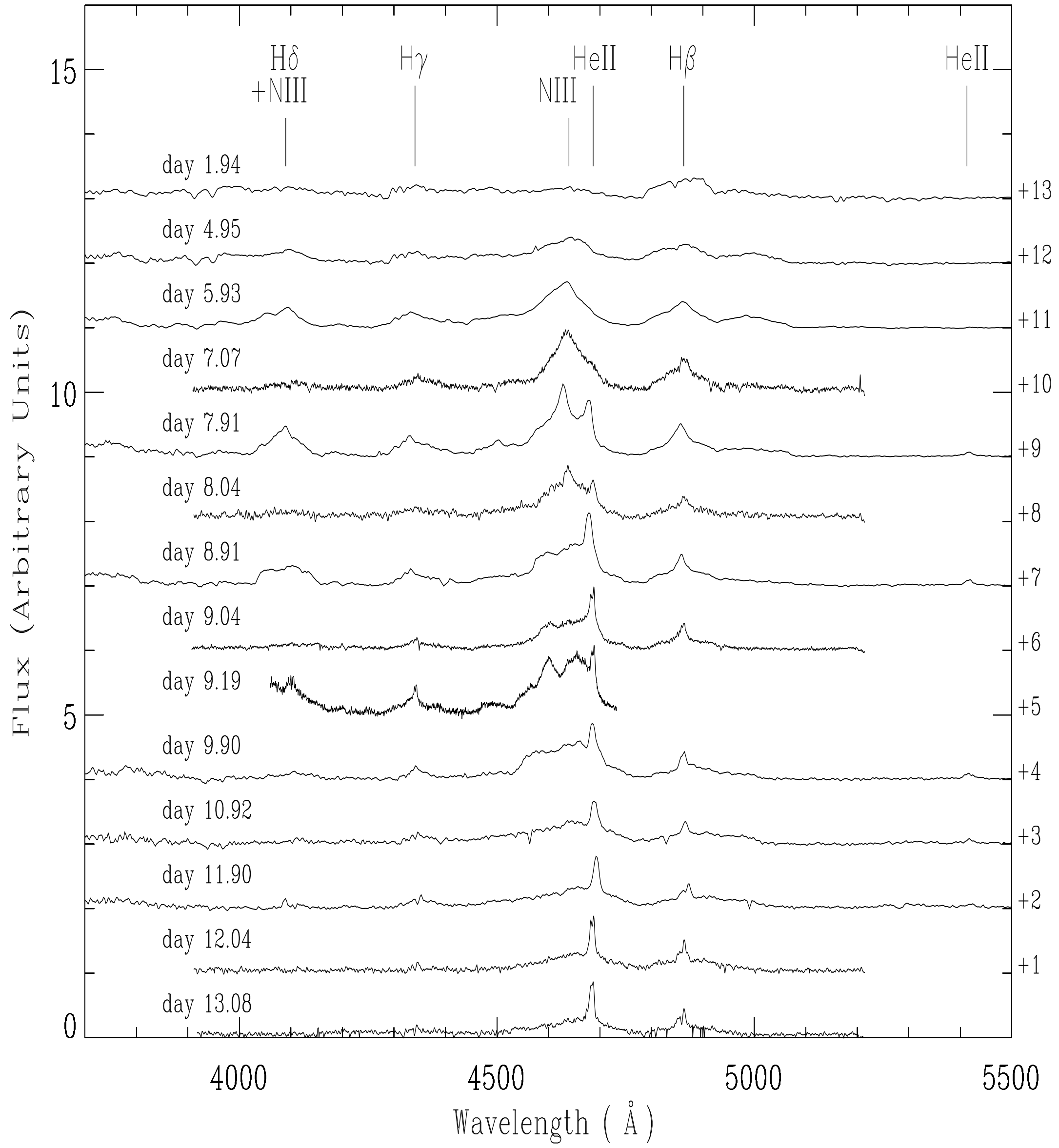

Figure 2.5: Spectra of U Sco taken from day 1.94 to 13.08 at LT, CTIO, and SAAO. The spectra are offset as indicated and the continuum has been removed. LT spectra are smoothed with a Gaussian profile to match the SAAO resolution.

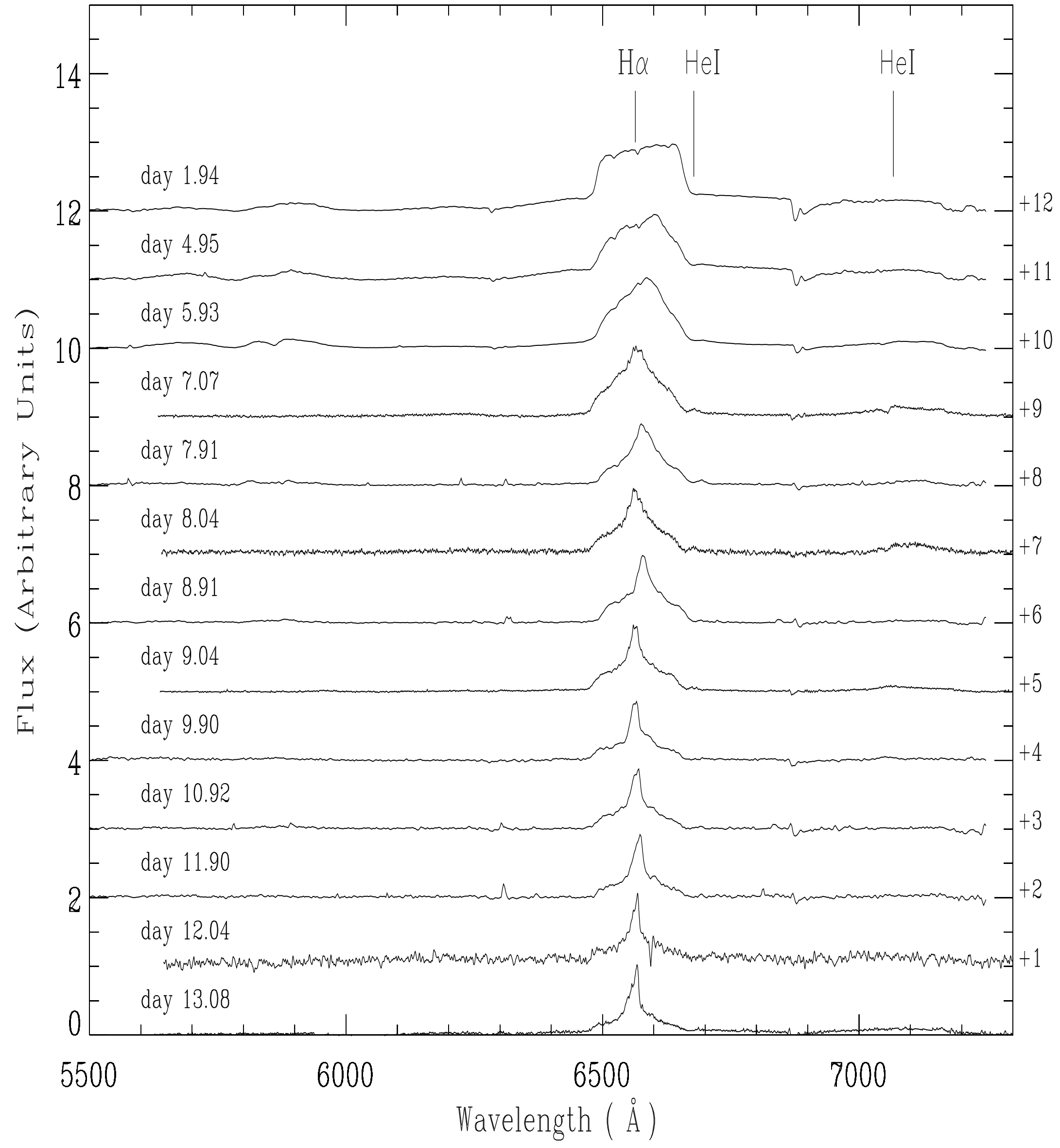

Figure 2.6: Spectra of U Sco taken from day 1.94 to 13.08 at LT and SAAO. The spectra are offset as indicated and the continuum has been removed. LT spectra are smoothed with a Gaussian profile to match the SAAO resolution.

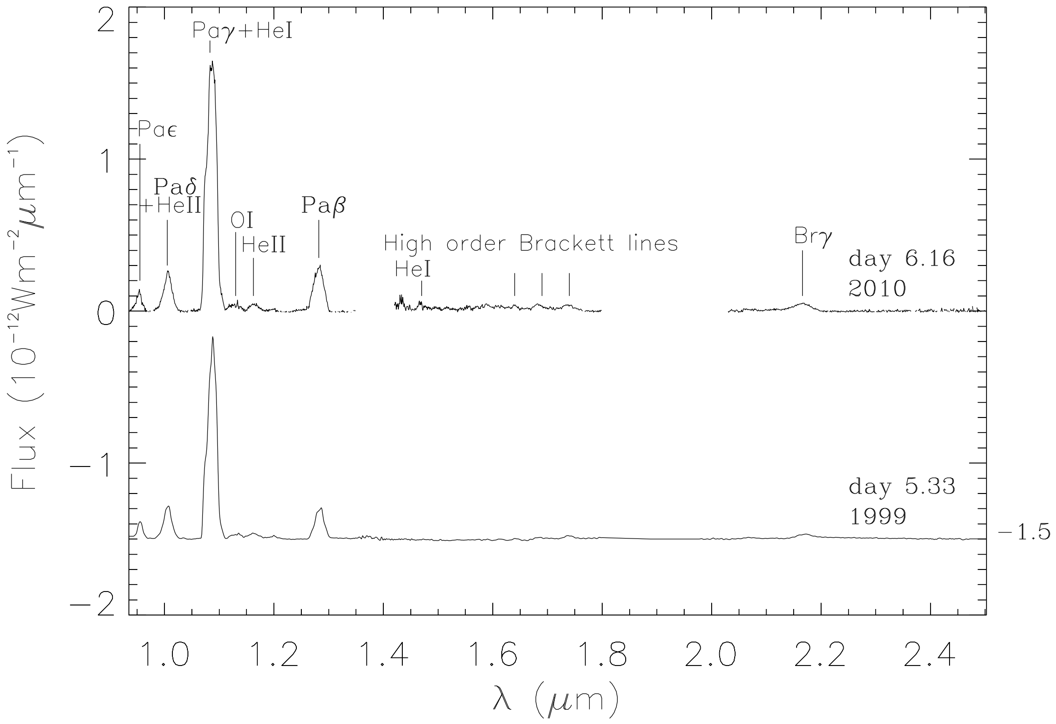

Figure 2.7: Top: IR spectrum of U Sco taken at the NTT on day 6.16 of 2010 outburst. Bottom: IR spectrum of U Sco taken at the NTT 5.33 days after the maximum of the 1999 outburst from Evans et al. (2001), offset as indicated on right hand side.

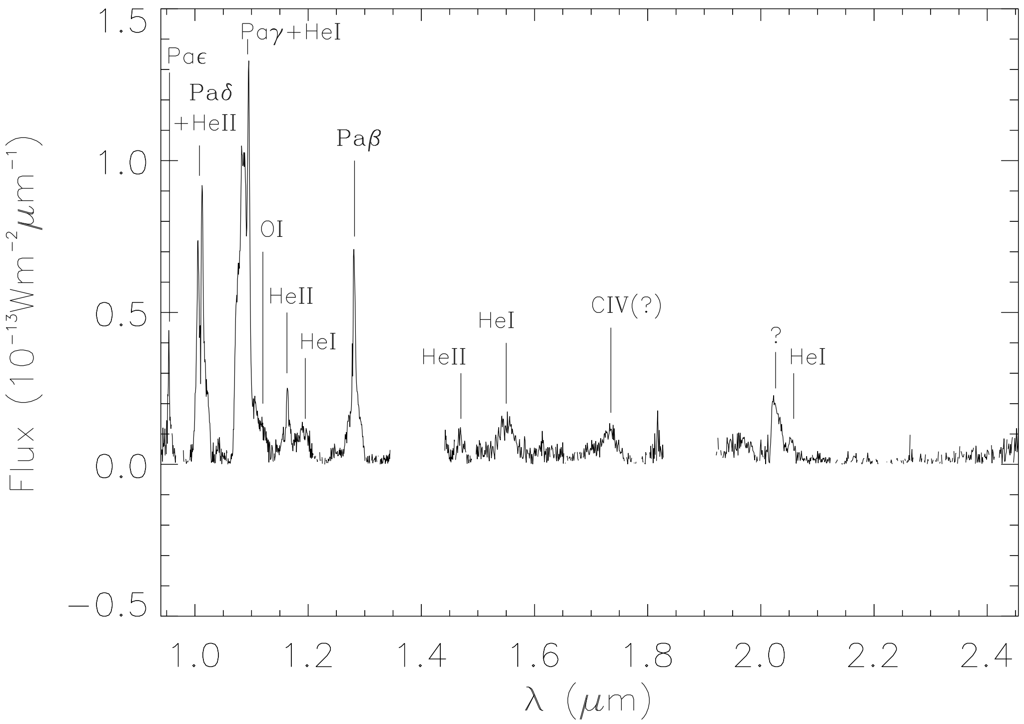

Figure 2.8: IR spectrum of U Sco taken at the NTT on day 9.19 of 2010 outburst.

components of Hα and Hβ. Such high velocity outflows ($\simeq 10,000\,\mathrm{km\,s^{-1}}$) were also seen in early (≤ 5 days) IR spectra of this outburst of U Sco (Banerjee et al. 2010).

Integrated line fluxes, in arbitrary units, were measured by fitting Gaussian profiles to the lines with a least squares fit and can be seen in Table 2.6. Multiple profiles were used in some cases; an example of this is shown in Figure 2.9. These fluxes were then ratioed and compared to theoretical values from Hummer & Storey (1987). From these ratios the abundance of species A to species B can be found using

$$\frac{F_A}{F_B} = \frac{\lambda_B}{\lambda_A} \times \frac{N_A}{N_B} \times \frac{\alpha_A}{\alpha_B}, \tag{2.1}$$

(Osterbrock & Ferland 2006), where F is the measured dereddened flux, N is the abundance by number, and α is the recombination coefficient from Hummer & Storey (1987) for species A and B respectively. The sources of H I, He I, and He II emission are assumed to be co-extensive.

This process was repeated for each available He I (for He^{+}) and He II (for He^{++}) to hydrogen line ratio. Since the spectra show both neutral and once-ionised states of helium in emission the total abundance can be directly measured instead of needing to use the Saha equation (Saha 1921), which determines the abundance of one species of an element relative to another depending on the temperature and density, via

$$\frac{n_{i+1} \times n_e}{n_i} = \frac{2}{\wedge^3}\frac{g_{i+1}}{g_i} \exp\left[\frac{-\epsilon_{i+1} - \epsilon_i}{kT}\right], \tag{2.2}$$

$$\wedge = \sqrt{\frac{h^2}{2\pi m_e kT}}, \tag{2.3}$$

(where n$_e$ is the electron density, g is the degeneracy, ϵ is the ionisation energy, k is the Boltzmann constant, T is the temperature, h is Planck's constant, and m$_e$ is the mass of an electron), to predict the abundance of one species (n+1) from the other (n).

Table 2.3: Broad Component Line Widths (FWZI, kms^{-1}) from LT and SAAO.

	Hγ	N III 4616Å	He II 4686Å	Hβ	Hα	He I 6678Å	He I 7065Å
1.93	-	-	-	8000±2000	10000±1000	-	-
4.93	-	-	-	9000±2000	9000±1000	-	-
5.93	12000±2000	-	-	12000±2000	9000±1000	-	-
7.07	9000±3000	8000±2000	6000±2000	9000±2000	8000±1000	2000±500	13000±3000
7.91	10000±2000	-	6000±3000	9000±2000	9000±1000	-	-
8.04	-	8000±1000	6000±2000	9000±2000	8000±1000	1000±500	10000±2000
8.91	9000±2000	-	6000±2000	9000±1000	9000±1000	-	-
9.04	8000±2000	12000±2000	4000±2000	8000±2000	8000±500	1500±250	12000±2000
9.90	4000±1000	-	4000±1000	3000±1000	9000±2000	-	-
10.92	4000±1000	-	2000±500	3000±1000	9000±1000	-	-
11.90	4000±1000	-	2000±500	2000±500	9000±1000	-	-
12.04	-	-	1500±500	2000±1000	8000±2000	-	-
13.08	-	-	1200±250	1500±500	8000±1000	-	-

Table 2.4: Narrow Component Line Widths (FWHM, kms^{-1}) from LT data.

Day	7.07	8.04	9.04	12.04	13.08
Hβ	1001.95 ± 72.36	836.21 ± 131.3	953.53 ± 41.62	882.85 ± 61.97	1234.63 ± 85.49
Hα	1071.35 ± 50.0	1146.4 ± 46.77	849.94 ± 23.94	753.96 ± 57.1	1380.0 ± 41.95

Table 2.5: Narrow Component Line Widths (FWHM, kms^{-1}) from SAAO data.

Day	1.94	4.95	5.93	7.91	8.91	9.90	10.92	11.90
Hβ	-	-	-	1782.15±106.9	1318.17±108.8	975.48±71.76	764.72±53.5	1192.30±80.41
Hα	-	-	-	1413.54±68.99	876.78±40.20	778.07±32.47	841.79±30.53	882.26±36.28

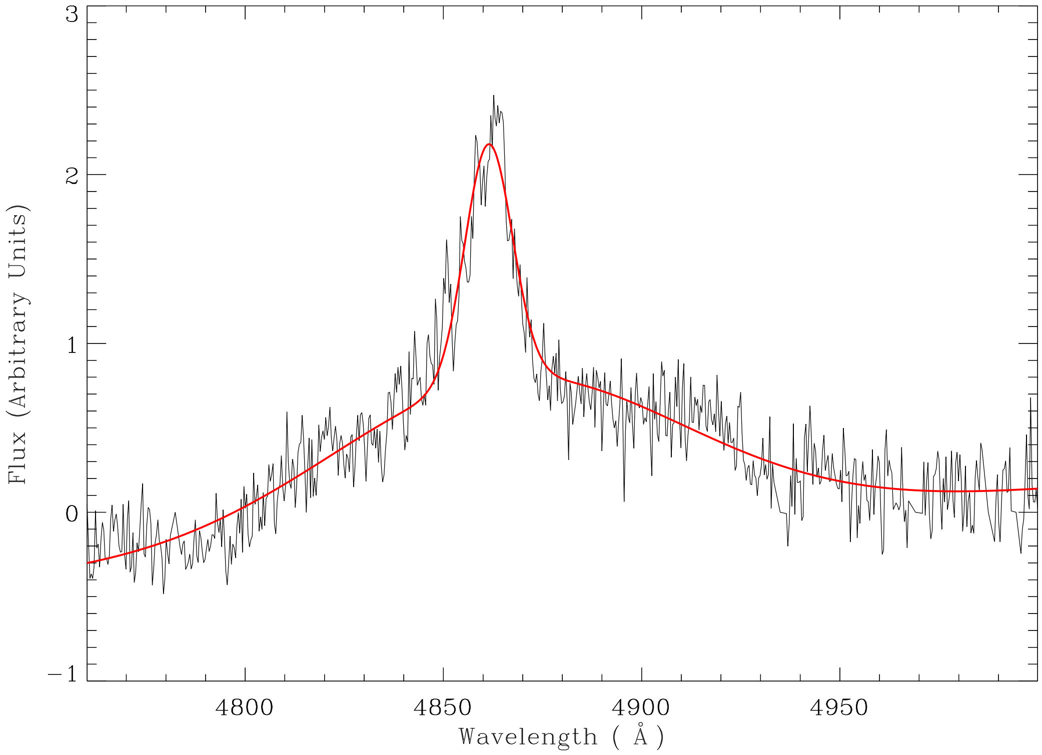

Figure 2.9: Example of a double Gaussian fit to an emission line.

Table 2.6: Dereddened line fluxes. Fluxes and errors are relative to Hβ on that date for optical data and Paβ for near-IR data.

	Hβ	Hγ	Paβ	Paϵ	He I 6678Å	He II 4686Å	He II 5411Å	He II 1.163μm
9.04	1±0.01	0.46±0.07	-	-	0.018±0.003	-	-	-
9.19	-	-	1±0.04	0.45±0.02	-	-	-	0.18±0.01
9.90	1±0.2	0.29±0.08	-	-	-	0.34±0.10	0.074±0.021	-
10.92	1±0.2	0.12±0.03	-	-	-	0.19±0.05	0.022±0.006	-
11.90	1±0.2	0.25±0.07	-	-	-	0.28±0.08	0.036±0.010	-

2.3 Reddening

Several studies (Barlow et al. 1981; Amôres & Lépine 2005; Burstein & Heiles 1982) as well as the dust maps of Schlegel et al. (1998) have shown the reddening of U Sco to be in the range $\mathrm{E}_{B-V} = 0.09 - 0.36$. The ratios of line fluxes were estimated and compared to the theoretical values derived from Hummer & Storey (1987). The optical spectra taken on day 9.04 at LT and day 9.19 at CTIO (Figs 2.1 and 2.2), and the IR spectrum taken on day 9.19 at NTT (Fig 2.4) are used to estimate the reddening, as by this time the flux ratios are converging on case B values. The extinction law and assumption of R=3.1 of Howarth (1983) are used. Using the ratios Hβ/Paϵ, Hβ/Paβ, Hγ/Paϵ, and Hγ/Paβ the reddening was found to be in the range $\mathrm{E}_{B-V} = 0.02 - 0.34$ with a mean of $\mathrm{E}_{B-V} = 0.17 \pm 0.14$, consistent with the previous studies. Although U Sco is at a distance of 12 kpc, low reddening is consistent with the line of sight leaving the plane of the Galaxy: the system is at a height of $z = 4.5$ kpc above the galactic plane (Schaefer 2010). For the spectra used in this thesis $\mathrm{E}_{B-V} = 0.2$ is adopted as a good compromise between this value and previous estimates; the value chosen within the range determined changes the measured fluxes by only ~1%, considerably less than the error on the measured flux. The equations used to calculate the reddening, reproduced below, are described in Howarth (1983). Equations 2.4 and 2.5 describe the extinction law in the optical and IR respectively,

$$X(x) = R + 2.56(x - 1.83) - 0.993(x - 1.83)^2 \tag{2.4}$$

$$X(x) = ((1.86 - 0.48x)x - 0.1)x \tag{2.5}$$

where $x = 1/\lambda$, then

$$E(B-V) = \frac{-2.5}{x_1 - x_2} \log(\frac{F_1}{F_2}\frac{F_2^i}{F_1^i}) \tag{2.6}$$

where F_1 and F_2 are the fluxes of the two lines being used to determine the extinction and F_1^i and F_2^i are the recombination coefficients of those lines from Hummer & Storey (1987).

2.4 Helium Abundance

The helium abundance in the ejecta of U Sco was calculated using H I, He I, and He II recombination lines. The line fluxes on days 9.04 (LT), 9.90-11.90 (SAAO), and 9.19 (NTT) are used to estimate the helium abundance, as by this time the line ratios are converging on case B values. The large Hα/Hβ ratio throughout the available time coverage shows that Hα should not be used in the abundance analysis due to optical depth effects.

Abundance analyses of helium are complicated by the metastability of the lowest triplet level of He I, 2^3S, which can cause some lines to become optically thick. Furthermore, collisional excitations from this level enhance triplet lines. The collisional contributions are 56% for 5876Å, 78% for 7065Å, and 72% for 1.083μm using relations from Kingdon & Ferland (1995) and Peimbert & Torres-Peimbert (1987) at a temperature of 2×10^4 K at the high density limit. The contribution is lower in the singlet lines, although collisions from the 2^1S level must be taken into account. The ratio of 7065Å/4471Å is an optical depth indicator (Osterbrock & Ferland 2006) and this ratio (1.31) is inconsistent with the case B value (~ 0.5), further evidence that the 7065Å line is unsuitable for this analysis. In this abundance analysis the He I line at 6678Å is used; for this line the collisional contribution is 27% using equation 12 of Kingdon & Ferland (1995) at a temperature of 2×10^4 K. At temperatures of 10^4 K and 3×10^4 K the collisional contributions for this line are 7% and 36% respectively. He II lines at 4686Å (LT and SAAO), 5411Å (SAAO), and 1.163μm

Table 2.7: Helium ion abundances

Helium Line	Derived Ion Abundance
He I 6678Å	0.061 ± 0.016
He II 4686Å	0.047 ± 0.035
He II 5411Å	0.076 ± 0.057
He II 1.163μm	0.061 ± 0.010

(NTT) are also used; the line strength ratios can be seen in Table 2.6.

Following Evans et al. (2001) the electron density is estimated using Paschen and Brackett series H I lines from near-IR spectra (Figs 2.7 and 2.8) using the equation

$$F(H) = \frac{\epsilon \phi N_e^2}{\alpha} \times \frac{V^3 t^3}{3D^2}, \tag{2.7}$$

where $F(H)$ is the measured flux of a hydrogen line in the spectrum, ϵ is the case B emissivity from Hummer & Storey (1987), α is the number of electrons per hydrogen atom, ϕ is the volume filling factor, N_e is the electron density in units of m^{-3}, V is the velocity in kms^{-1}, D is the distance in metres, and t is the time since maximum in days; $\alpha = 1$, $\phi = 0.01$, and $D = 12\,\mathrm{kpc}$ are assumed (Evans et al. 2001). The results are consistent with those of Evans et al. (2001) at similar times, and so their values of electron density of $10^{10}\,\mathrm{cm}^{-3}$ for data taken before day 9.19 and $10^{9}\,\mathrm{cm}^{-3}$ for data taken at later times are adopted. The recombination coefficients are relatively insensitive to temperature; $T_e = 20,000\,\mathrm{K}$ is assumed. Using the line fluxes in Table 2.6 $N(\mathrm{He}^+)/N(\mathrm{H}^+) = 0.061{\pm}0.016$ and $N(\mathrm{He}^{++})/N(\mathrm{H}^+) = 0.061{\pm}0.010$ are derived from the data obtained at LT, NTT, and CTIO using the He I line at 6678Å and the He II line at 1.163μm. From the SAAO data $N(\mathrm{He}^{++})/N(\mathrm{H}^+) = 0.047 \pm 0.035$ is derived using the He II line at 4686Å and $N(\mathrm{He}^{++})/N(\mathrm{H}^+) = 0.076 \pm 0.057$ using the line at 5411Å. These results are summarised in Table 2.7.

2.5 Conclusion

The helium abundance in U Sco has been the subject of many studies which have resulted in a wide range of values from 0.16 to 4.5 (Iijima 2002; Barlow et al. 1981; Anupama & Dewangan 2000; Evans et al. 2001). Here the abundance is found to be $N(\mathrm{He})/N(\mathrm{H}) = 0.122 \pm 0.157$. Using just the data for which there is a reliable flux calibration, since the assumed 20% error on line flux measurements for the SAAO data is the major factor contributing to the large uncertainties on the result, the derived abundance is 0.122 ± 0.018, lower than that found by Iijima (2002), Barlow et al. (1981), Anupama & Dewangan (2000), and Evans et al. (2001). Iijima (2002) derived a value of 0.16 using spectra obtained in the immediate aftermath of the 1999 outburst, at which time the ejecta was optically thick, meaning abundances cannot be accurately determined. Additionally, only He I lines were used, further invalidating this result. The result of Barlow et al. (1981) was determined using just He II lines using the Pickering method, which only accounts for narrow component emission, therefore this result is not reliable. Evans et al. (2001) determine the highest abundance, He/H = 4.5, however in this case the Saha equation was used to estimate the abundance, which as previously mentioned is extremely sensitive to the assumed temperature and density making it difficult to produce a reliable estimate in this way. The abundance of He/H = 0.4 derived by Anupama & Dewangan (2000) is the most robust of these estimates, as both He I and He II lines were used from spectra obtained after the ejecta had become optically thin, although Hα, which remains subject to optical depth effects for longer than other lines, was used to determine the He/H ratio in some cases. In this work, the He/H abundance was determined using spectra taken after the ejecta had become optically thin, which contain recombination lines from both He^{++} to He^{+} and He^{+} to He, and enough Balmer lines that the use of Hα is not necessary. A high helium abundance would suggest that the companion in U Sco is a highly evolved star, but the value derived here is close to the solar value N(He)/N(H) = 0.085 (Asplund et al. 2009). This estimate suggests that assumptions about the helium-rich nature of the companion are unfounded and that the companion did not accrete helium-rich material significantly in the post common envelope phase (Hachisu et al. 1999). In the evolutionary calculations of Sarna et al. (2006), U Sco is best represented by their sequence B, with a hydrogen-rich companion. For this helium abundance analysis only data obtained $\geq$8 days after outburst and lines for which case B recombination is valid have been used. Other estimates have been larger than this value, especially those based only on the He II lines. These large abundances result from the use of the Saha equation, which is highly sensitive to the assumed electron temperature. However, here both He I and He II lines are used in the analysis, avoiding the use of the equation to derive the total helium abundance. The temperature dependencies in this analysis are in the recombination coefficients, which are relatively insensitive to the value chosen, and in the collisional correction for He I lines. Using a range of lines from days 9.04 and 9.19 and a range of recombination coefficients several $\mathrm{He}^{++}/\mathrm{He}^{+}$ ratios are determined, each of which suggest electron temperatures of $2.3 - 2.4 \times 10^4\,\mathrm{K}$, therefore recombination coefficients for the closest temperature from Hummer & Storey (1987) of $T_e = 2 \times 10^4\,\mathrm{K}$ are used.

The hydrogen line profiles have broad and narrow components. The narrow components become prominent around day 8 and arise from slow moving material at speeds of $\sim 1000\,\mathrm{kms}^{-1}$. The broad components are composed of material travelling at velocities of up to $\sim 10,000\,\mathrm{kms}^{-1}$. The rise in the strength of the narrow components could be explained by optical depth effects. The ejecta begins to become optically thin around day 8; before this time slower moving material would be concealed by the shell of optically thick fast moving material. As the faster moving material expands and becomes optically thin the flux from the slow moving material becomes visible. He II lines also begin to dominate the helium emission around day 8, however this is most likely due to photo-ionisation of helium rather than an optical depth effect.

The measured line widths are generally consistent for the broad emission, however for the narrow component emission the measured velocities are generally higher for the SAAO data than for near-simultaneous LT data; one explanation for this is differences in the signal-to-noise since a lower signal to noise makes it difficult to determine where the broad emission becomes dominant over the narrow emission. The SAAO observations were also taken a few hours earlier than the LT observations on each night, therefore the orbital phase is different, which could result in different parts of the emission being obscured by the companion star, leading to different observed velocities. Although the narrow component emission appears to increase on the last day of LT and SAAO observations, this may not be what is actually happening, rather the broad emission has receded allowing the wings of the narrow component to become visible. There also appears to be clear structure to the Hβ line in the LT spectra which is not present in the SAAO spectra. In order to better determine the structure of the emission lines, the different components, and the width of the narrow component high resolution, high signal-to-noise spectra are required covering the first $\sim$2 weeks following an outburst. A possible source of the narrow components is an inclination effect; since U Sco is a high inclination system most of the velocity is in the plane of the sky, therefore a small radial component may be present. This is consistent with the asymmetric ejecta models of Drake & Orlando (2010). Data over a longer time range and with better orbital phase coverage are required to explore this further.

Chapter 3

U Scorpii in quiescence

3.1 Introduction

U Sco, like all recurrent novae, is poorly observed in quiescence. In order to properly understand the characteristics of an outburst and the phenomena observed it is essential that the nature of the system in quiescence is well understood. There is still extreme uncertainty regarding the mass accretion rate and the nature of the companion, both of which need to be properly determined in order to interpret the outbursts. Thoroughgood et al. (2001) observed U Sco ∼2 months after the 1999 outburst; the V-band magnitude is in the final decline stage at this time and is just returning to the pre-eruption level. Using the radial velocity of the white dwarf they find the mass of the primary to be $1.55 \pm 0.24\,\mathrm{M}_{\odot}$, near to the Chandrasekhar limit. They attempt to determine the spectral type of the companion by comparing the Mg I b absorption feature in their spectra to a catalogue of template stars. However they are unable to constrain the spectral type due to the quality of the data. They do however determine a radius for the companion of $2.1 \pm 0.2\,\mathrm{R}_{\odot}$ using the radial velocities of the primary and companion, suggesting that it is evolved. Johnston & Kulkarni (1992) observed U Sco in 1990 and 1991, 3 and 4 years after the 1987 outburst respectively. They detect Ca II, H Balmer, and He I lines in absorption and He II in emission. Due to the ratio of calcium H and K lines to Hδ, and the non-detection of the G-band, they suggest that the spectral type of the companion is F8±2 and that it has a mass of $1.1 - 1.3\,\mathrm{M}_\odot$ using the catalogue of Jacoby et al. (1984). Mason et al. (2012) determine that the companion is of spectral type F3-G9 based on the presence of the G-band and the morphology of the Mg I lines. Other estimates of the spectral class of the companion include G3-6 (Schaefer 1990), G0±5 (Hanes 1985), K2 (Anupama & Dewangan 2000), and K0-G3 (Webbink et al. 1987). Clearly there is little consensus as to the nature of the companion, or the system as a whole in quiescence; this work will address the uncertainty regarding the nature of the companion, the mass accretion rate in quiescence, and the long term evolution of the system following outburst.

3.2 Observations

A series of observations was taken using VLT/XShooter and SALT/RSS, a summary of which can be seen in Table 3.1. These observations were proposed by the author and obtained in standard service mode by a resident astronomer. The VLT observations were obtained under proposal 087.D-0804(A) using the UVB, OPT, and NIR detectors, the SALT observations under proposal code 2012-1-UKSC-005 using the PG0900 grating. These observations were all taken after the V-band magnitude had returned to the quiescent level. The data were reduced using standard procedures in IRAF as described in Section 2.2.1. Phase 0.0 is defined as being when the companion appears directly in front of the WD to the observer as defined in Fig 3.1. The VLT and SALT data can be seen in Figs 3.2 and 3.3 respectively. Although the SALT data begin at ∼3200Å, the data short of 4000Å are very noisy and so are not displayed here, with the SALT data suffering from poor S/N in general. The gaps in VLT data are due to the removal of telluric features, gaps in SALT data are due to the detector consisting of three chips which do not cover a continuous wavelength range. The resolving power of the VLT data is ∼4300 from ∼3000-5500Å, ∼7500 from 5500Å-1μm, and ∼5000 from 1-2.5μm. The resolving power of the SALT data is ∼1000. The VLT data were wavelength calibrated using a ThAr lamp and flux calibrated using the standard stars LTT3218 and LTT7987. SALT data were wavelength calibrated using a ThAr lamp and flux calibrated using the standard star EG21. SALT data were reduced using IRAF rather than pySALT due to the author's familiarity with the former. Figs 3.4-3.18 show the variation with phase of: H Balmer lines; He II lines; Ca II, Mg I, and Na I lines; and H Paschen and H Brackett lines respectively.

For spectra obtained at the VLT an absolute flux calibration is possible, but for SALT spectra only a pixel-to-pixel calibration is possible. This means that for SALT spectra the flux level of the continuum is not reliable. However the shape of the continuum and the ratio of lines fluxes are reliable; therefore the difference in shape between the spectra displayed in Figure 3.3 can be assumed to be real. On each night the target was observed there was also an observation of a flux standard, with the exception of the SALT observation on 25/7/2012 when an observation of a flux standard did not take place until ∼3 weeks later. Although it is preferable for the flux standard to be observed on the same night as the target, the properties of the detector should not have changed in this time, and so other than a small change in airmass this should not be a problem. This should not cause any major errors during the analysis, although it is something to be aware of. The complex structure of the Balmer lines in the VLT data, and the difficulty in fitting them, will be a significant source of error.

Table 3.1: Observing Log

Orbital phase	λ range (Å)	Date of observation	Days since peak	Facility	Exposure (s)	Airmass
0.25	3300-25000	18/04/2011 06:55:15	445	VLT	1800	1.01
0.40	3300-25000	03/05/2011 05:57:16	460	VLT	1800	1.01
0.43	3300-25000	03/05/2011 07:05:19	460	VLT	1800	1.02
0.46	3300-25000	03/05/2011 07:58:46	460	VLT	1800	1.09
0.55	3213-6319	25/05/2012 01:13:30	848	SALT	2250	1.33
0.62	3300-25000	02/05/2011 07:13:12	459	VLT	1800	1.03
0.77	3213-6319	25/07/2012 21:06:32	909	SALT	2430	1.30

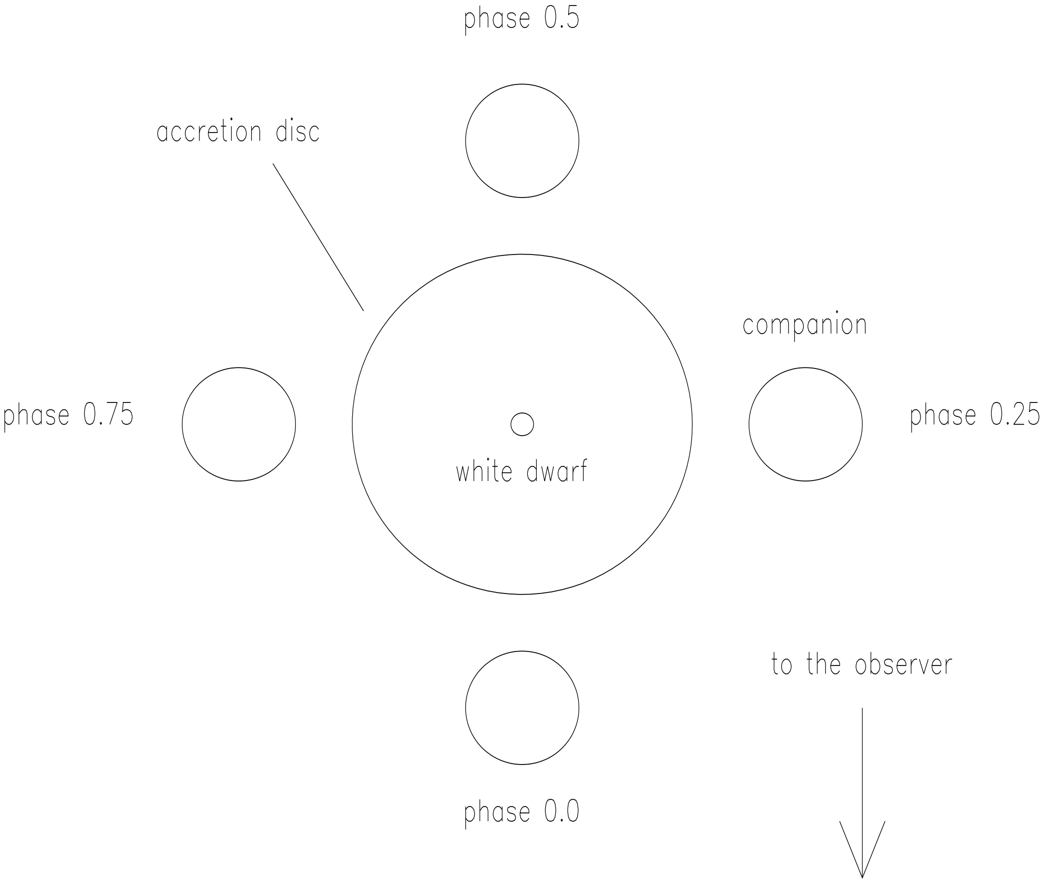

Figure 3.1: Orbital phases.

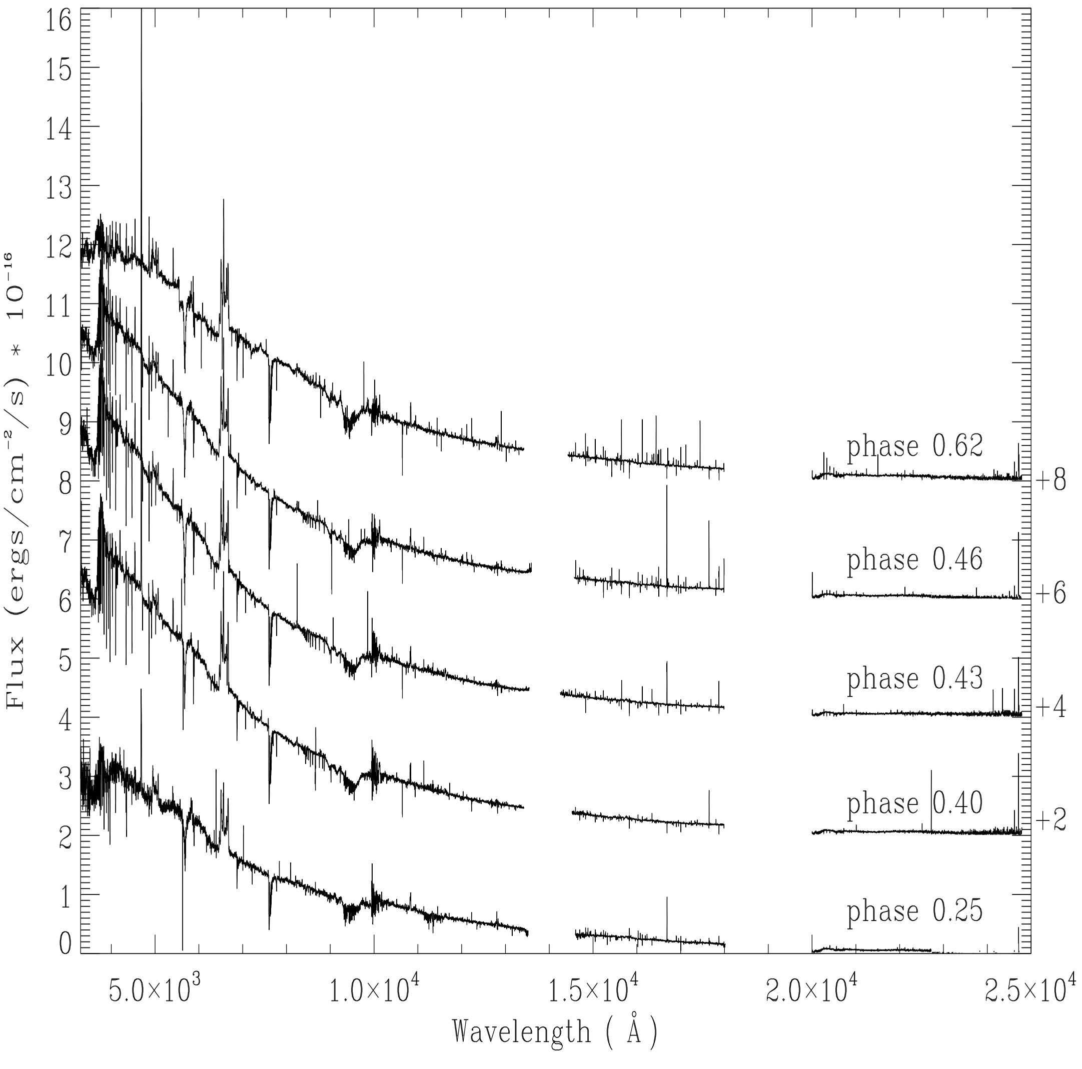

Figure 3.2: VLT spectra of U Sco. The offset is shown to the right of the figure.

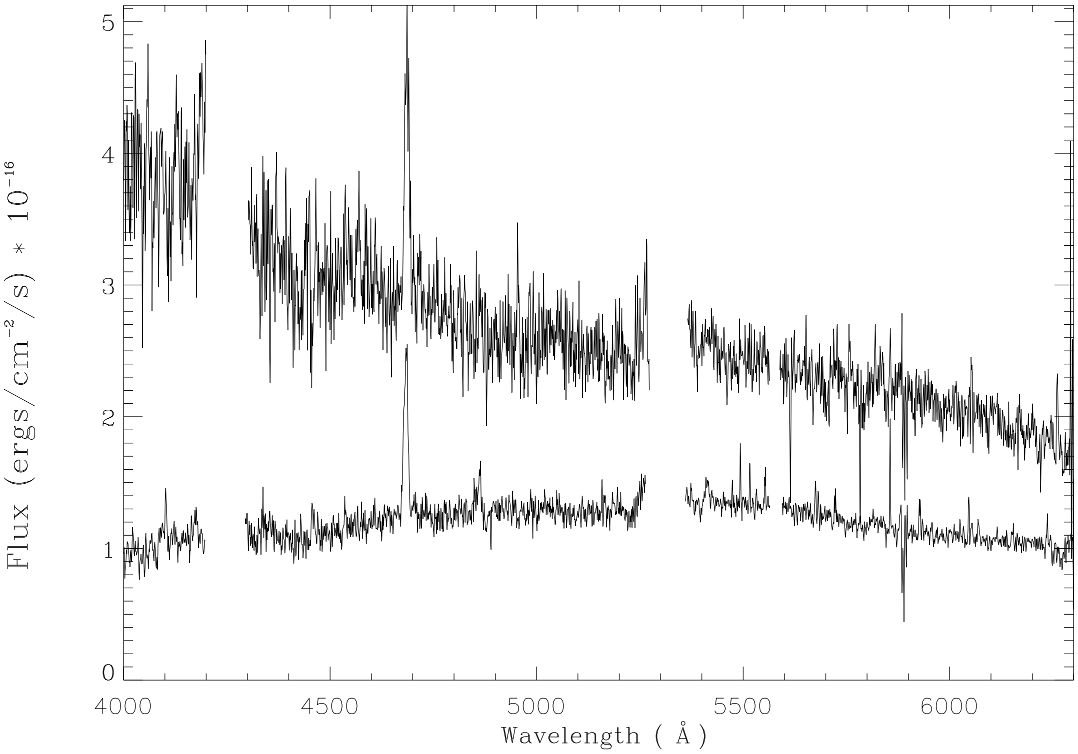

Figure 3.3: SALT spectra of U Sco taken at phase 0.77 (day 909, upper spectrum) and 0.55 (day 848, lower spectrum).

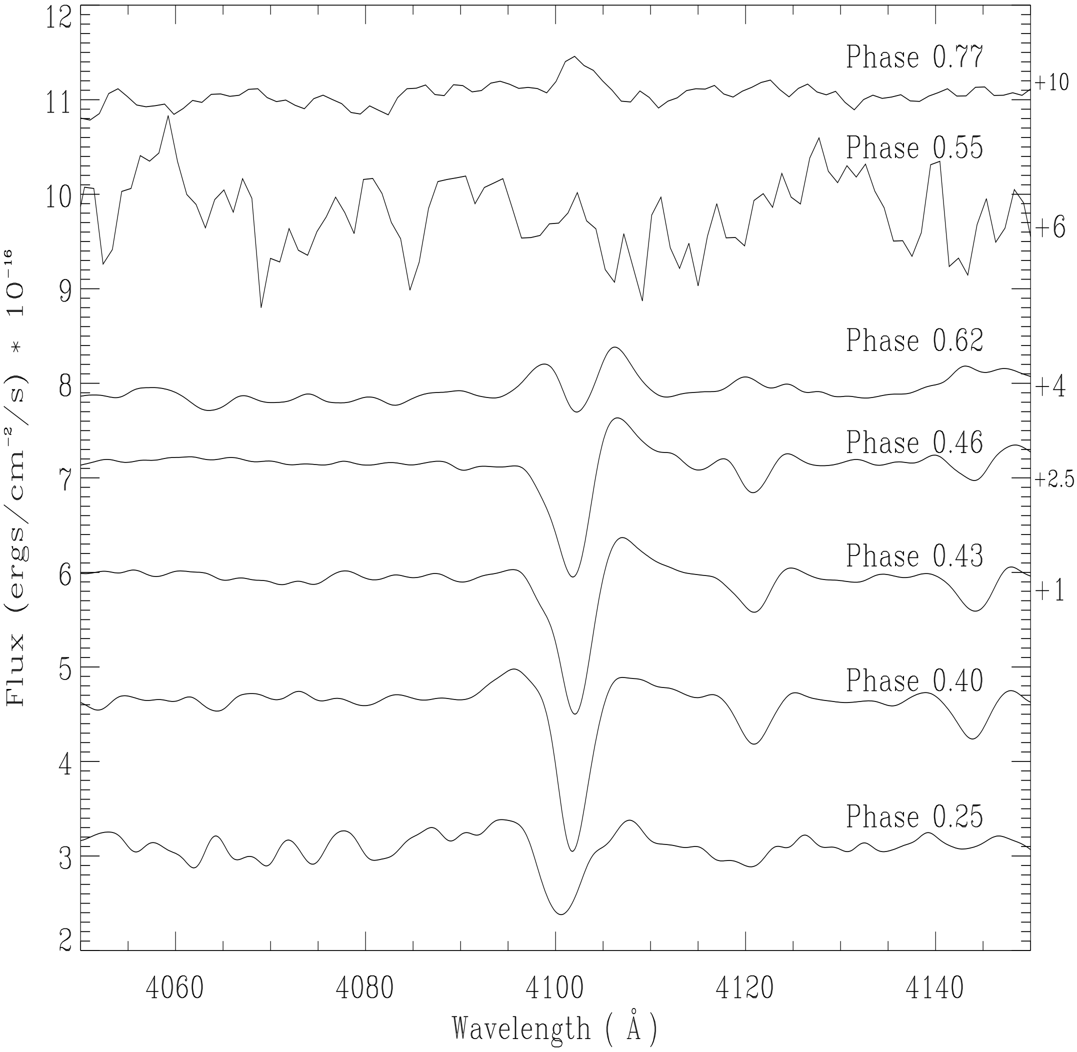

Figure 3.4: Hδ line profiles offset as indicated to the right of the figure. The orbital phase and number of days after outburst are indicated on the Y axis.

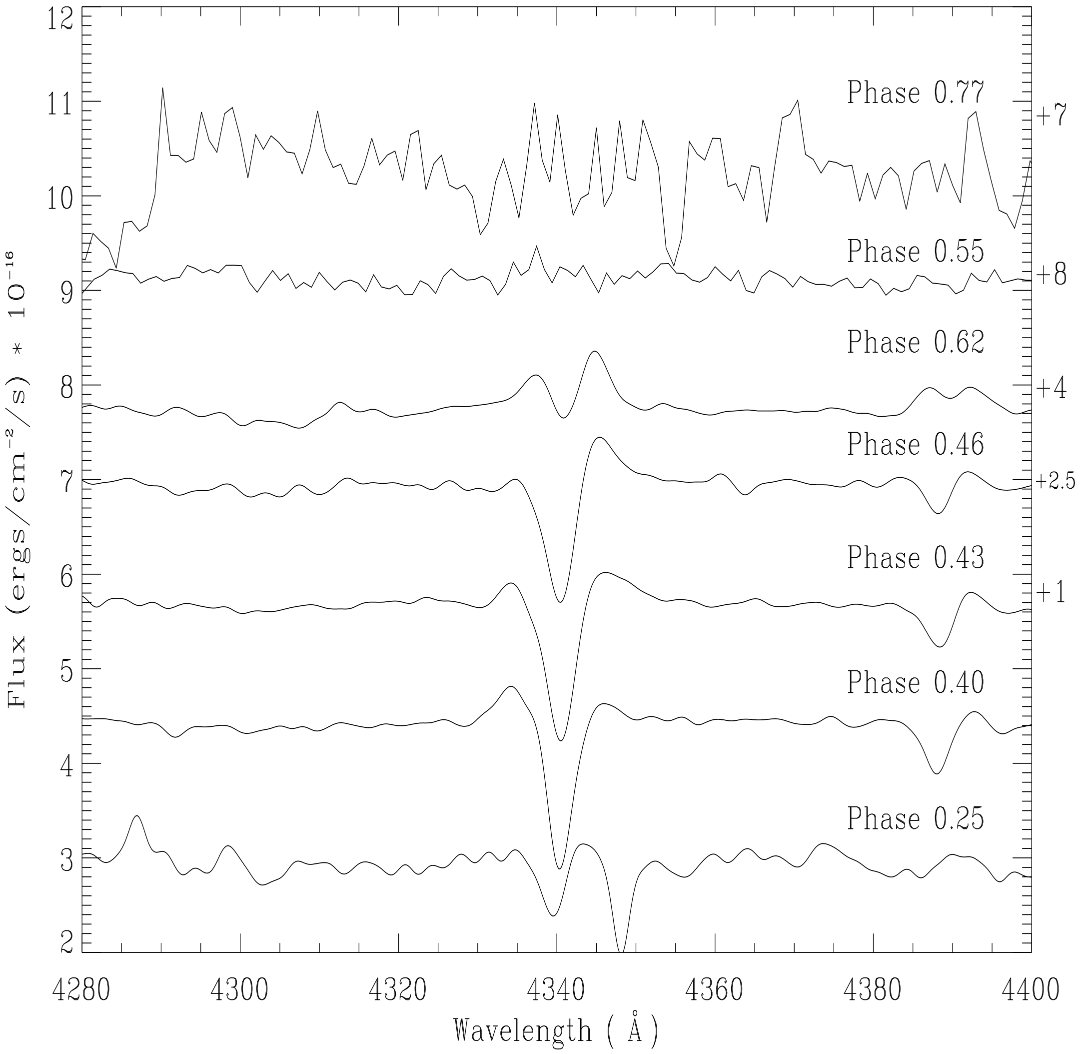

Figure 3.5: Hγ line profiles offset as indicated to the right of the figure. The orbital phase and number of days after outburst are indicated on the Y axis.

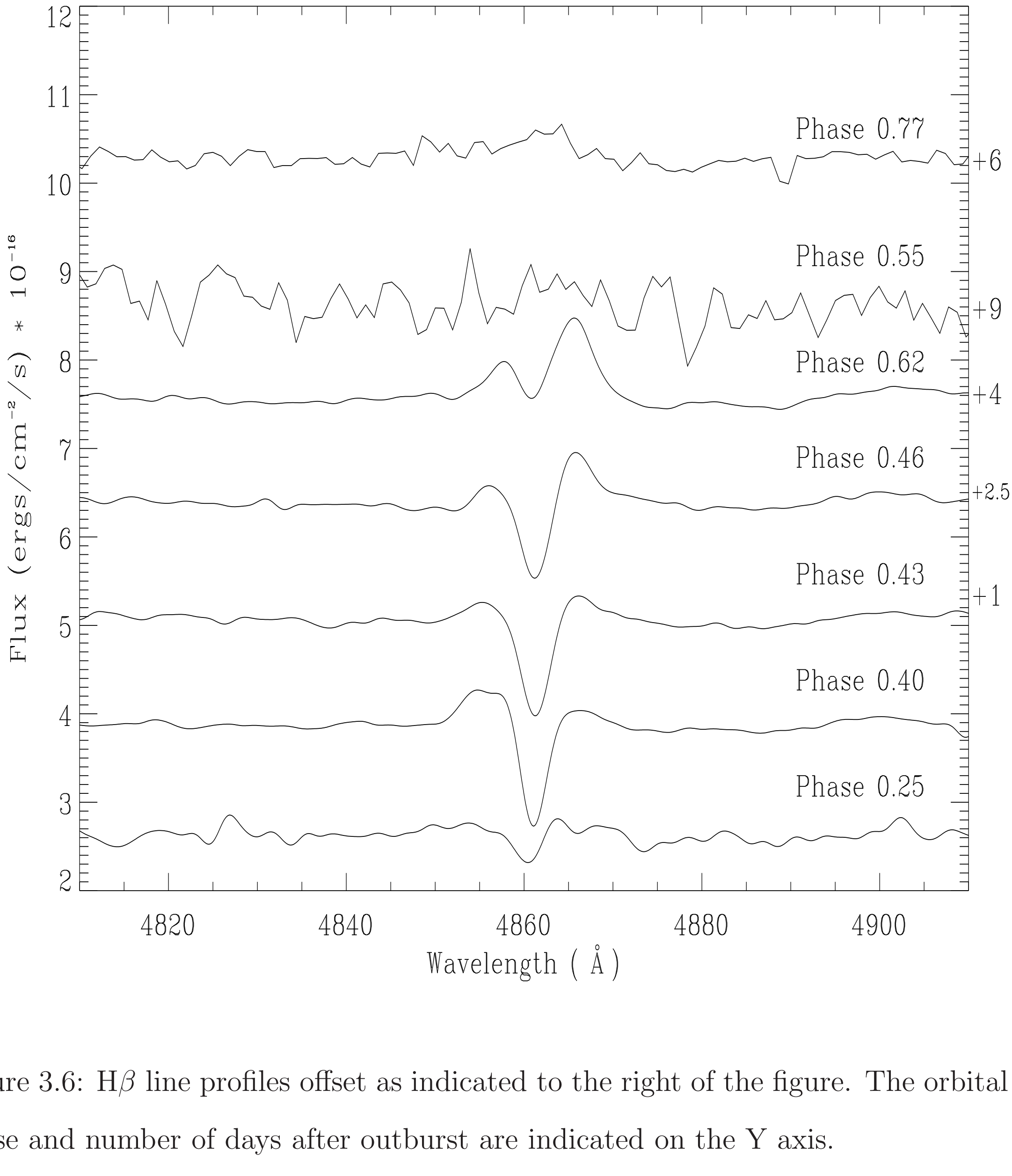

Figure 3.6: Hβ line profiles offset as indicated to the right of the figure. The orbital phase and number of days after outburst are indicated on the Y axis.

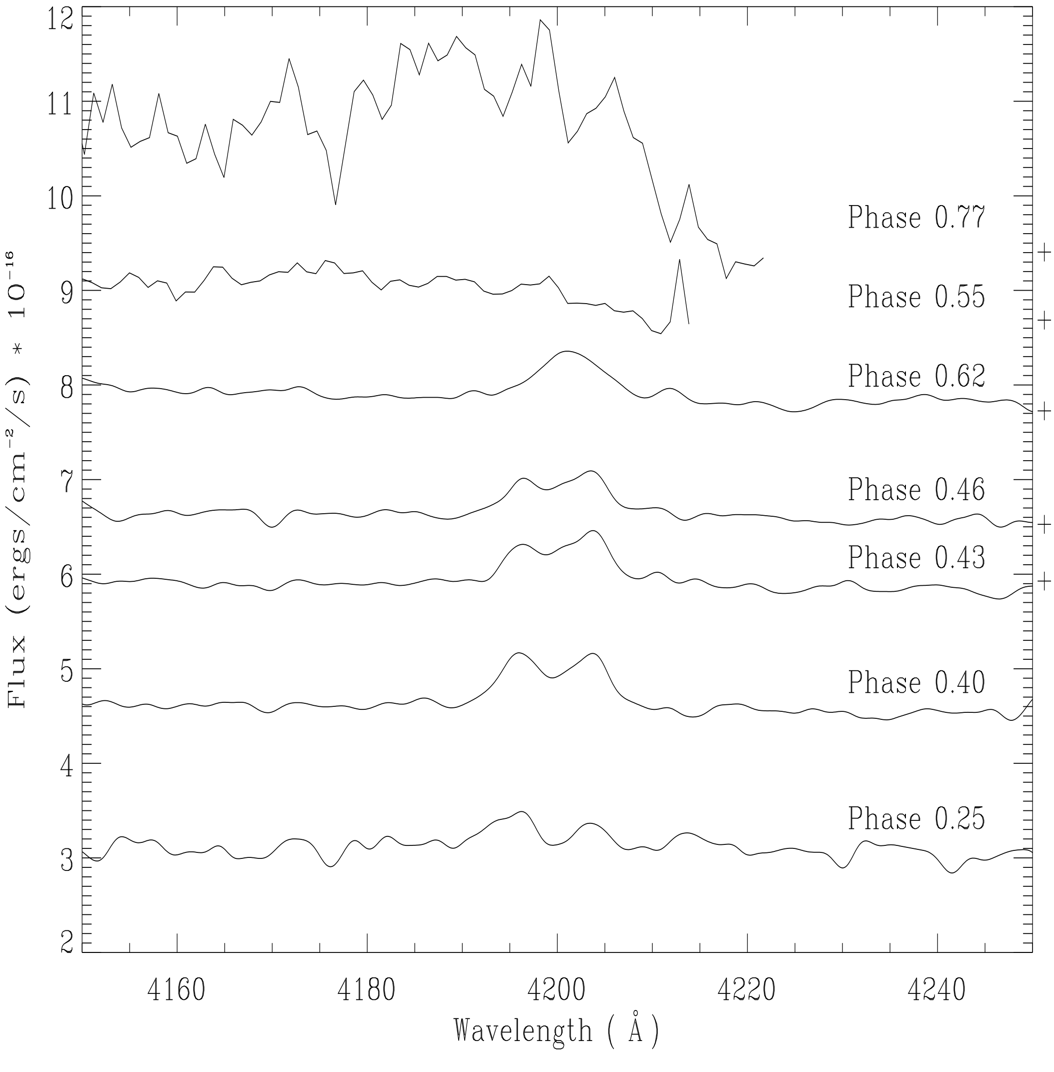

Figure 3.7: He II 4200Å line profiles offset as indicated to the right of the figure. The orbital phase and number of days after outburst are indicated on the Y axis.

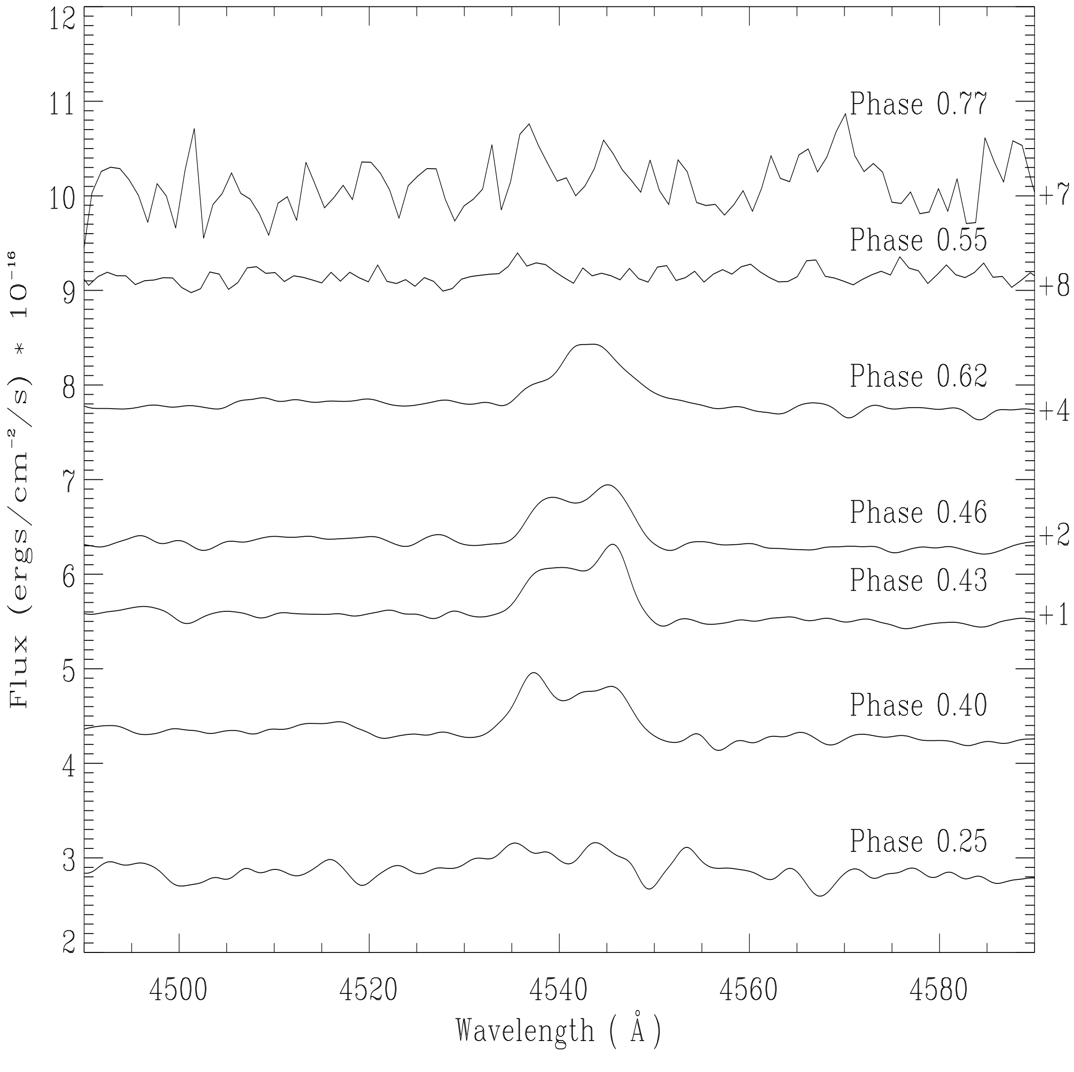

Figure 3.8: He II 4540Å line profiles offset as indicated to the right of the figure. The orbital phase and number of days after outburst are indicated on the Y axis.

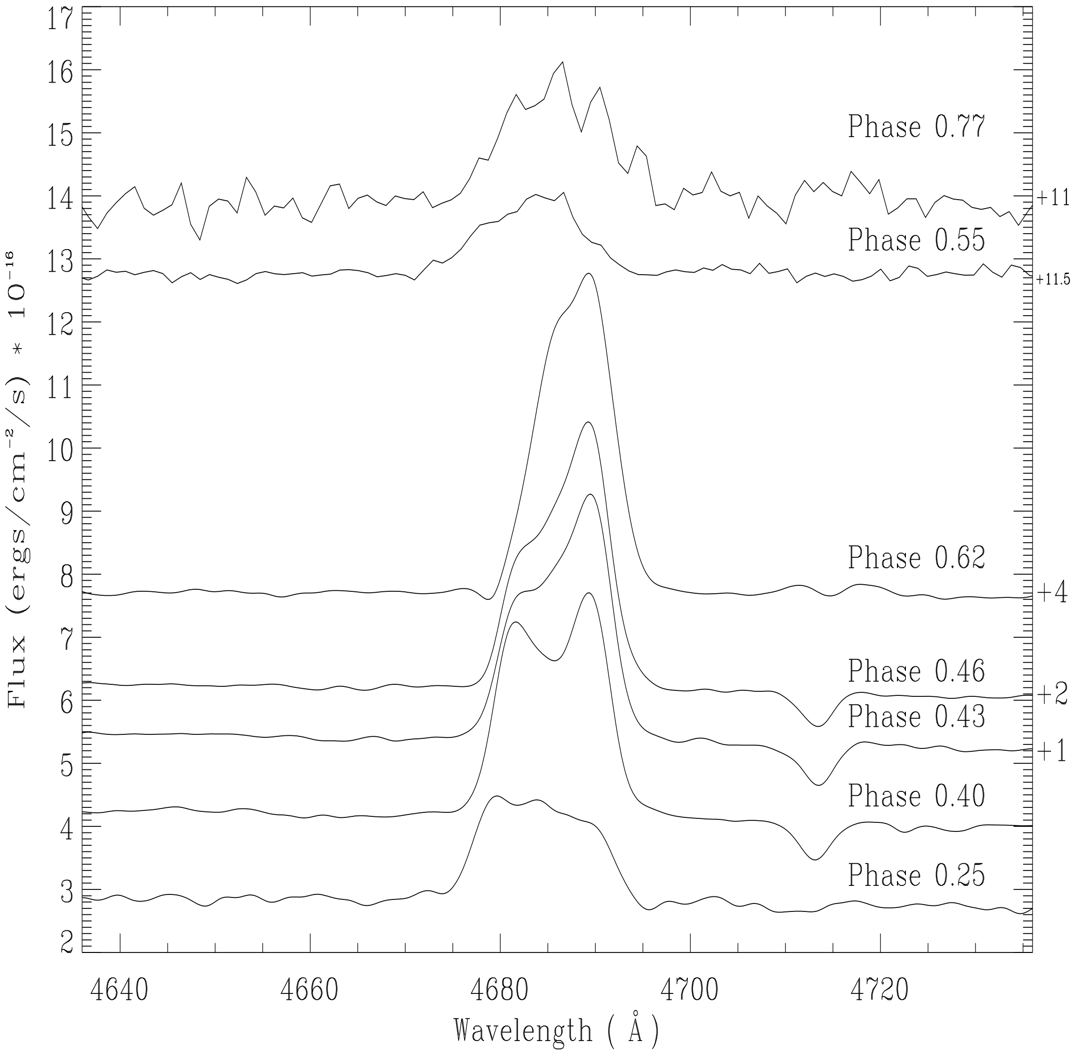

Figure 3.9: He II 4686Å line profiles offset as indicated to the right of the figure. The orbital phase and number of days after outburst are indicated on the Y axis.

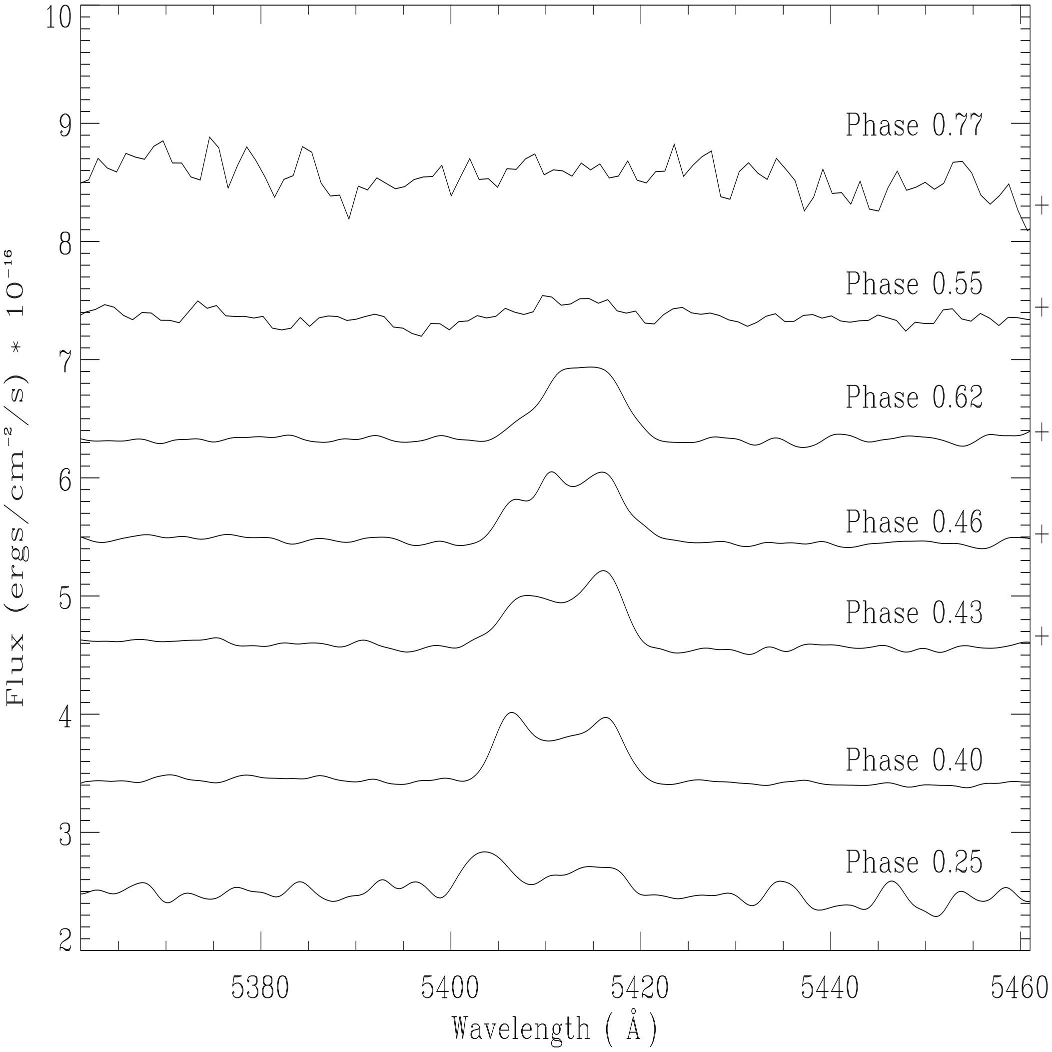

Figure 3.10: He II 5411Å line profiles offset as indicated to the right of the figure. The orbital phase and number of days after outburst are indicated on the Y axis.

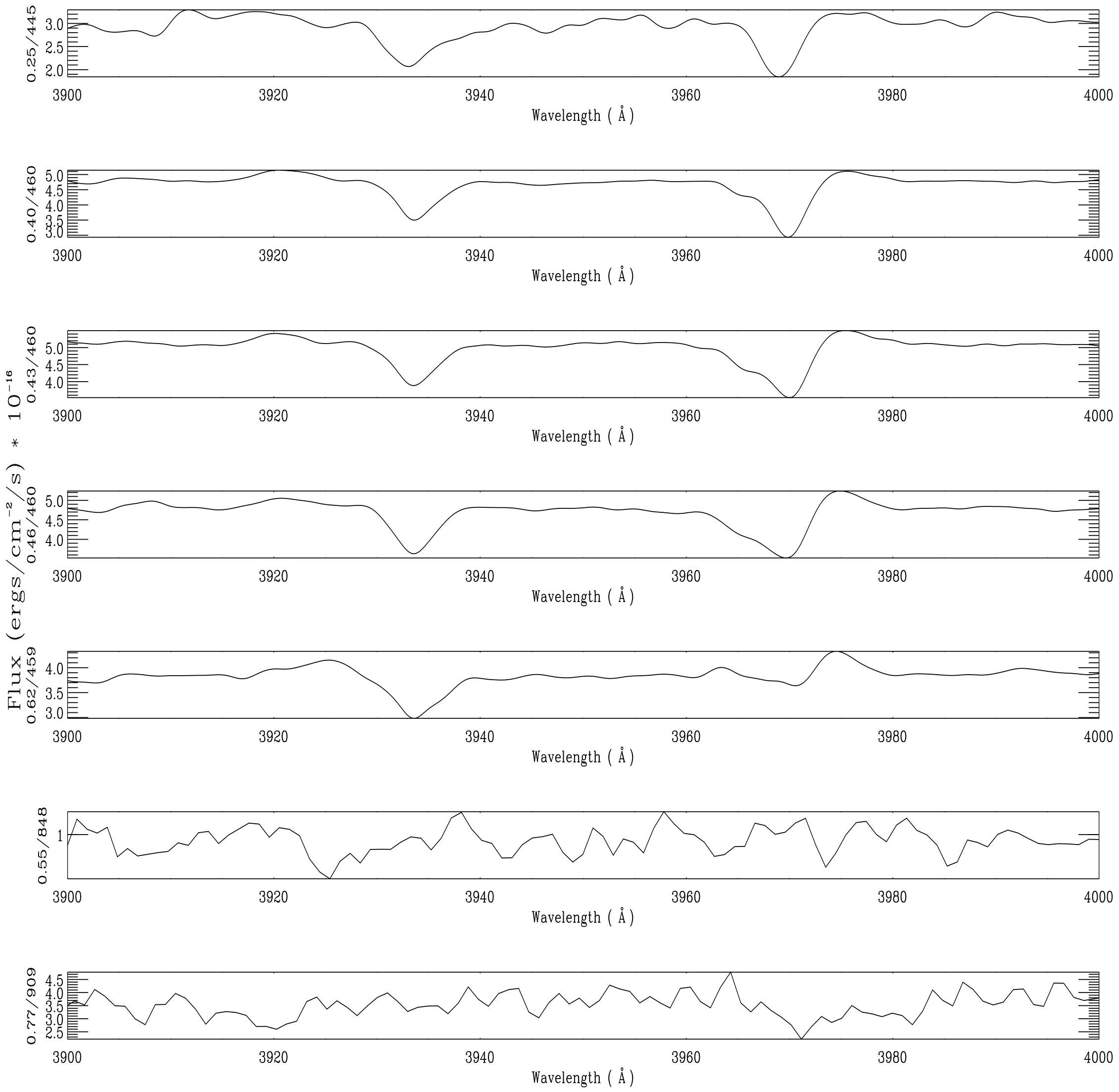

Figure 3.11: Ca II line profiles. The orbital phase and number of days after outburst are indicated on the Y axis.

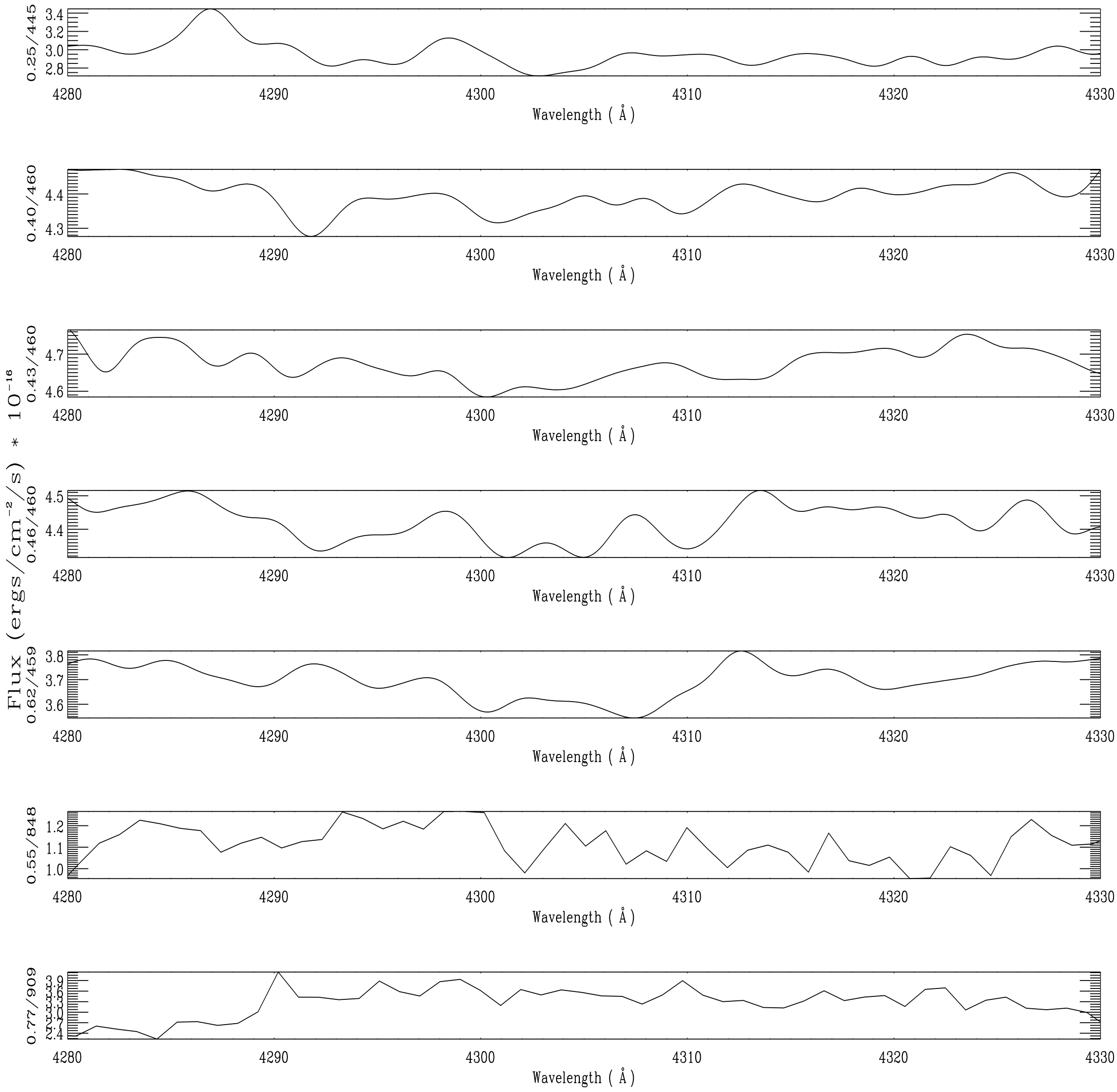

Figure 3.12: G band line profiles. The orbital phase and number of days after outburst are indicated on the Y axis.

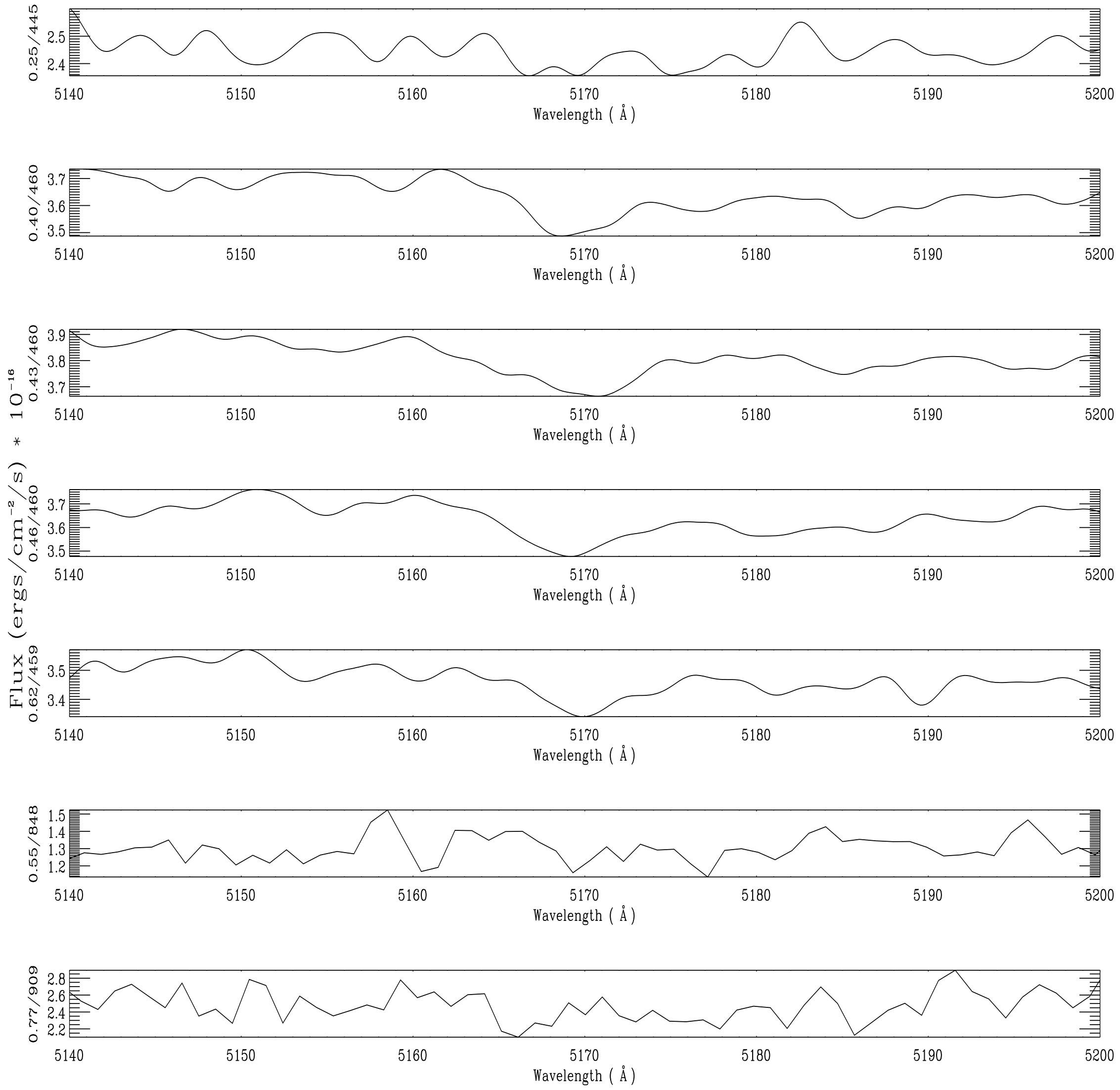

Figure 3.13: Mg line profiles. The orbital phase and number of days after outburst are indicated on the Y axis.

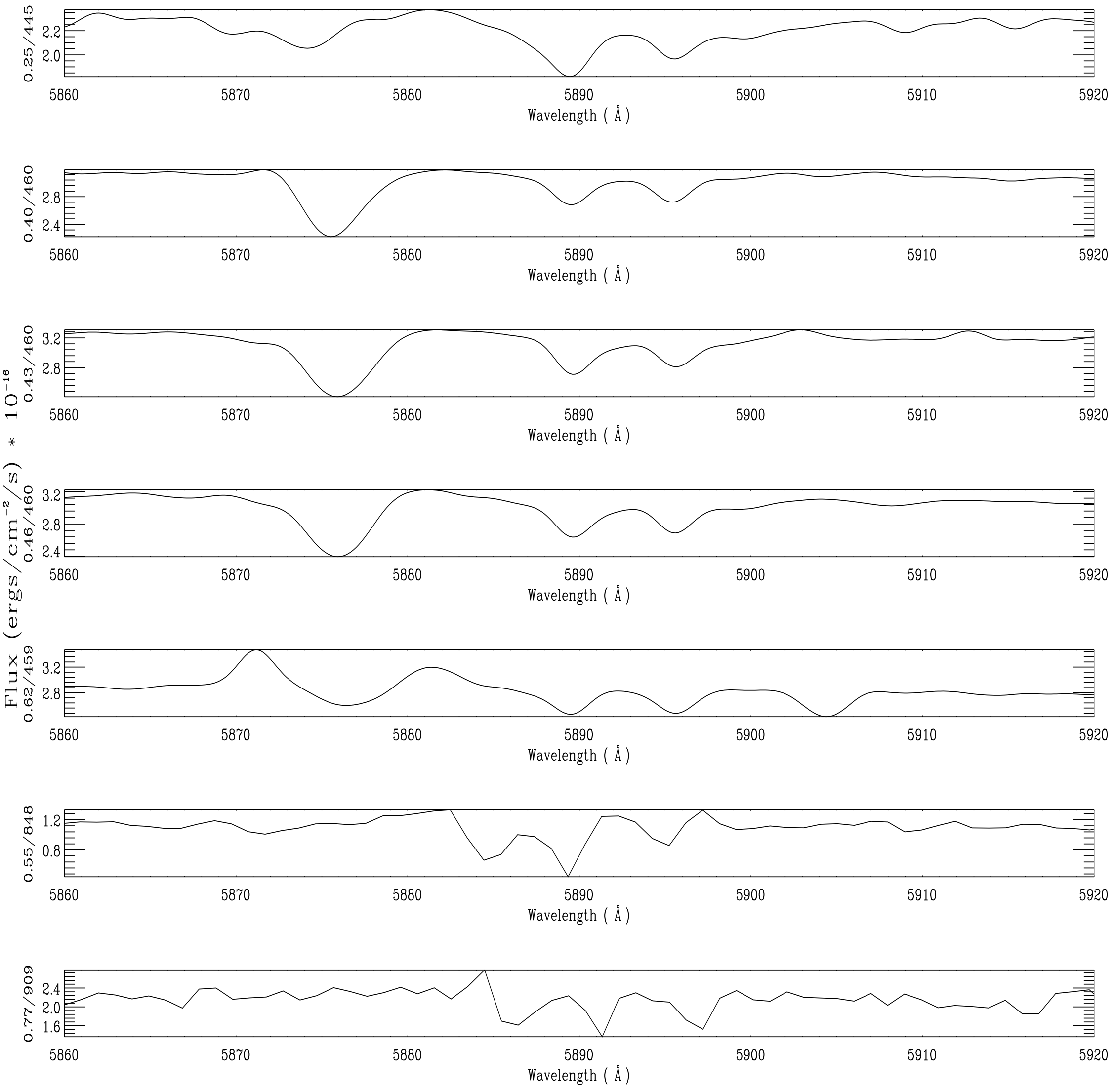

Figure 3.14: Na line profiles. The orbital phase and number of days after outburst are indicated on the Y axis.

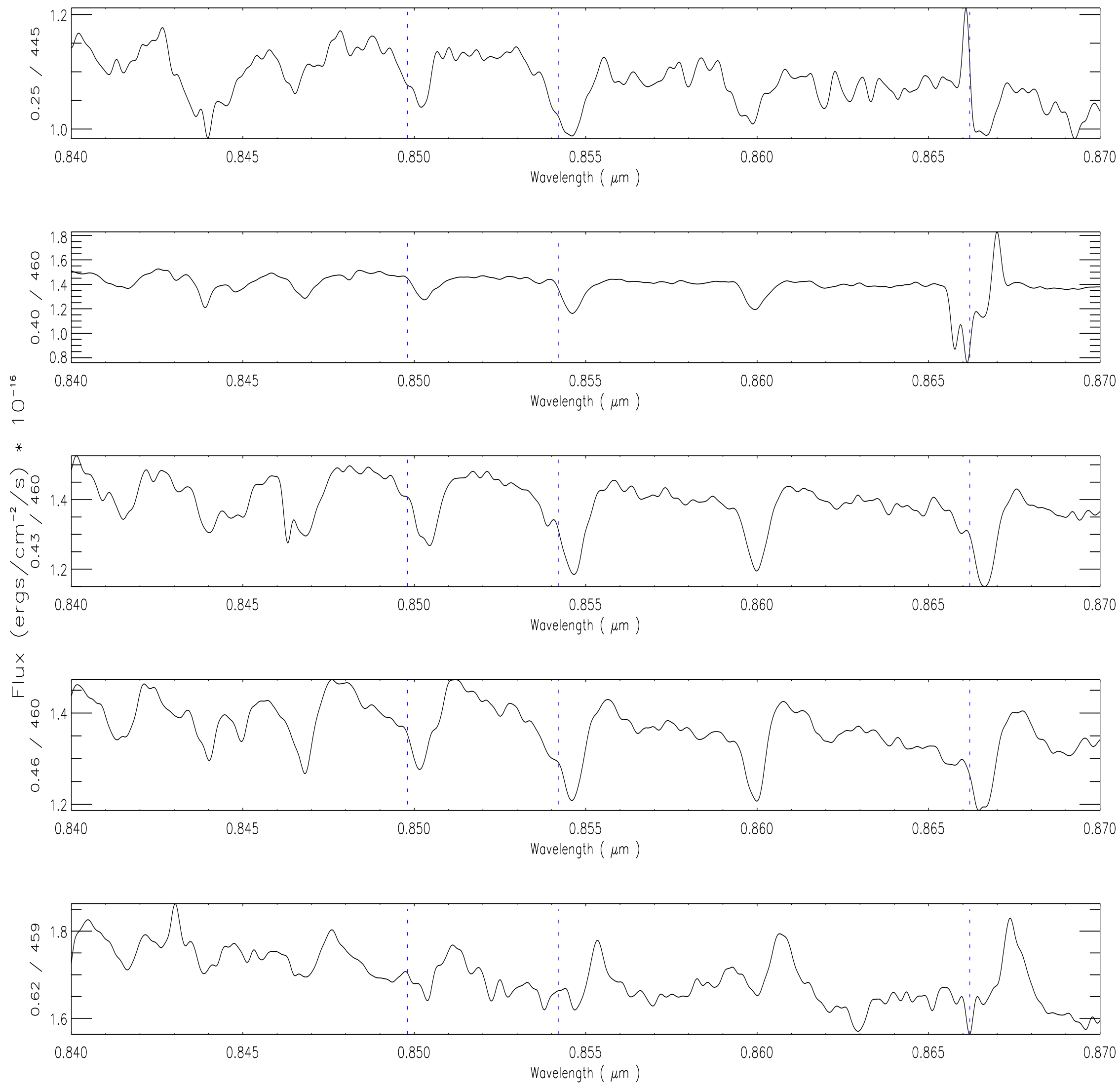

Figure 3.15: Paschen series line profiles. The orbital phase and number of days after outburst are indicated on the Y axis. The dashed blue lines indicate the rest wavelength of Ca II lines.

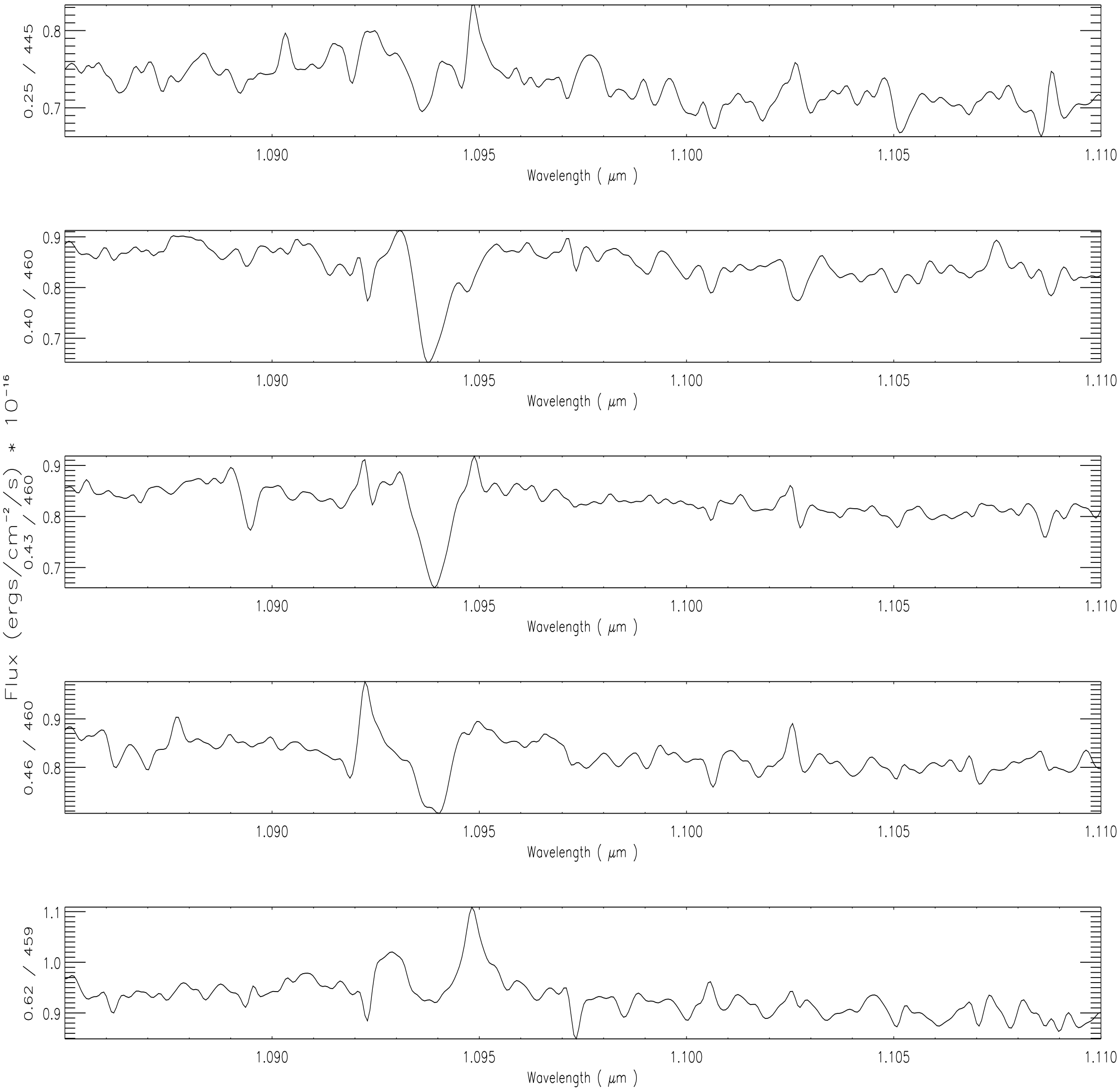

Figure 3.16: Paschen γ line profiles. The orbital phase and number of days after outburst are indicated on the Y axis.

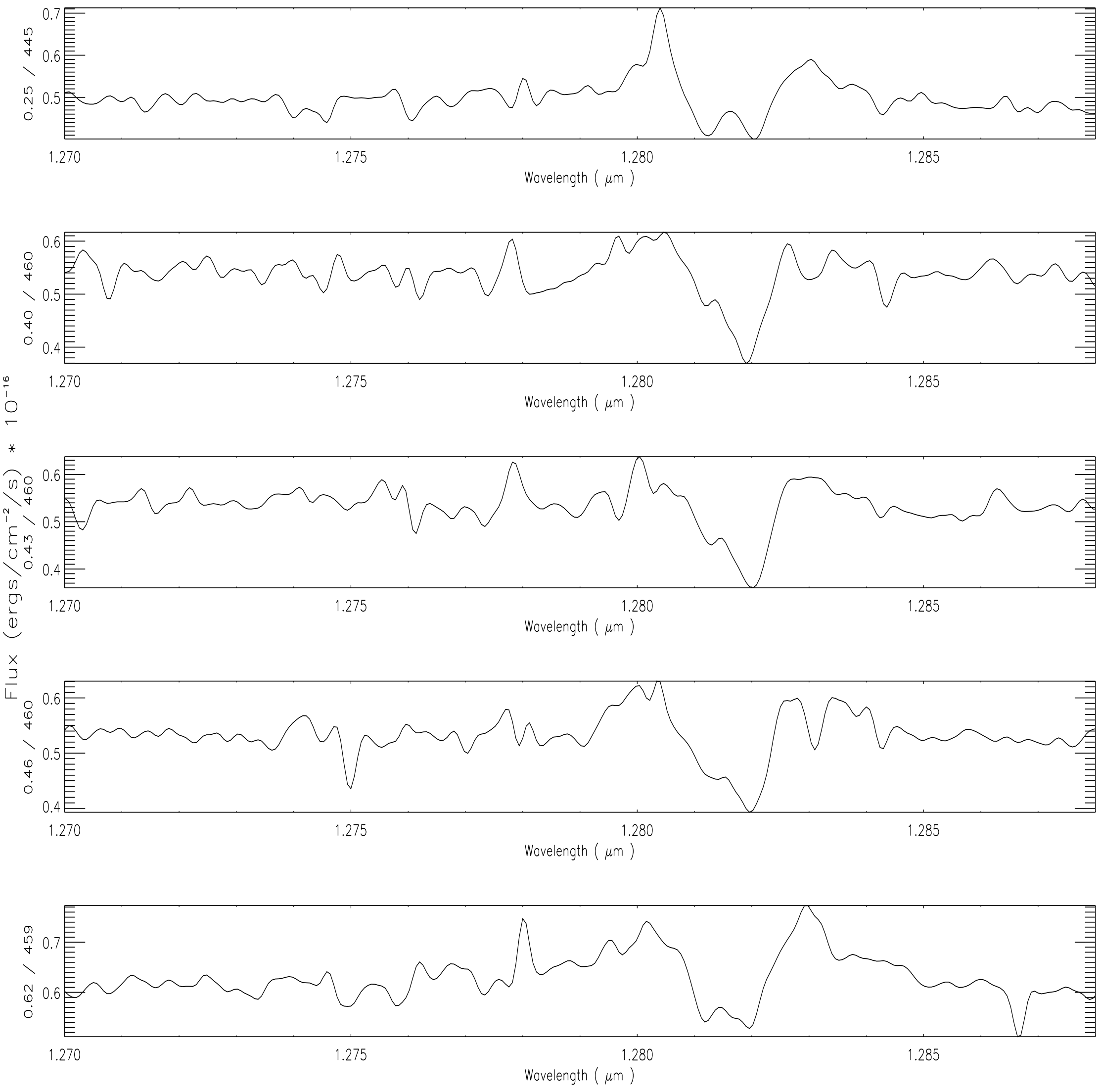

Figure 3.17: Paschen β line profiles. The orbital phase and number of days after outburst are indicated on the Y axis.

3.3 Results

3.3.1 Overview of spectra

The spectra taken at the VLT show many emission and absorption lines as well as a clear Balmer jump. H I, He I, and He II are observed, with high energy n-2 transitions of H I responsible for the Balmer jump at ∼3800Å. The He II feature at 4686Å is the dominant feature with He II 4200, 4542, and 5411Å also present. Other He II lines, if present, are blended with H I lines. There is clear variability in both the continuum and lines at different phases; this could be caused by phase related variations due to the companion and hot spot or long term variations due to changes in the accretion disc. The disc can vary on a timescale of hours causing the B band magnitude to vary at levels of up to ∼1 mag and the V band curve to vary at levels up to ∼0.4 mag (Schaefer 2010). This can be seen in the visual lightcurve (Fig 1.6), although given that these data comes from amateur observers the accuracy of the observations cannot be verified; the typical uncertainty given for AAVSO data is 0.1 mag[1].

The Balmer lines show both emission and absorption components, as can be seen in Figs 3.4-3.6, with the absorption component varying in both position and strength at different phases; the absorption component is slightly redshifted from the line centre at phase 0.40 and then moves bluewards as the companion moves behind the disc (Figs 3.4 - 3.6). By phase 0.62 the absorption component has become blueshifted from the line centre and weak. The H lines show an emission feature which varies with phase between being to the blue or red of the absorption feature; this absorption feature is consistent with a high-inclination, optically thick disc (Warner 1989) with a varying emission feature being consistent with a hot spot (Fig 1 of Robinson et al. 1994, see also Jovanović et al. 2010 and Mason et al. 2000).

---

[1] http://www.aavso.org/quickstart-guide-using-aavso-data

It is not clear if there is an absorption component present in the Balmer lines in the SALT data due to the poor S/N. The same behaviour is clearly present in the He II lines as can be seen in Figs 3.7-3.10. A different interpretation (S. Shore, private communication) is that the line profiles in the VLT spectra resemble those seen in shell stars, which could be reproduced in U Sco if the material accreted by the primary following an outburst does not settle into a disc immediately, but fills the Roche-lobe of the primary in a diffuse cloud before forming a disc. The line profiles in shell stars, such as ψ Per (Fig A.2. of Rivinius et al. 2006), show significant variation with excitation level which is clearly not the case for U Sco as can be seen in Figs 3.4 to 3.6; this discrepancy in the line profiles would seem to rule out this interpretation.

Comparing the VLT and SALT observations it is clear that they are similar in only a few ways. Although each set of observations was taken after the system had returned to the pre-maximum V band magnitude the VLT data are clearly very different from previous quiescent spectra (Johnston & Kulkarni 1992). Although the continuum level is consistent with the quiescent magnitude, several emission and absorption lines are present which are not seen in the spectra of Johnston & Kulkarni (1992). There is also a clear rise in the continuum at shorter wavelengths and a visible Balmer jump up to day 460, which is not seen in the quiescent spectra of Johnston & Kulkarni (1992). This indicates that the system returns to photometric quiescence before it returns to spectroscopic quiescence. Conversely, the SALT spectra appear quite similar to the spectra of Johnston & Kulkarni (1992), with few lines present and a much flatter continuum than in the VLT data. In both SALT observations the strongest feature is He II 4686Å; it is not clear if He II 5411Å is present due to its proximity to the edge of the detector chip. H Balmer lines are detected at phase 0.55 (day 848) in the SALT data but not at phase 0.77 (day 909); there is also a significant change in the shape and level of the continuum between the

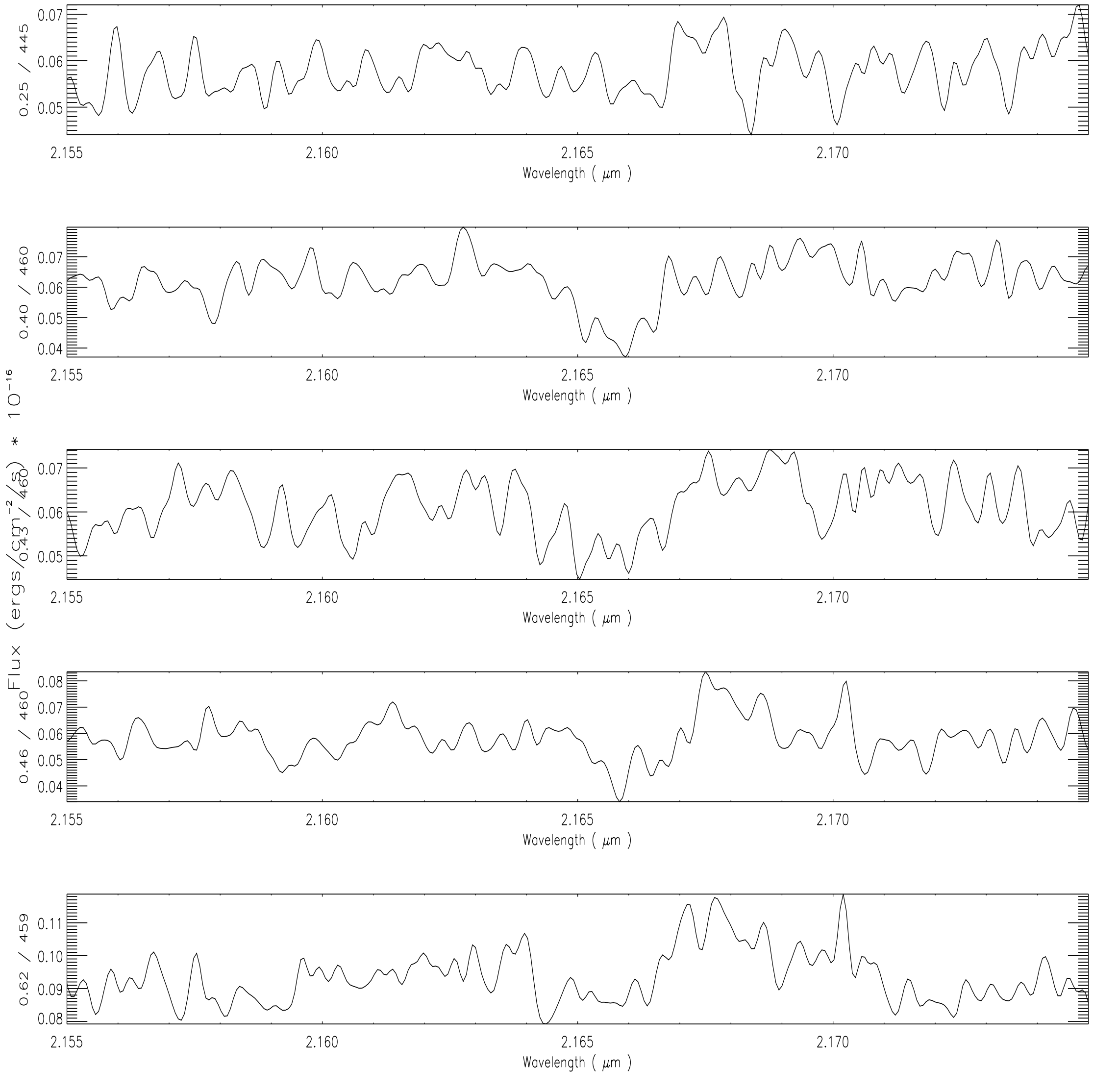

Figure 3.18: Brackett γ line profiles. The orbital phase and number of days after outburst are indicated on the Y axis.

two SALT observations. At phase 0.55 (day 848) the companion is almost entirely behind the accretion disc, whereas at phase 0.77 (day 909) they are side by side. Both of these changes could be due to the difference in flux from the companion, although longer term variations could also be responsible.

Both H and He lines in the VLT data show an absorption component and an emission component. The flux of these two components can be estimated using the ELF (emission line fitting) package in DISPO[2] using the following method: first the absorption component is snipped from the data and the continuum removed, leaving only the wings of the feature. A Gaussian profile can then be fitted to these wings to produce an estimated emission feature. Subtracting this fit from the snipped feature then produces a fit to the absorption core. The ELF procedure gives the flux and errors of these fits, allowing the emission of each line to be estimated even though there is significant absorption. The absorption component is strongest at phase 0.5, getting weaker as the companion becomes more visible. Fitting the features in this manner allows the ratios to be compared to the recombination coefficients of Hummer & Storey (1987) to see if case B recombination applies. For He II the lines at 4200, 4542, and 5411Å can be shown to have ratios consistent ($1 \leq R_{HeII}/R_{caseB} \leq 2$) with case B ratios (Table 3.2), however He II 4686Å cannot ($R_{HeII}/R_{caseB} \simeq$ 3-5), indicating that case B recombination does not apply and that the line is optically thick. Possible reasons for this are discussed in Section 3.4.

The He II emission has been shown by Patterson & Raymond (1985) to be an indicator of mass accretion. From the luminosity of the He II 4686Å line the mass accretion rate in U Sco can be estimated to be $\sim 10^{-7}\,\mathrm{M}_{\odot}\,\mathrm{yr}^{-1}$ using

$$L_{4686} = 1.3 \times 10^{29} \dot{M}_{16}^{0.78}\,\mathrm{ergs\,s^{-1}}, \tag{3.1}$$

where $\dot{M}_{16}$ is the mass accretion rate in units of 10^{16} g/s, as shown in Table 3.3.

---

[2] http://www.starlink.rl.ac.uk/docs/sun50.htx/sun50.html

Table 3.2: Ratios of helium lines with comparison to case B ratios.

Lines	0.25	0.40	0.43	0.46	0.62	Case B ratio
4200/4542	0.762	0.877	0.772	0.817	0.667	0.692
4200/4686	0.221	0.168	0.158	0.134	0.084	0.037
4200/5411	0.369	0.690	0.772	0.521	0.563	0.391
4542/4686	0.291	0.192	0.205	0.163	0.125	0.053
4542/5411	0.485	0.787	1.000	0.637	0.843	0.565
5411/4686	0.599	0.243	0.205	0.256	0.149	0.094

Because He II 4686Å is optically thick this mass accretion estimate is a lower limit. Patterson & Raymond (1985) also show that in close binaries, since the He II 4686Å flux is due to irradiation from the boundary layer, the flux of that line is an indicator of the soft X-ray flux. U Sco has not been detected in X-rays in quiescence, which is consistent with a distance of 12±2 kpc (Schaefer 2010). However, if the soft X-ray flux can be predicted from the He II 4686Å flux then an estimate can be made of the integration time required in order for current instruments to observe U Sco in X-rays in quiescence.

Patterson & Raymond (1985) also show that the temperature of the boundary layer can be estimated using

$$T_{BL} = 2.16 \times 10^5 M_{0.7}^{0.86} \dot{M}_{18}^{0.18} \mathrm{K} \tag{3.2}$$

and that the soft X-ray flux (0.12 - 1 keV) can be estimated by

$$F_{sx} = 2.1 \times 10^{-12} \dot{M}_{17.5}^{2.1} M_{0.7}^{8} d_{200}^{-4.5}\, \mathrm{ergs\,cm^{-2}\,s^{-1}} \tag{3.3}$$

where M_x is the mass of the white dwarf in units of x solar masses, $\dot{M}_x$ is the mass accretion rate in units of 10^x g/s, and d_{200} is the distance in units of 200 parsecs,

Phase	L ($\mathrm{ergs\,s^{-1}}$)	$\dot{M}(M_{\odot}yr^{-1})$
0.25	$4.47\pm0.12\times10^{31}$	$2.81\pm0.03\times10^{-7}$
0.40	$11.1\pm0.14\times10^{31}$	$9.09\pm0.01\times10^{-7}$
0.43	$9.34\pm0.14\times10^{31}$	$7.22\pm0.01\times10^{-7}$
0.46	$9.43\pm0.14\times10^{31}$	$7.39\pm0.01\times10^{-7}$
0.55	$2.56\pm0.10\times10^{31}$	$1.38\pm0.04\times10^{-7}$
0.62	$8.42\pm0.10\times10^{31}$	$6.29\pm0.01\times10^{-7}$
0.77	$4.12\pm0.28\times10^{31}$	$2.56\pm0.07\times10^{-7}$

Table 3.3: Mass accretion rates derived from He II 4686Å flux.

provided that these quantities ≃1. In U Sco these quantities are much larger and so the soft X-ray flux cannot be estimated in this way. The luminosity of the He II 4686Å line is also related to the hard X-ray flux by

$$L_{4686} = 6.4\times10^{-5}L_x. \tag{3.4}$$

The measured luminosities and the derived mass accretion rates at each phase can be seen in Table 3.3. From these mass accretion rates the temperature of the boundary layer is found to be $\sim7\times10^5$ K using Equation 3.2.

3.3.2 Velocities

The full width at zero intensity (FWZI) of a line gives the maximum velocity of the emitting material; the velocity of each H and He II line in the spectra can be seen in Table 3.4. Using these velocities, along with the profile of each line, a picture of the geometry of the system can be built up. Each FWZI was measured by fitting a Gaussian profile to the emission line and observing by eye where the intensity falls to zero. As can be seen in Table 3.4, the velocities are consistent both between different lines and within the same line at different phases. The major exception to this is He II 4686Å; every other line experiences a reduction in velocity at later times (days 848 and 909), although the line velocities in the SALT data are difficult to determine due to the poor S/N. Thoroughgood et al. (2001) find the FWZI of He II 4686Å and 5411Å to be $1600\pm100\,\mathrm{kms^{-1}}$ and $1500\pm300\,\mathrm{kms^{-1}}$ respectively, consistent with these observations.

3.3.3 Disc modelling

In order to investigate the physical parameters of the system a model of the system needs to be produced. There are several components which can be considered for inclusion in the model: the white dwarf, the boundary layer, the hot spot, the accretion disc, and the companion star (Fig 3.19). The spectra which will be modelled have a wavelength range of 3300-25000Å. Therefore the white dwarf is not included in the model as the peak of the emission is expected to be at a shorter wavelength than 3300Å: the peak for a WD of temperature 10,000 K would be at ~2900Å, with a WD at 10^5 K peaking at ~290Å. Additionally, white dwarfs are generally low luminosity objects, as demonstrated by Torres et al. (2013), and are therefore unlikely to have a significant contribution to the optical continuum. The boundary layer is assumed to have a luminosity too low in the optical/near-IR to contribute to the continuum, with $\leq 1\%$ of the boundary layer output typically being in the optical (Godon & Sion 2005). Although the boundary layer may contribute significantly to line fluxes the contribution to the continuum is assumed not to be significant, as the majority of the emission is in the UV/X-ray (Shakura & Sunyaev 1973; Lynden-Bell & Pringle 1974). The accretion disc and the companion are therefore the two components which are included in the model. A series of blackbody fits were first used to model the spectra, before moving onto using a grid of model stellar atmospheres.

Table 3.4: Maximim emission line velocities for H Balmer and He II from FWZI measurements ($\mathrm{km\,s^{-1}}$)

Phase	0.25	0.40	0.43	0.46	0.55	0.62	0.77
Hβ	1200±400	1300±100	1500±100	1100±200	800±400	1400±200	-
Hγ	1400±100	1400±200	1500±100	1200±100	800±200	1200±200	-
Hδ	1400±200	1700±200	1200±200	1200±200	700±300	1400±200	-
He II 4200Å	1300±100	1500±200	1100±100	1200±200	-	1100±200	-
He II 4542Å	1000±200	1300±200	1200±200	1200±200	-	1300±300	-
He II 4686Å	1300±100	1400±200	1200±200	1300±100	1500±100	1100±100	1600±200
He II 5411Å	1200±200	1100±200	1200±200	1200±200	1000±300	1000±100	-
Facility	VLT	VLT	VLT	VLT	SALT	VLT	SALT
Day	445	460	460	460	848	459	909

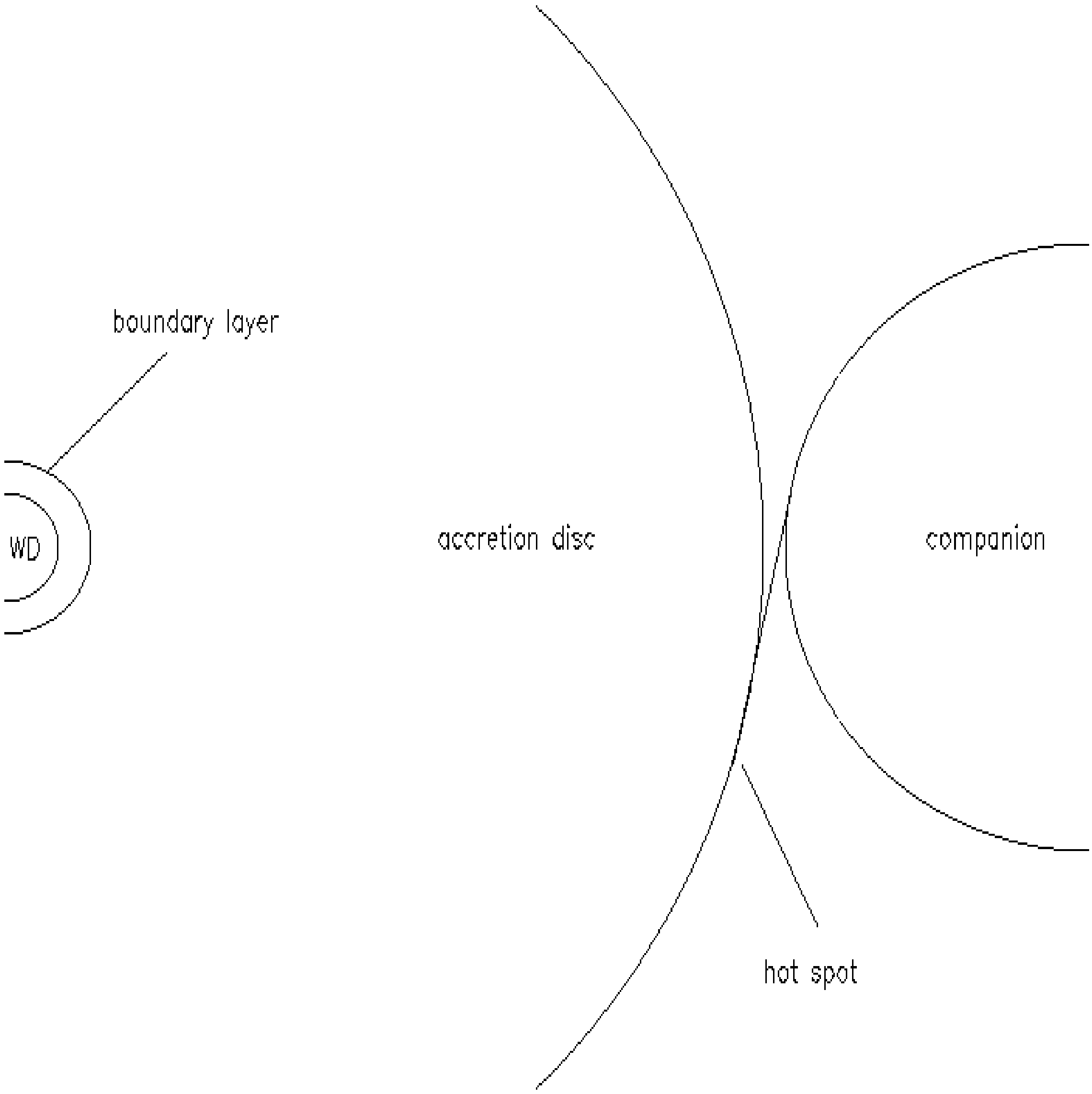

Figure 3.19: Schematic diagram of U Sco (not to scale).

Blackbody fits

Initially the spectra were modelled using blackbody fits, as outlined by Warner (2003). A series of blackbodies are used to represent the accretion disc with a single blackbody representing the companion. The accretion disc rings are each of thickness δr and form a disc up to a radius r. Each annulus is represented by a blackbody described by

$$B_\lambda(T) = \frac{2hc^2}{\lambda^5} \frac{1}{e^{\frac{hc}{\lambda kT}} - 1}, \tag{3.5}$$

where h is Planck's constant, c is the speed of light, k is Boltzmann's constant, and T is the temperature. The entire disc is represented by

$$F_\lambda = \frac{2\pi \cos(i)}{D^2} \int_{R_{acc}}^{R_d} B_\lambda(T_{eff}(r)) r dr, \tag{3.6}$$

where D is the distance to the object in parsecs, R_{acc} is radius of the white dwarf, R_d is the radius of the disc, i is the inclination, and the effective temperature, T_{eff}, is determined by

$$T_{eff} = T_* \left(\frac{R_{acc}}{r}\right)^{3/4} \left(1 - \left(\frac{R_{acc}}{r}\right)^{1/2}\right)^{1/4}, \tag{3.7}$$

and T_* is found using

$$T_* = 4.10 \times 10^4 R_9^{-3/4} M_1^{1/4} \dot{M}_{16}^{1/4} = 2.05 T_{max}, \tag{3.8}$$

where R_9 is the white dwarf radius in units of 10^9cm, M_1 is the white dwarf mass in solar masses, $\dot{M}_{16}$ is the mass accretion rate in units of $10^{16} gs^{-1}$, and T_{max} is the maximum temperature in the disc. A full derivation and discussion of these equations can be found in Warner (2003).

The companion is described using a single blackbody as described in Equation 3.5. The full model spectral energy distribution (SED) for the disc is added to the model SED for the companion and this composite model is then scaled to the observation using a χ^2 minimisation. A free scaling parameter is also included to allow the relative contributions of the companion and the disc to vary. The parameters for the χ^2 minimisation are shown in Equations 3.9 to 3.16. Although these models are capable of fitting the observed data there is a lack of physics included; even if the models can give effective temperatures if there is no physics included in the model then it is more difficult to understand the processes behind the observed behaviour. The effectiveness of fitting the spectra in this manner is also limited by the fact that the peak of the continuum is not present in the spectra; when fitting the Rayleigh-Jeans tail it is difficult to constrain an upper limit for the peak temperature if this peak is at a shorter wavelength than the limit of the data. The best fit to U Sco at phase 0.40 is shown in Figure 3.20.

In order to make the model more sophisticated and to account for more of the physical processes involved, the blackbody fits were replaced with model atmospheres. These model atmospheres, produced by Kurucz (1992), comprise a grid of several thousand models across a range of temperature, metallicities, and surface gravities.

Model atmospheres

The spectral type of the companion in U Sco is poorly constrained. By fitting the continuum with a pair of models, one composite model for the accretion disc consisting of several annuli and a single model stellar atmosphere for the companion star, it is possible to constrain the temperature of both components. A third model atmosphere to represent the white dwarf is not included since the effective temperature of the primary is high enough, up to 10^6 K by day 35 following the 2010 outburst (Orio et al. 2012), that it will not make a significant contribution to the continuum in the region of interest; WD temperatures in CVs are typically 10^4-10^5 K (Szkody

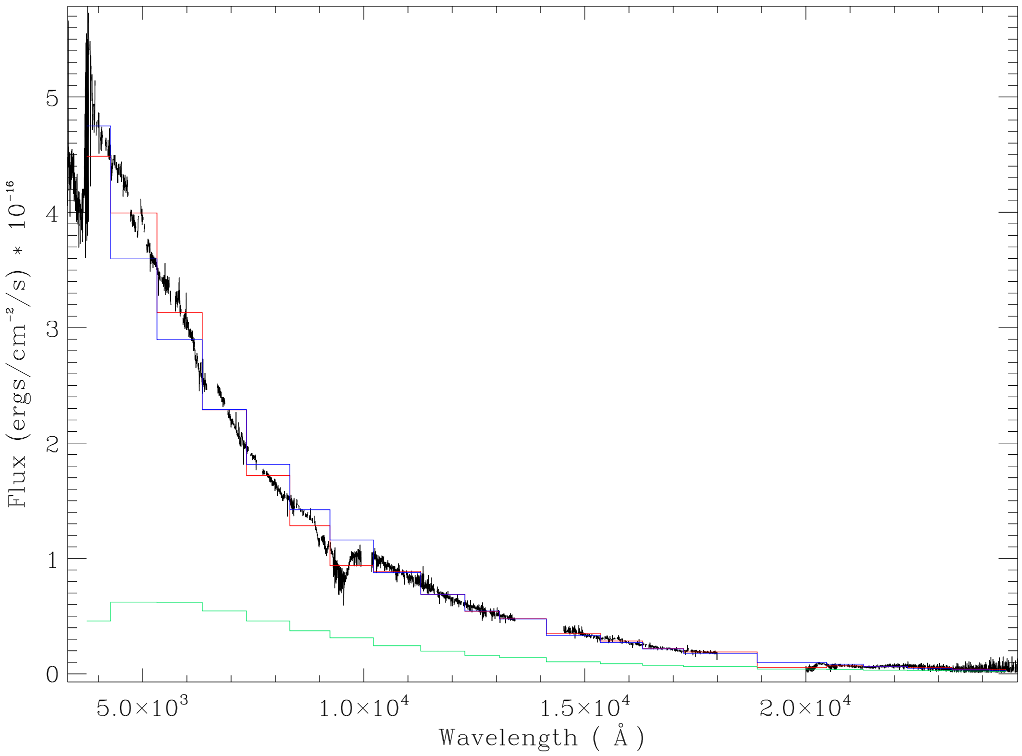

Figure 3.20: Best fit blackbody model (blue) to the binned spectrum (red) at phase 0.40. The contribution of the companion is shown in green.

et al. 2002; Townsley & Bildsten 2003). There are several spectral lines, such as Mg I and Ca II, which are also useful in spectral class diagnostics and which can be used to help constrain the effective temperature of the companion.

The model atmospheres used here come from a grid produced by Kurucz (1992) using the ATLAS code. Here only models with a solar metallicity were used, with the full range of temperatures (T = 3500-60000 K) and surface gravities ($\log(g)$ = 0.0-5.0) being investigated; this temperature and surface gravity range covers stars of spectral class K to O. Solar metallicity models were used as the work presented in Chapter 2 showed that the helium abundance in the ejecta of the 2010 outburst was close to the solar value. Additionally, the other available grids were produced using metallicities of 10 times the solar value and 0.1 times the solar value, and since there is no reason to assume that the metallicity in U Sco is that far from the solar value these grids were not used, although this is an area that could be investigated in the future. Although atmospheres produced by Kurucz (1979) have been available for over 30 years, their application to novae has been limited, and their application to recurrent novae practically non-existent. Some work was done using model atmospheres in the 1980s on dwarf novae (Hassall 1985), novae (Andrade & Friedjung 1989), and nova-like variables (Wade 1987), however the model atmospheres have become more sophisticated since then and are yet to be applied to recurrent novae. By using these model atmospheres to model the quiescent spectrum of U Sco, investigating the companion star and mass accretion rate, these model atmospheres are being used in a new and innovative way. Spectral types of companion stars in recurrent nova systems have typically been estimated using colours (Schaefer & Ringwald 1995) or absorption lines (Hanes 1985; Anupama & Dewangan 2000). This method of using model atmospheres allows the spectral type of the companion to be estimated without relying on photometry or high resolution, high signal-to-noise spectroscopy. Using a combination of these methods, or preferably all three, should be the aim for future studies in order to produce the most reliable result. Although Kurucz atmospheres were designed to be model stellar atmospheres, they have often been used to model accretion discs (Wade 1987; Suleimanov et al. 1999), since model stellar atmospheres represent accretion disc annuli well as long as the disc is optically thick and the scale height of the atmosphere is small relative to the thickness of the disc (Mayo et al. 1980; Bath & Pringle 1981). Additionally, the temperature range of the grid of atmospheres is sufficient to incorporate both the cooler, outer regions and the hotter, inner regions of an accretion disc.

In order to fit the spectra with the model atmospheres they must be resampled onto the same wavelength scale such that the resolutions are identical. In order to do this, as well as reduce the computational time required, both the spectra and the models are binned into 400Å bins at wavelengths $\leq 1\mu m$ and bins of 1000Å at wavelengths $\geq 1\mu m$; bins of this size are necessary due to the resolution of the models. Having larger bins at longer wavelengths is not only necessary but also preferable; having a large number of small bins at longer wavelengths would result in the parameters of the fit being dominated by the red tail of the emission, however the part of the spectrum which is most temperature sensitive, and therefore is the most important when constraining a fit, is the short wavelength region and in particular the Balmer jump. However, bins this large are not ideal, as the resolution of the data is lost and rapid changes in the flux of the continuum, as occurs near the Balmer jump, become difficult to detect and therefore fit. Deciding at what point to bin the spectra into bins of 1000Å rather than 400Å was somewhat arbitrary, however in order to keep the bins as small as possible relative to the wavelength of that bin 1000Å bins were only used when $\lambda \geq 1\mu m$. Each spectrum has the emission lines cut out, since only the continuum is being modelled, and then the mean of all data points within each bin is taken as the value for that bin. Each spectrum has emission and absorption lines cut out using the snip command in DIPSO and is then read into a fitting program written by the author of this thesis. This program bins the observation, and then calculates the radial dependence of the effective temperature of the disc using Equation 3.7, assuming that the disc consists of five annuli and has a radius of 680R$_{WD}$. This radius is calculated assuming the primary has a mass of 1.4M$_\odot$, the companion has a mass of 0.88M$_\odot$, and that the radius of the disc is 0.87R$_1$ where R$_1$ is the volume radius of the primary (Thoroughgood et al. 2001). The model atmosphere with the temperature closest to the mean effective temperature of each annulus is then read in and binned; these models are scaled according to the surface area of the annulus and are then combined to form the model for the accretion disc. The companion is represented by a single model atmosphere and is allowed to vary via a free scaling parameter which allows the relative contributions of the disc and the companion to vary. The two models are then added together and scaled to the observation using a χ^2 fitting routine. The χ^2 routine is defined in equations 3.9 - 3.16 following the prescription of Press et al. (1992), where x_i is the value of the model at point i, y_i is the data value at point i, σ_i is the error in y_i, and a and b are the offset and scaling factor respectively. The standard deviation of each point within a bin is determined and is taken to be the error on the flux value for that bin.

$$\chi^2(a,b) = \sum_{i=1}^{N}(\frac{y_i - a - bx_i}{\sigma_i})^2 \tag{3.9}$$

$$a = \frac{S_y - S_x b}{S} \tag{3.10}$$

$$b = \frac{1}{S_{tt}} \sum_{i=1}^{N} \frac{t_i y_i}{\sigma_i} \tag{3.11}$$

$$S_{tt} = \sum_{i=1}^{N} t_i^2 \tag{3.12}$$

$$t_i = \frac{1}{\sigma_i}(x_i - \frac{S_x}{S}) \tag{3.13}$$

$$S = \sum_{i=1}^{N} \frac{1}{\sigma^2} \tag{3.14}$$

$$S_x = \sum_{i=1}^{N} \frac{x_i}{\sigma^2} \tag{3.15}$$

$$S_y = \sum_{i=1}^{N} \frac{y_i}{\sigma^2} \tag{3.16}$$

The χ^2 minimisation technique, which is a measure of the goodness of fit, is used here in order to find the closest fit to the spectra. At each data point the objective is to minimise

$$\frac{y - a - bx}{\sigma}^2, \tag{3.17}$$

using the same notation as described above, with the sum of this value at each data point giving the value of χ^2, as shown in Equation 3.9. Essentially, this technique is calculating the value of the difference between the flux of the model at any given wavelength and the flux of the observation multiplied by a scaling factor, b. The combination of models which gives the lowest result when this value is summed for all data points is considered to be the best fit. The boundary condition that $a \geq 0$ is imposed in order to avoid negative fluxes, which are unphysical. This particular technique was used as the number of data points is small ($\sim$15) and the calculation is relatively simple, which reduces the computing time, which matters since there is a large number of combinations of model atmospheres. Additionally, this technique is well known by astronomers and has been used in many studies to fit a range of astronomical datasets (Savoury et al. 2011; Sharp et al. 2004; Horne et al. 1994).

The fitting routine works by looping through mass accretion rates and calculating each possible combination of model atmospheres, combining them, and calculating the χ^2 parameters for each case. The b parameter is the amount by which the model is multiplied to scale it to the data and the a parameter is an offset that is then added to the model to fit it to the data. However, in each case a was found to be very small, $\leq$1% of the continuum flux, and also negative which violates the boundary condition that $a \geq 0$, therefore a=0 is adopted for each fit. The lowest χ^2 fit is then used to determine the mass accretion rate and the temperature of the companion. The errors on these values are determined by subtracting the highest and lowest fits within a 95% confidence interval, which includes models with $\chi^2 - \chi^2_{min} \leq 1$, from the best fit value. The best fits to the mass accretion rate and the effective temperature of the companion can be seen in Table 3.5. The best fit to the spectrum at phase 0.43 can be seen in Figure 3.21.

Although the χ^2 fitting routine used in this work is considered sufficiently rigorous, here potential changes and improvements to the fitting are discussed. The number of data points used in the fitting is limited by the resolution of the model atmospheres. If and when higher resolution synthetic spectra become available the size of the bins into which the observations are binned will decrease, resulting in a more robust result. Since the model atmospheres go well into the infrared taking observations with very wide wavelength coverage would also aid the fitting process. Another option to try and produce a better result is to use a different type of statistics to fit the data, such as in the form of a Bayesian analysis.

3.3.4 The companion star

Due to a lack of observations in quiescence the spectral type of the companion is poorly constrained. Spectra in quiescence give two good indicators of spectral class: absorption features and fitting the spectrum to determine the effective temperature. The Ca II H and K lines can be seen in Fig 3.11 at 3933.6Å and 3968.5Å, with the latter being blended with a hydrogen lines at 3970Å. At phase 0.62, where the H

Phase	$\dot{M}(M_\odot/yr)$	T$_{companion}$	$\log g$	b	L$_{disc}$/L$_{companion}$
0.25	$7.31^{+0.48}_{-0.64} \times 10^{-9}$	5000^{+750}_{-250}	0.0	8.88×10^{-25}	5.80
0.40	$6.52^{+0.48}_{-0.48} \times 10^{-9}$	6500^{+250}_{-250}	5.0	8.33×10^{-25}	1.90
0.43	$7.31^{+1.12}_{-0.48} \times 10^{-9}$	7000^{+250}_{-750}	5.0	7.07×10^{-25}	1.69
0.46	$7.31^{+0.48}_{-0.48} \times 10^{-9}$	6500^{+250}_{-250}	5.0	7.55×10^{-25}	2.19
0.62	$4.45^{+0.16}_{-0.32} \times 10^{-9}$	6000^{+250}_{-250}	5.0	1.28×10^{-24}	1.62

Table 3.5: Best fits for mass accretion rates and companion temperature. Errors are the 95% confidence interval.

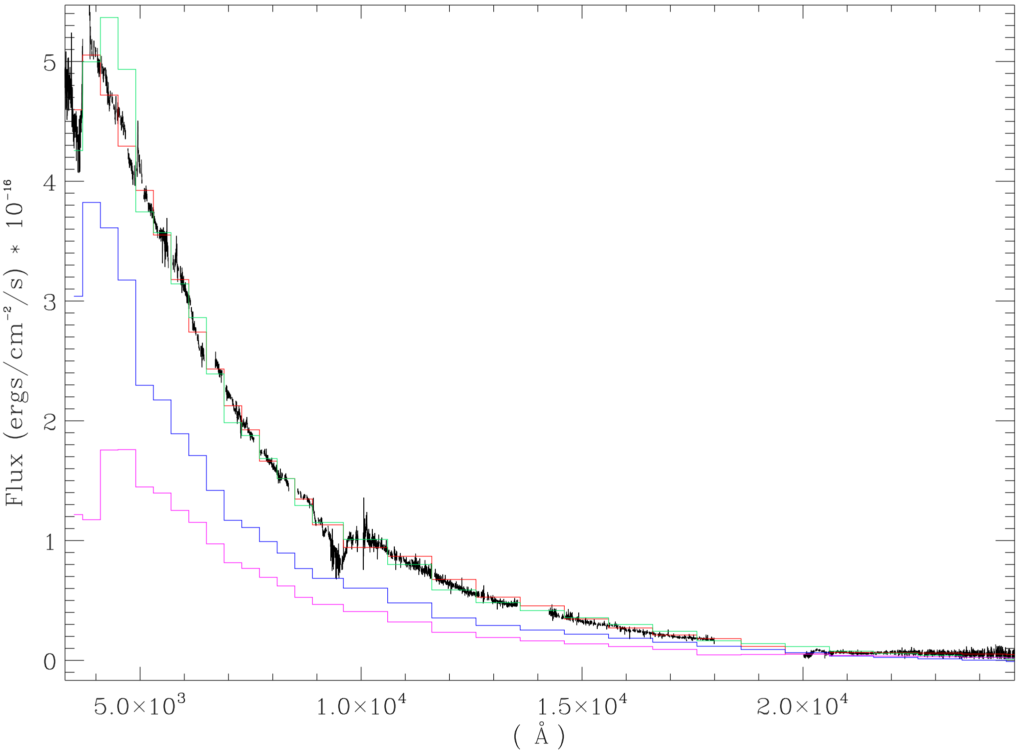

Figure 3.21: Best fit model (green) to the binned spectrum (red) at phase 0.43. The contribution of the accretion disc can be seen in blue and the contribution of the companion in purple Full fit parameters are included in Table 3.5.

absorption is weak as can be seen in Figs 3.4-3.6, the Ca line at 3968.5Å is likely the main contributor to absorption in that region. The Mg I triplet at ∼5170Å is clearly present in the VLT data at phases 0.40-0.62, with the G band at ∼4300Å possibly present, particularly at phase 0.62. Na I absorption is clearly present at ∼5900Å at all phases in SALT and VLT data. Ca II absorption could also be present at ∼8500-8800Å. However, any lines which might be present are blended with the Paschen series of hydrogen. These lines can be seen in Fig 3.15; in each blend the Ca line has a slightly shorter wavelength than the H line, and so a blue shoulder should be present on H lines which are in fact blended with Ca II. At phase 0.62, where the hydrogen line absorption is weakest, the Ca II features are most clearly seen. A spectral atlas can be used to compare the features observed in these spectra with those of stars with a well constrained spectral type. Several such libraries exist, such as those of Jacoby et al. (1984) and Montes et al. (1999). Here the atlas of Sánchez-Blázquez et al. (2006) is used, as this atlas has both the wavelength coverage and spectral type coverage necessary; spectral types F to G are shown in Fig 3.22.

3.4 Discussion

These results, including the spectral type of the companion, the mass accretion rate in quiescence, the velocities derived from spectral features, and the strength of the He II 4686Å line reveal a lot about the nature of U Sco in quiescence; here these results are discussed in the context of previous studies of U Sco and similar objects.

The best fits to the VLT spectra are shown in Table 3.5, where the mass accretion can be seen to be in the range 4.45-7.31$\times10^{-9}\,\mathrm{M}_\odot\,\mathrm{yr}^{-1}$ with the temperature of the companion being in the range 5000 - 7000 K. Given that ejected mass estimates for the previous outbursts are $\sim 10^{-6} - 10^{-7}\,\mathrm{M}_\odot$ (Diaz et al. 2010; Schaefer 2011) and a mean recurrence time of ∼10 years, it appears that U Sco is losing mass over time. However this may not be the case. The VLT data, taken ∼18 months after

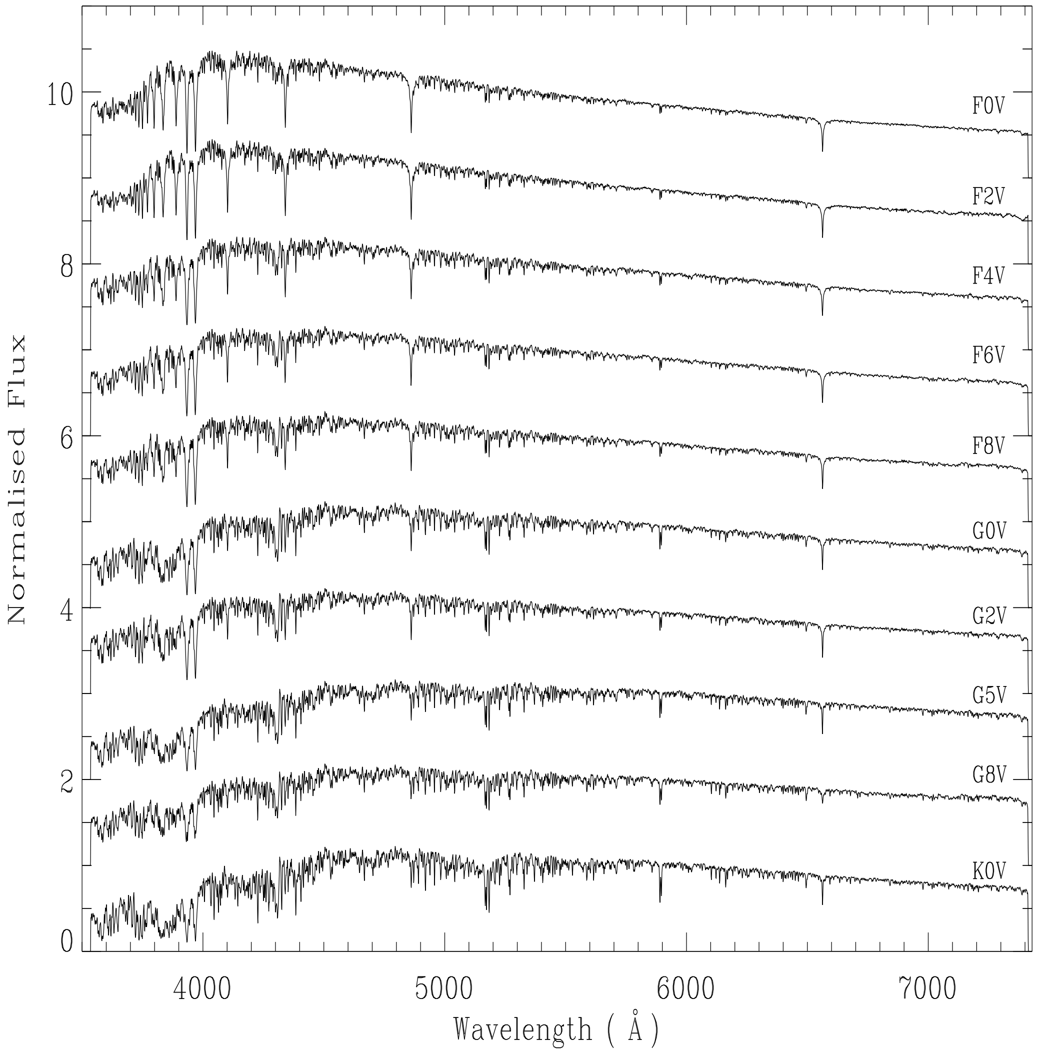

Figure 3.22: Spectra of stars of known spectral type from the MILES library (Sánchez-Blázquez et al. 2006)

outburst, show a clear rise in the continuum at shorter wavelengths to which a model can be fitted giving a mass accretion rate. In the SALT data, taken ∼30 months after outburst, the peak of the continuum is not present as it has moved to shorter wavelengths by this time. It is therefore difficult to make meaningful conclusions from modelling these data since only the red tail of the accretion disc emission is present in the observed wavelength range.

This change in the behaviour of the continuum can be explained by an increase in the luminosity of the accretion disc. As the disc, which is destroyed in the outburst (Mason et al. 2012; Ness et al. 2012), becomes fully re-established the luminosity of the disc increases. Schaefer et al. (2011) find that the disc has become fully re-established by 67 days after outburst. However this result is inconsistent with the VLT and SALT spectra, which suggest that the disc takes at least ∼18 months to become fully re-established.

If the disc were in the steady state by the time of the VLT and SALT observations, then an increase in the luminosity of the disc would imply that the mass accretion rate (see Equation 10 of Selvelli et al. 2008) and therefore the temperature (Equations 3.7 and 3.8) have increased, causing the peak of the emission to move well into the UV and the contribution in the optical to become much less significant. However, the differences between the VLT and the SALT spectra, and the low mass accretion rates (relative to the rates derived from the He II 4686Å line) derived from the fits to the VLT data, show that the disc is not in the steady state ∼18 months after outburst and is still evolving. The increase in luminosity is likely due to an increase in the amount of material in the disc and an increase in the contribution of the inner, hotter regions of the disc, causing the mean effective temperature to increase. Simulations of disc formation in dwarf novae (Ichikawa & Osaki 1992) and X-ray binaries (Hayasaki & Okazaki 2004) have shown that accretion discs in these systems shrink over time, although it is not clear if this is the case in recurrent novae. If the disc is shrinking over time then the inner, hotter regions of the disc will become more significant at later times, causing the mean effective temperature of the disc and therefore the mass accretion rate to increase once the steady state has been reached.

This interpretation can be tested through further observations. If optical spectra at different times and phases show no evidence of a rise in the continuum at shorter wavelengths then the disc is indeed too hot to provide a significant contribution. However, if there is a significant rise, then the continuum can be modelled to provide an estimate of the temperature, luminosity and mass accretion rate. UV spectra would be invaluable in determining the nature of the accretion disc in this system if optical spectra cannot be modelled.

As with the blackbody modelling, there is the concern that when fitting the Rayleigh-Jeans tail it is difficult to constrain an upper limit for the temperature, although the presence of the Balmer jump in both the observations and the model atmospheres helps to constrain the blue end of the spectrum making this less of an issue. Variations in the measured temperature of the companion are expected due to irradiation from the hot component causing the effective temperature of the companion to appear different depending on orbital phase; this may explain the lower effective temperature of the companion at phase 0.25 as can be seen in Table 3.6.

Mass accretion rates derived from the luminosity of the He II 4686Å lines are shown in Table 3.3 and are higher than those derived from the fits to the VLT data at $\sim 10^{-7}\,\mathrm{M}_{\odot}\,\mathrm{yr}^{1}$. The rates from this method are lower limits due to the optically thick nature of the 4686Å line, and are consistent with U Sco ejecting $\sim 10^{-6} - 10^{-7}\,\mathrm{M}_{\odot}$ every ∼10 years. The mass accretion rates from the fits to the VLT data were derived assuming that the disc is in the steady state; such a large discrepancy between these two sets of mass accretion rates is consistent with the disc not being in the steady state ∼18 months after outburst.

The strength of He II 4686Å compared to the Balmer lines in the VLT spectra, combined with the disagreement with case B recombination and the velocity of the material, suggests that the He II 4686Å emission is not co-extensive with the H emission. The He II 4686Å emission feature is consistent (Patterson & Raymond 1985) with emission from the centre of the disc where it is experiencing soft X-ray irradiation from the boundary layer; the formation of He II lines requires a temperature of $\geq 10^{4.5}$ K. The H emission can be formed in the cooler outer regions of the disc; hydrogen becomes ionised at $\sim 10^4$ K (Mihalas et al. 1990). The strong He II emission has previously been used to suggest that the companion may be He-rich (Hachisu et al. 1999), but this analysis demonstrates that the observed line strengths are expected for a high mass white dwarf accreting at a high rate (see Figure 5 of Patterson & Raymond 1985).

The SALT spectra, which were taken ∼2.5 years after the 2010 outburst (Fig 3.3), can be used with Fig 3.22 to estimate the spectral class of the companion by looking at the behaviour of the continuum. The SALT spectra show different behaviour, with the continuum at phase 0.55 being almost flat, whereas at phase 0.77 there is a clear decline in the continuum level from shorter wavelengths to longer. At phase 0.55 the companion is behind the accretion disc and so will be partially obscured but should be fully visible at phase 0.77, and so less of the emission from the companion is being absorbed at this phase. A long term photometric and spectroscopic study is required in order to determine if the brightness variability and the shape of the continuum are independent.

Which face of the companion is being observed must also be considered, as the companion is irradiated by the hot component. The inwards facing hemisphere of the companion will experience this irradiation which should make it hotter than the outwards facing hemisphere. The flat continuum of phase 0.55 appears to be most similar to the cooler G type stars (Figure 3.22), whereas at phase 0.77, where the continuum is not flat and the companion is more visible, the cooler F type stars appear most similar. The VLT spectra show a significant continuum slope in the optical as well as many emission lines, which may indicate that the system has not fully returned to quiescence (c.f. the spectra of Johnston & Kulkarni 1992) by the time of these observations (∼ 18 months after outburst), and that at this time the disc is still cool enough to be causing a significant contribution in the optical.

The best fits to the VLT spectra show that the effective temperature of the companion is in the range 5000-7000K, corresponding to a spectral type of K0 - F3, expanding to K2 - F2 at the 95% confidence level as shown in Table 3.6. The luminosity of the companion can also be derived from these fits as shown in Table 3.6 for a distance of 12 kpc, which then allows the radius, R, of the companion to be estimated using

$$R \simeq \frac{\sqrt{L}}{T^2}, \tag{3.18}$$

where T is the temperature and L is the luminosity, all in solar units. The luminosity and radius of the companion are found to be in the range 1.41-4.32 $L_\odot$ and 1.43-1.91 $R_\odot$ respectively, lower than the determination of $2.1 \pm 0.2\,R_\odot$ by Thoroughgood et al. (2001), although both results suggest that the companion is a subgiant star. Given that the volume radius of the companion is 1.61 $R_\odot$, assuming the mass of the companion is 0.88 $M_\odot$ (Thoroughgood et al. 2001), the companion is likely filling this volume as required for RLO accretion.

Absorption lines such as Ca II, the G band, Mg I, and Na I are also useful diagnostics for determining spectral class. These features are displayed in Figs 3.11-3.14 and can be compared to the same features in the spectra of Sánchez-Blázquez et al. (2006) in Figs 3.23-3.26. The G band, Mg I, and Na I absorption features all become stronger as the spectral type varies from F0 to K0, with the Ca II features becoming

Phase	$T_{companion}$ (K)	$L/L_\odot$	$R/R_\odot$	Spectral class	Spectral class at 95% confidence interval
0.25	5000^{+750}_{-250}	$1.41^{+1.06}_{-0.24}$	$1.60^{+0.77}_{-0.21}$	K0	G3 - K2
0.40	6500^{+250}_{-250}	$3.76^{+0.67}_{-0.51}$	$1.54^{+0.18}_{-0.16}$	F7	F5 - F9
0.43	7000^{+250}_{-750}	$4.32^{+0.71}_{-1.56}$	$1.43^{+0.40}_{-0.40}$	F3	F2 - F9
0.46	6500^{+250}_{-250}	$3.41^{+0.60}_{-0.47}$	$1.47^{+0.17}_{-0.15}$	F7	F5 - F9
0.62	6000^{+250}_{-250}	$4.19^{+0.79}_{-0.62}$	$1.91^{+0.24}_{-0.21}$	G0	F9 - G3

Table 3.6: Spectral type from fits to VLT data.

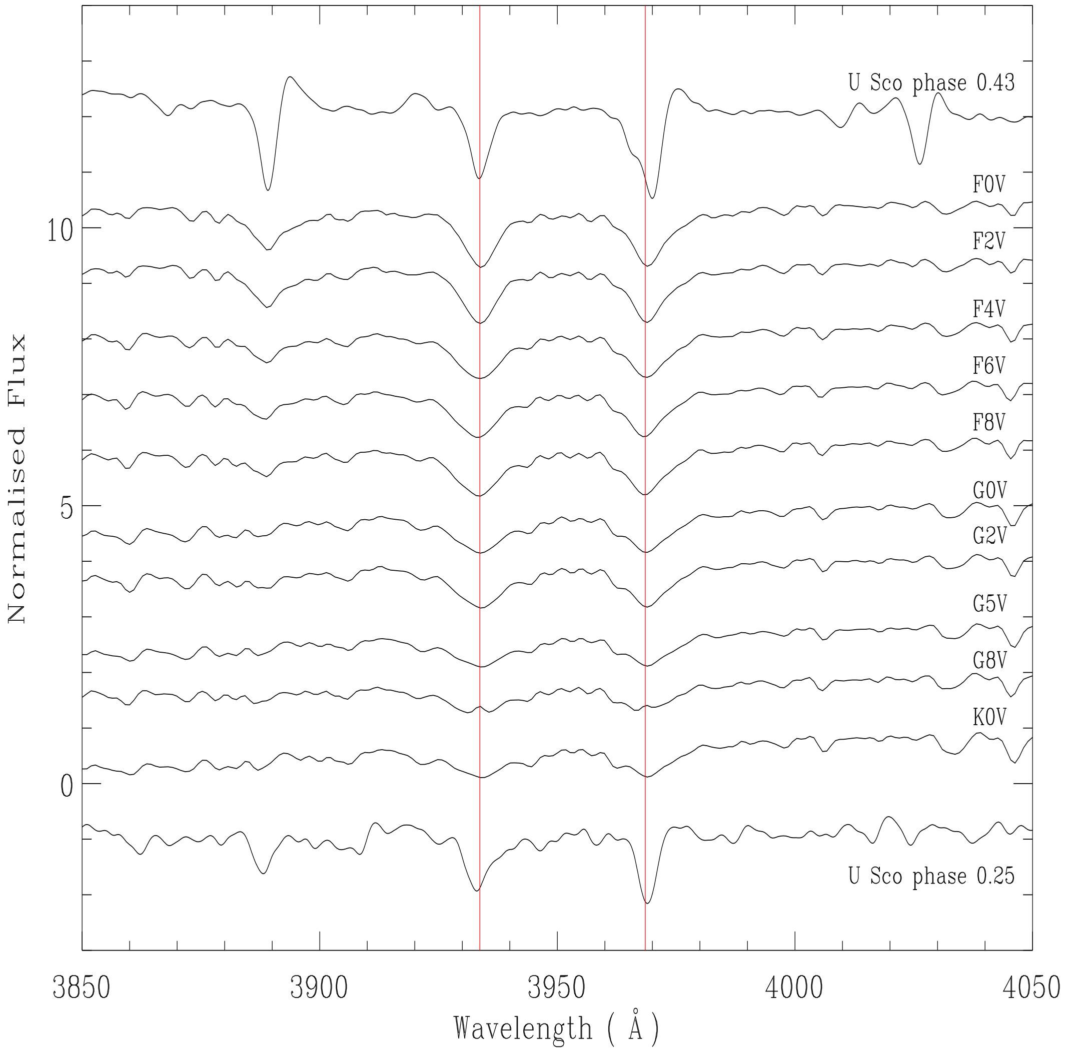

Figure 3.23: Ca II H and K lines from Sánchez-Blázquez et al. (2006). U Sco spectra with the hottest (top) and coolest (bottom) companion effective temperature fits also shown. The rest wavelength of the H and K lines are shown in red.

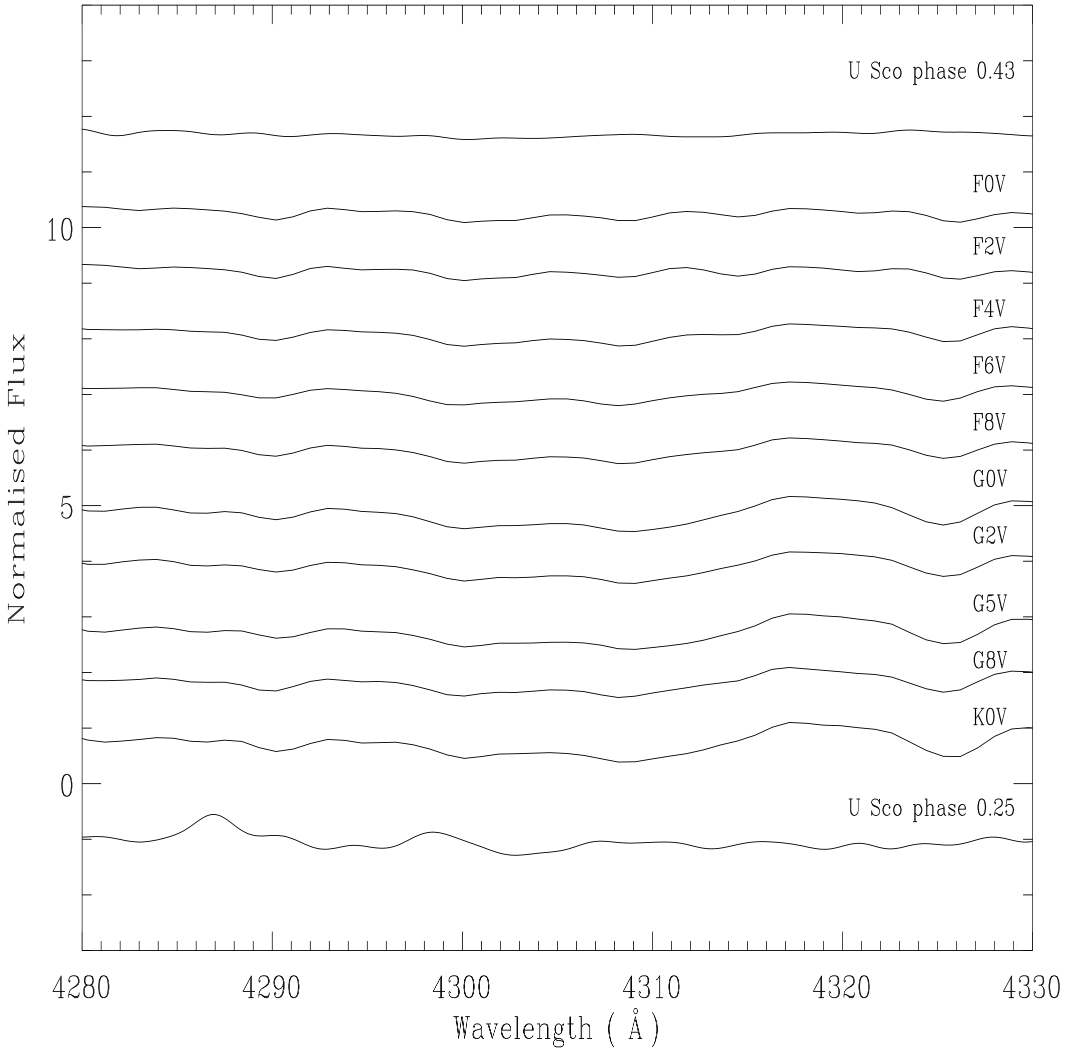

Figure 3.24: G band (CH) lines from Sánchez-Blázquez et al. (2006). U Sco spectra with the hottest (top) and coolest (bottom) companion effective temperature fits also shown.

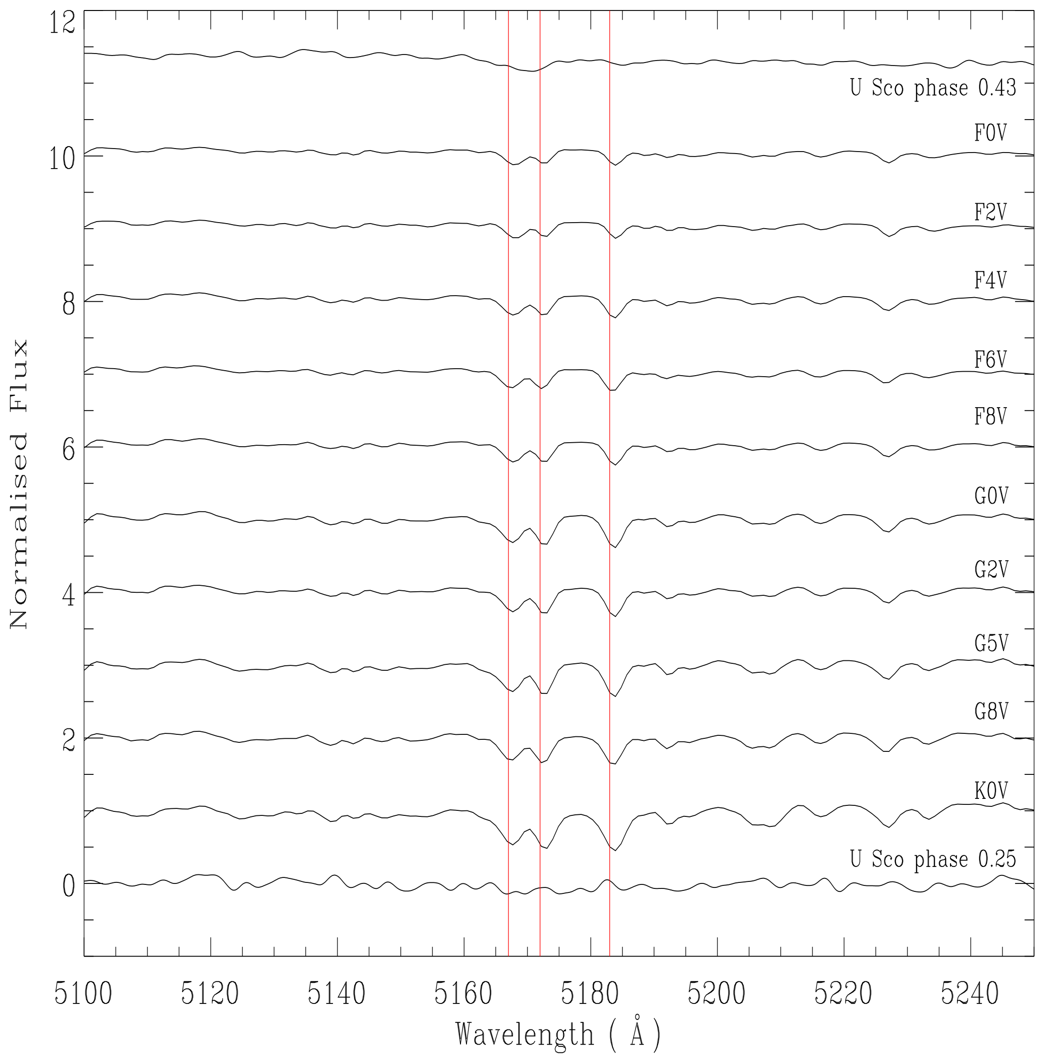

Figure 3.25: Mg I triplet lines from Sánchez-Blázquez et al. (2006). U Sco spectra with the hottest (top) and coolest (bottom) companion effective temperature fits also shown. The rest wavelength of each line of the triplet are shown in red.

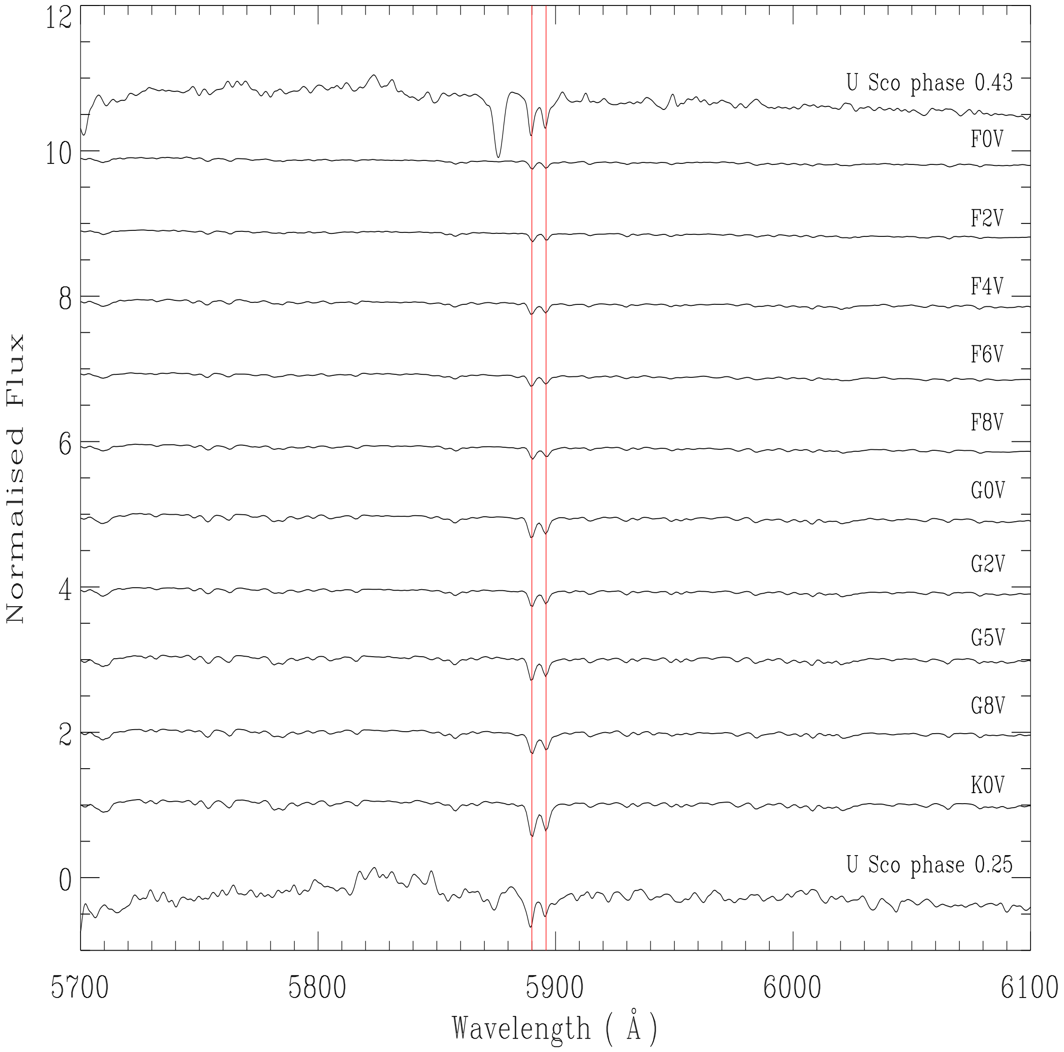

Figure 3.26: Na I band lines from Sánchez-Blázquez et al. (2006). U Sco spectra with the hottest (top) and coolest (bottom) companion effective temperature fits also shown. The rest wavelength of each line is shown in red.

weaker. From the weakness of the G band, Mg I, and Na I absorption features, and the strength of the Ca II features, an F type star seems to give the best fit to the observed spectra. The Ca II H+K lines, as well as the lines at ~8500Å have been shown to be present, which indicates that a hot G or F star would be a reasonable fit. The independent estimates of the spectral type of the secondary discussed here are most consistent with the estimates of Johnston & Kulkarni (1992) and Hanes (1985), who derive spectral types of F8 ± 2 and G0 ± 5 respectively. From Figs 3.11-3.14 there is a clear variation in the strength of the absorption features with phase; the irradiation of the companion and the orbital phase of the observation may well be important factors in determining the spectral class of the companion, although the variability of the disc must also be considered. Observations of the companion at phase 0.0, when the coolest hemisphere of the companion is observable and the accretion disc is the most obscured, would be invaluable in determining the nature of the companion.

3.5 Conclusion

Optical and NIR spectra of U Sco have been obtained with better resolution, temporal coverage, and wavelength coverage in quiescence than ever before, allowing many outstanding questions regarding the system in quiescence to be addressed. The companion has been shown through fits to VLT spectra to have an effective temperature in the range 5000 - 7000 K depending on the orbital phase, with four of the five spectra being consistent with a spectral type of F2-G3 at the 95% confidence level. From the lines present in the spectra and their relative strength, and through comparison with a library of stars of known spectral type, the companion in U Sco has been shown to be consistent with either an F or hot G type star. The luminosity and radius of the companion suggest it is a subgiant star; the luminosity and radius are 1.41-4.32 $L_\odot$ and 1.43-1.91 $R_\odot$ respectively, as determined from the effective temperature of the fits to the VLT spectra. In both the VLT and SALT spectra He II 4686Å is the strongest feature, consistent with the emission coming from the central regions of the disc arising from irradiation from the boundary layer, whereas the H lines originate in the outer, cooler regions of the disc. The Balmer lines and other He II lines ratios have been shown to be consistent with the ratios expected from case B recombination. However, ratios derived from the He II 4686Å line flux are not. Finally, the velocity of the He II 4686Å line does not decrease significantly at later times whereas the velocity of the other lines do.

From fits to the VLT data it has been shown that the accretion disc has not become fully re-established by the time of these observations. The level of activity in the VLT spectra obtained ∼18 months after outburst compared to the SALT spectra taken ∼30 months after outburst, as well as the clear change in slope of the continuum in the VLT spectra, indicates that the system returns to photometric quiescence (meaning the V band magnitude has returned to the pre-outburst level) before it returns to spectroscopic quiescence (where spectral features due to the ejecta have disappeared and the spectrum resembles the pre-outburst spectrum). The differences between the two datasets indicates that the accretion disc takes at least ∼18 months to become fully re-established. The VLT data show a strong rise in the continuum at shorter wavelengths, caused by the accretion disc which is still re-establishing itself at this time. The SALT data display a flatter continuum, indicating that the luminosity of the disc has increased to the point that the contribution in the optical is not significant. In order to follow the return to spectroscopic quiescence, in both U Sco and in other systems, it will be necessary to continue observational campaigns for many months after outburst. Further observations of U Sco in quiescence, particularly if covering a long time base and several different orbital phases, will allow the effects of orbital phase and long term variations to be better separated and understood. UV observations in particular would help to further constrain the mass accretion rate in quiescence and the nature of the accretion disc.

Chapter 4

Other recurrents

4.1 RS Ophiuchi

4.1.1 Introduction

As discussed in Chapter 1 the 2006 outburst of RS Oph was well observed in the optical, radio, X-ray, and IR, but ultra-violet (UV) observations were few and far between. The International Ultra-violet Explorer (IUE) had taken extensive observations of the 1985 outburst (Shore et al. 1996; Cassatella et al. 1985), but since the demise of IUE in 1996 there has been a distinct lack of UV observations of novae. The UV contains many spectral lines useful in analyses of novae both during outburst and in quiescence (Shore 2008), including several species of Mg, N, Fe, C, and He. In particular lines such as Mg II, O III, He II and high ionisation state Fe lines are often used in analyses of nova outbursts and are observable by UVOT. Some of these important lines are labelled in the UVOT spectra shown in Fig 4.4. These lines are particularly useful in the case of recurrent novae as they can be used to determine abundances, temperatures, and densities in nova ejecta and for studying the white dwarf and accretion disc in quiescence. Therefore, any UV observations would provide another dimension to the study of a nova outburst, such as that of

RS Oph in 2006.

4.1.2 Swift/UVOT observations

Data reduction

Following the 2006 outburst Swift (Gehrels et al. 2004b), a space based telescope, began observing RS Oph ~30 days after the optical maximum; before this time the object was thought to be too bright; RS Oph was one of the first bright objects to be observed and the magnitude limits were uncertain. Swift is equipped with UVOT (Ultra-Violet and Optical Telescope, Roming et al. 2005), one of only a few facilities with UV capabilities and a long term successor to the IUE. Following the outburst 56 spectra were obtained throughout 2006, with 18 further spectra being taken over the next four years. These observations are available through the Swift archive and are summarised in Table 4.1.[1] U grism observations cover 1670 - 5886Å, V grism observations 2668 - 6117Å. Although RS Oph was observed by Swift for several years after outburst, problems with the calibration of the grism detectors have prevented results from these data from being published, presented, or otherwise made available to date. This work therefore represents one of the first attempts to reduce these data and derive reliable results using the current reduction tools. Problems with the calibration include (Paul Kuin, private communication):

- The wavelength calibration is not constant across the detector;
- The calibration becomes worse as the source moves further away from the detector boresight;
- There is overlap between the different orders of the grism;
- Coincidence loss is unaccounted for;

---

[1] http://www.swift.ac.uk/archive/

- Background sources within the extraction region cannot be removed.

Table 4.1: Summary of UVOT observations.

Date	Start time	Exposure time (s)	Detector
13/3/2006	19:55:46	1338.5	U Grism
14/3/2006	16:57:09	1350.6	U Grism
15/3/2006	20:09:47	1603.3	U Grism
16/3/2006	20:15:48	1605.9	U Grism
17/3/2006	17:31:09	970.4	U Grism
24/3/2006	00:24:23	1041.0	U Grism
25/3/2006	00:18:37	523.3	U Grism
28/3/2006	00:47:41	19.1	U Grism
29/3/2006	00:46:29	799.0	U Grism
30/3/2006	00:56:38	553.4	U Grism
31/3/2006	09:00:37	559.4	U Grism
1/4/2006	07:28:37	317.2	U Grism
2/4/2006	09:11:44	664.9	U Grism
3/4/2006	07:41:37	372.2	U Grism
4/4/2006	07:47:45	419.2	U Grism
5/4/2006	00:02:39	1615.1	U Grism
6/4/2006	00:12:15	1402.7	U Grism
7/4/2006	00:23:18	1222.3	U Grism
8/4/2006	00:31:10	567.7	U Grism
11/4/2006	02:21:33	704.4	U Grism
11/4/2006	14:55:38	731.0	U Grism
12/4/2006	02:26:38	732.0	U Grism
12/4/2006	15:11:39	732.0	U Grism

Table 4.1: Summary of UVOT observations (continued).

Date	Start time	Exposure time (s)	Detector
13/4/2006	08:43:38	671.0	U Grism
15/4/2006	02:48:02	423.0	U Grism
15/4/2006	15:43:40	346.2	U Grism
16/4/2006	01:21:14	328.5	U Grism
16/4/2006	15:51:40	346.2	U Grism
16/4/2006	23:54:40	317.7	U Grism
17/4/2006	15:56:39	346.2	U Grism
18/4/2006	00:02:40	405.3	U Grism
19/4/2006	14:35:39	346.2	U Grism
20/4/2006	14:42:39	376.7	U Grism
21/4/2006	00:02:39	405.3	U Grism
22/4/2006	03:26:39	731.0	U Grism
23/4/2006	03:32:40	731.0	U Grism
24/4/2006	02:01:39	731.0	U Grism
25/4/2006	20:02:41	464.3	U Grism
26/4/2006	18:31:40	55.3	U Grism
27/4/2006	17:04:13	267.3	U Grism
28/4/2006	15:42:48	366.7	U Grism
30/4/2006	17:08:38	818.6	U Grism
2/5/2006	15:35:26	979.9	U Grism
4/5/2006	00:02:09	330.5	U Grism
19/2/2007	12:06:06	197.4	U Grism
26/2/2007	01:48:41	573.6	U Grism
4/3/2007	10:20:13	802.9	U Grism

Table 4.1: Summary of UVOT observations (continued).

Date	Start time	Exposure time (s)	Detector
11/3/2007	01:28:59	689.7	U Grism
11/5/2008	03:28:23	627.3	U Grism
11/5/2008	11:29:23	745.3	V Grism
13/5/2008	08:28:22	1100.1	U Grism
13/5/2008	11:41:22	1159.4	V Grism

A guide to data reduction with the current official reduction software, as well as in-development tools which will address many of the problems outlined above, is available at the website of Dr Paul Kuin.[2] The tools used are part of the HEASoft[3] package and the data reduction steps are outlined in Table 4.2.

The extraction of spectra with UVOTIMGRISM is not trivial. Factors such as the width of the extraction region, the width of background regions, the distance of the background regions from the extraction region, and the aspect correction must be considered, therefore the creation of a plot showing the extraction region with UVOTGRPLOT is necessary. Examining the output of UVOTGRPLOT allows the regions selected for the source and the background to be viewed and adjusted in order to account for any background sources which may be present in those regions. By trying different combinations of these parameters, finding problems with the reduction software, and discussing this process with the calibration team, the issues surrounding coincidence loss (max loss now $\leq$ 10%), wavelength calibration (max error now $\leq$ 50Å), and order overlap were significantly improved. The output from UVOTGRPLOT for three different observations taken ~1 month, ~3 months, and ~3 years after the 2006 outburst can be seen in Figs 4.1-4.3. In the observation taken

---

[2] http://www.mssl.ucl.ac.uk/~npmk/Grism/General/reduce.html

[3] http://heasarc.gsfc.nasa.gov/lheasoft/

∼1 month after outburst the effect of saturation and coincidence loss can clearly be seen at ∼700 pixels in Fig 4.1; at this time the target was still very bright (V mag ∼9). In each of Figs 4.1-4.3 the parameters defining the extraction and background regions, the exposure time, the date of observation, the roll angle, and the source position can be seen to the left of the Figure. It is evident from these figures that there are many background sources present in the field of view; in order to get a good extraction it is imperative that no bright sources are in the source extraction region whilst the number of bright sources in the background regions must be kept to a minimum. Typically the source extraction region is ∼25 pixels with the background regions being ∼30 pixels wide. The centre of the zeroth order can be seen at the left edge of each plot. The spectra shown in the middle panels of Figs 4.1-4.3 show the net counts vs wavelength. The flux calibrated spectra extracted using UVOTIMGRISM can be seen in Fig 4.4; the two spectra from 2006 clearly show that there can be significant variation in the wavelength calibration.

Flux calibration

As mentioned above, there are several factors which cause difficulties when extracting a spectrum from Swift/UVOT observations. These issues are the causes of significant sources of error in the flux calibration. The presence of background sources in the extraction region, which cannot be accounted for by the current software, cause the calibration algorithms to overestimate the flux at a given wavelength. Background sources in the background subtraction regions cause the background to be overestimated at certain points. The UVOT grism consists of several orders; whilst at shorter wavelengths the contribution of orders above the first is negligible at wavelengths greater than ∼ 4000Å their contribution becomes significant, however the current reduction process does not account for this in a comprehensive way. The most recent updates to the reduction software includes a routine for accounting

Command	Purpose
UVOTBADPIX	Identifies bad pixels via a query to the calibration database.
UVOTMODMAP	Creates a mod8 corrected image using the output of uvotbadpix and a mod8 correction file
SWIFTXFORM	Converts the raw image to detector co-ordinates using the attitude file, teldef file, the roll angle, and the co-ordinates of the target.
UVOTGRASPCORR	Performs aspect and distortion corrections using the distortion file from the calibration database and the usnob1 catalogue.
UVOTIMGRISM	Extracts a flux calibrated spectrum.
FDUMP	Writes the extracted spectrum to a text file.
UVOTGRPLOT	Creates a plot showing the image and extraction region (see Figs 4.1-4.3).

Table 4.2: Official UVOT data reduction tools, part of the HEAsoft software package (http://heasarc.gsfc.nasa.gov/lheasoft/), and their usage.

for coincidence loss in the first order, however it is still unaccounted for in other orders. The collective contribution of all these factors, combined with the usual issues surrounding flux calibration of any dataset, result in an error of ∼10% in the flux calibration (Paul Kuin, private communication).

4.1.3 Lightcurves

Darnley et al. (2008) published B, V, and r′ lightcurves, reproduced in Figure 4.5, taken at the Liverpool Telescope covering up to ∼550 days after outburst. The lightcurves show the end of the initial decline followed by a plateau phase and final

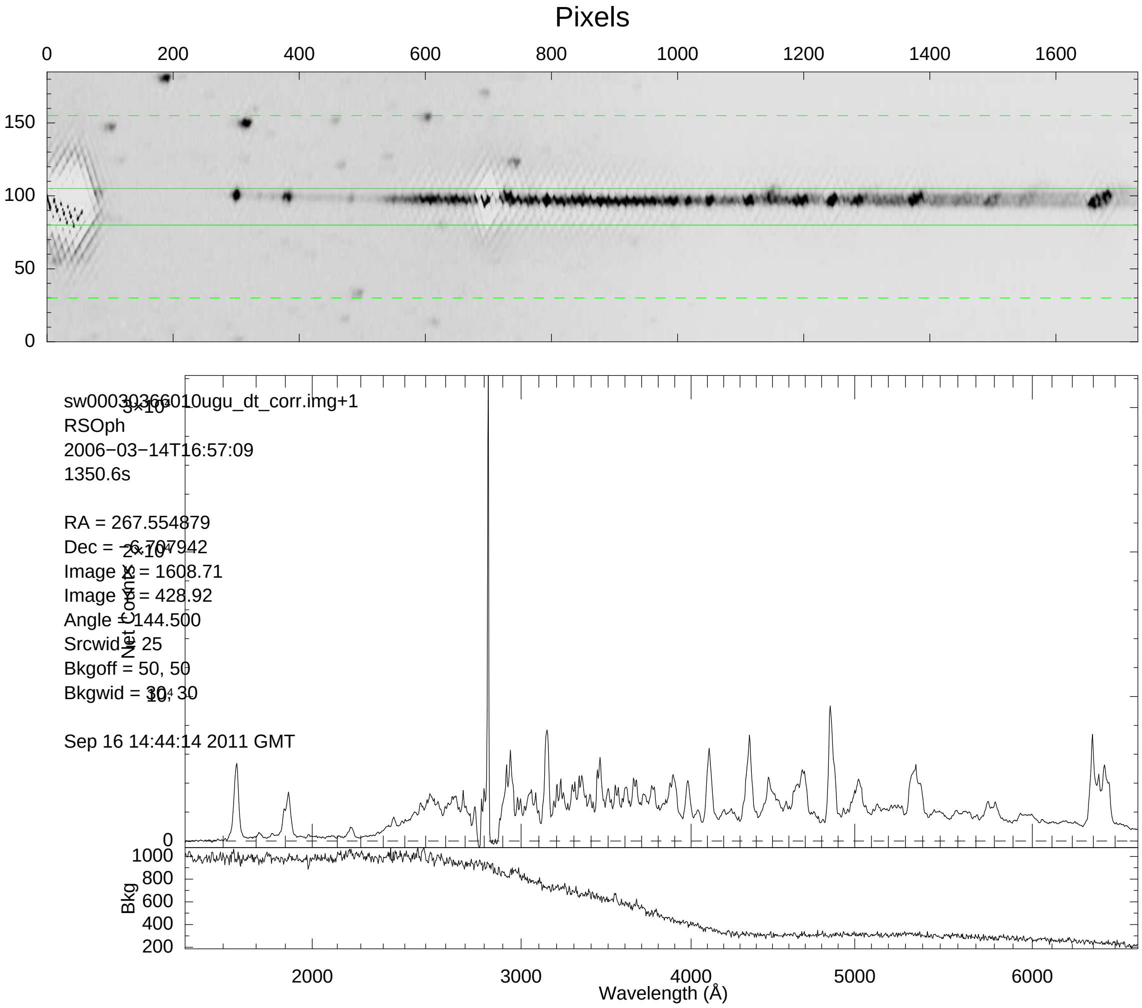

Figure 4.1: Output of UVOTGRPLOT for spectrum of RS Oph taken 14/3/2006. Note the saturation and coincidence loss at ∼700 pixels. Top panel: Detector image showing extraction region (solid green lines) and background regions (dashed lines). Middle panel: Extracted spectrum shown as counts vs wavelength. Bottom panel: Background contribution.

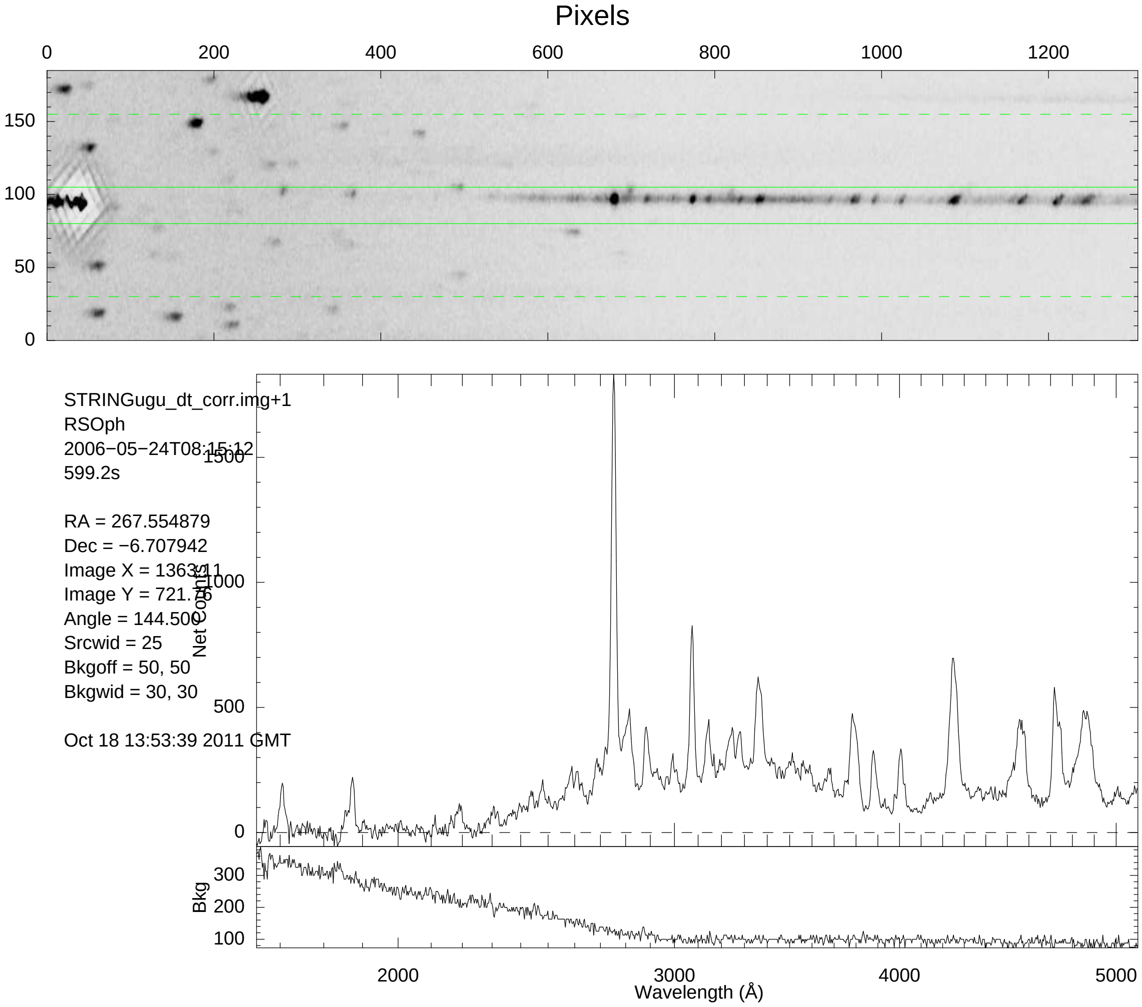

Figure 4.2: Output of UVOTGRPLOT for spectrum of RS Oph taken 24/5/2006. Top panel: Detector image showing extraction region (solid green lines) and background regions (dashed lines). Middle panel: Extracted spectrum shown as counts vs wavelength. Bottom panel: Background contribution.

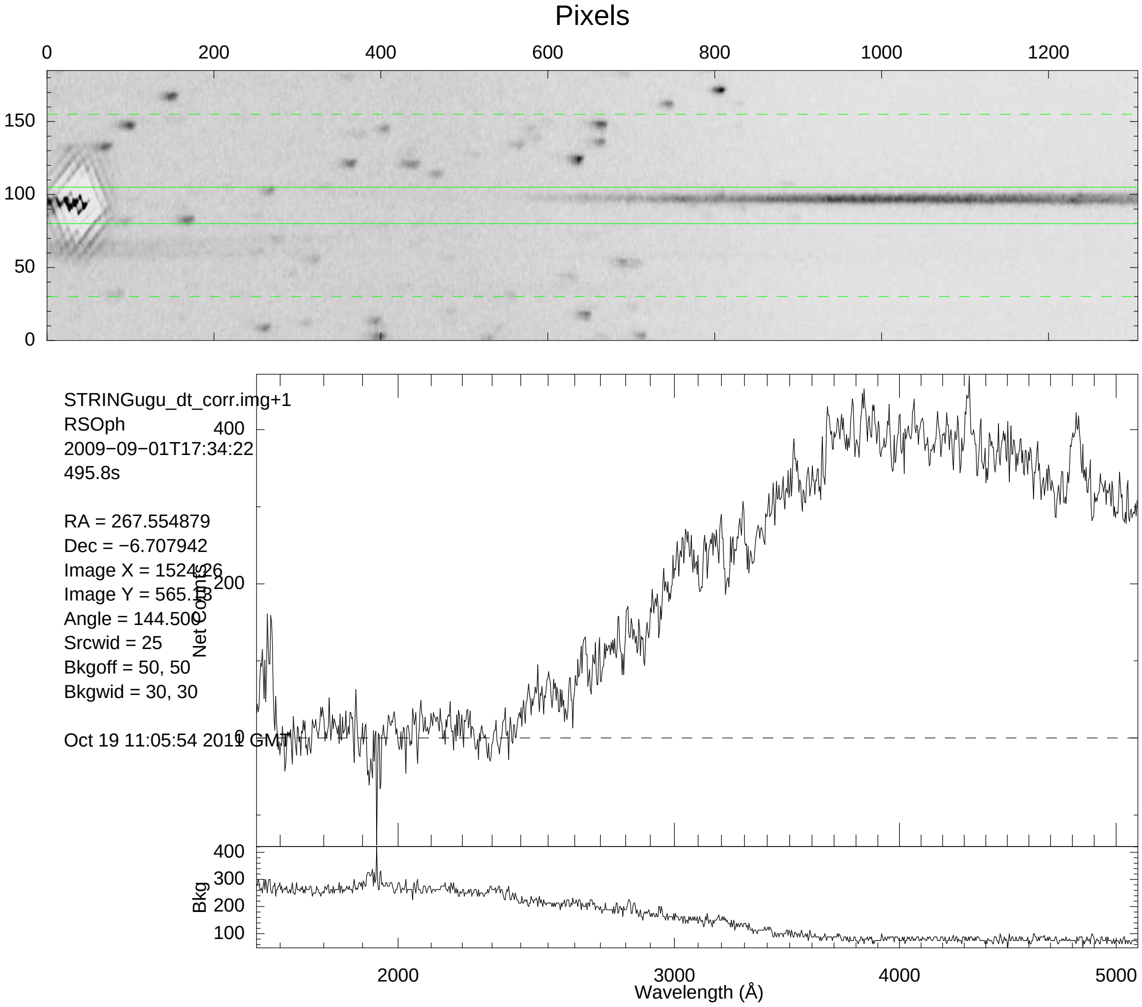

```
STRINGugu_dt_corr.img+1
RSOph
2009−09−01T17:34:22
495.8s

RA = 267.554879
Dec = −6.707942
Image X = 1524.26
Image Y = 565.18
Angle = 144.500
Srcwid = 25
Bkgoff = 50, 50
Bkgwid = 30, 30

Oct 19 11:05:54 2011 GMT
```

Figure 4.3: Output of UVOTGRPLOT for spectrum of RS Oph taken 01/9/2009. Top panel: Detector image showing extraction region (solid green lines) and background regions (dashed lines). Middle panel: Extracted spectrum shown as counts vs wavelength. Bottom panel: Background contribution.

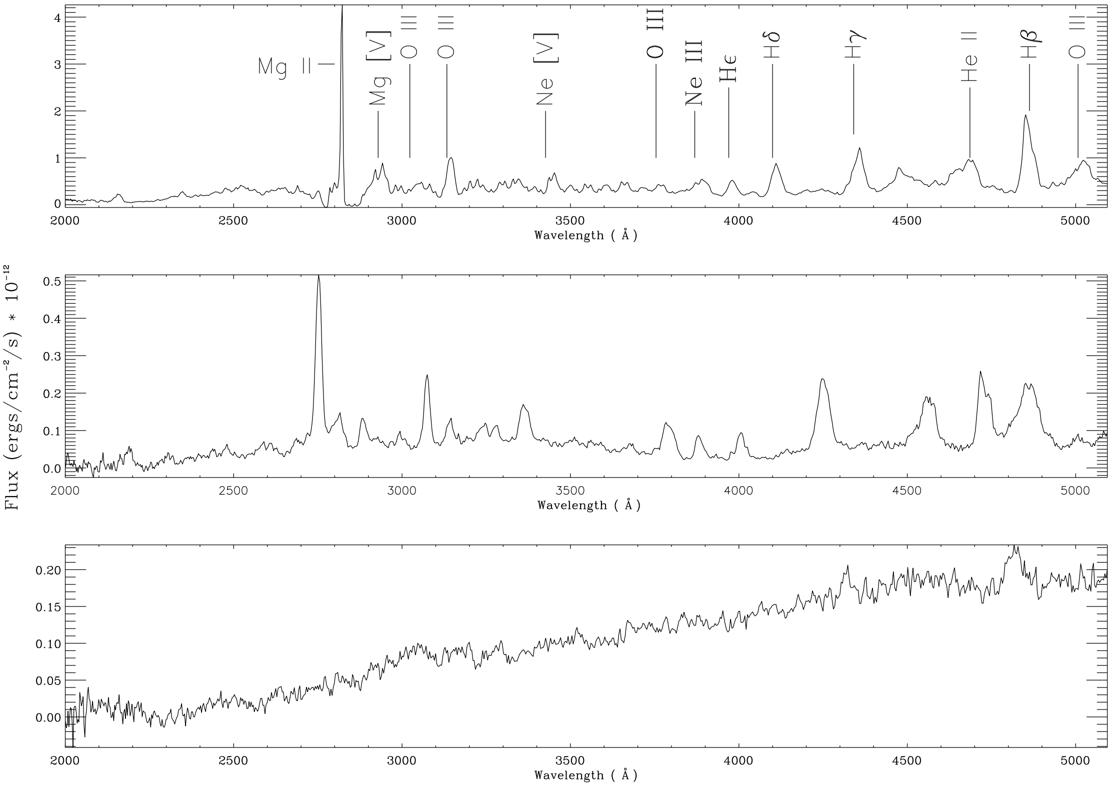

Figure 4.4: Sample spectra extracted from observations on 14/3/2006, 24/5/2006, and 01/9/2009.

decline. Adamakis et al. (2011) find that for all outbursts the mean end of the initial decline is at 53.07 days, the mean end of the plateau phase is at 106 days, and the mean time of the end of the final decline is at 142.89 days. There is a post-outburst minimum ~200 days after outburst followed by a slow rise to the pre-outburst quiescent level. The plateau phase, during which the lightcurve declines by ≤0.5 mag, lasts for ~40 days.

Using these spectra taken by UVOT following the 2006 outburst and the filter response functions of the Liverpool Telescope filters it is possible to produce B, u′, and ultra-violet lightcurves. UVOT covers the wavelength range 1651-5094Å, allowing both u′ (3150 - 3900Å) and B (3780 - 4830Å) lightcurves to be produced. UV is defined here as 1651 - 3150Å, and the lightcurve for this waveband is produced by integrating the flux in this wavelength regime. For the B and u′ lightcurves, each spectrum has the data outside of the region of interest removed and is then multiplied by the response function of the filter. The spectrum is then divided by the effective width of the filter and integrated to give the flux. The flux is then converted to a magnitude using Equation 4.1 (Pogson's equation),

$$F = F_0 \times 10^{-0.4m}, \tag{4.1}$$

where F is the flux, F_0 is the zero-point of the filter, and m is the apparent magnitude. The zero-point of the B filter is the same as the Liverpool Telescope[4] B filter with the zero-point of the u′ filter being taken from the Spanish Virtual Observatory[5]. When using data acquired with different filters there is an associated error, since the filters are not identical, however the zero-points for these particular filters are well determined therefore this error is considered to be small compared to the errors associated with the flux calibration of the UVOT data, which will dominate the uncertainties.

---

[4] http://telescope.livjm.ac.uk/

[5] http://svo.cab.inta-csic.es/main/index.php

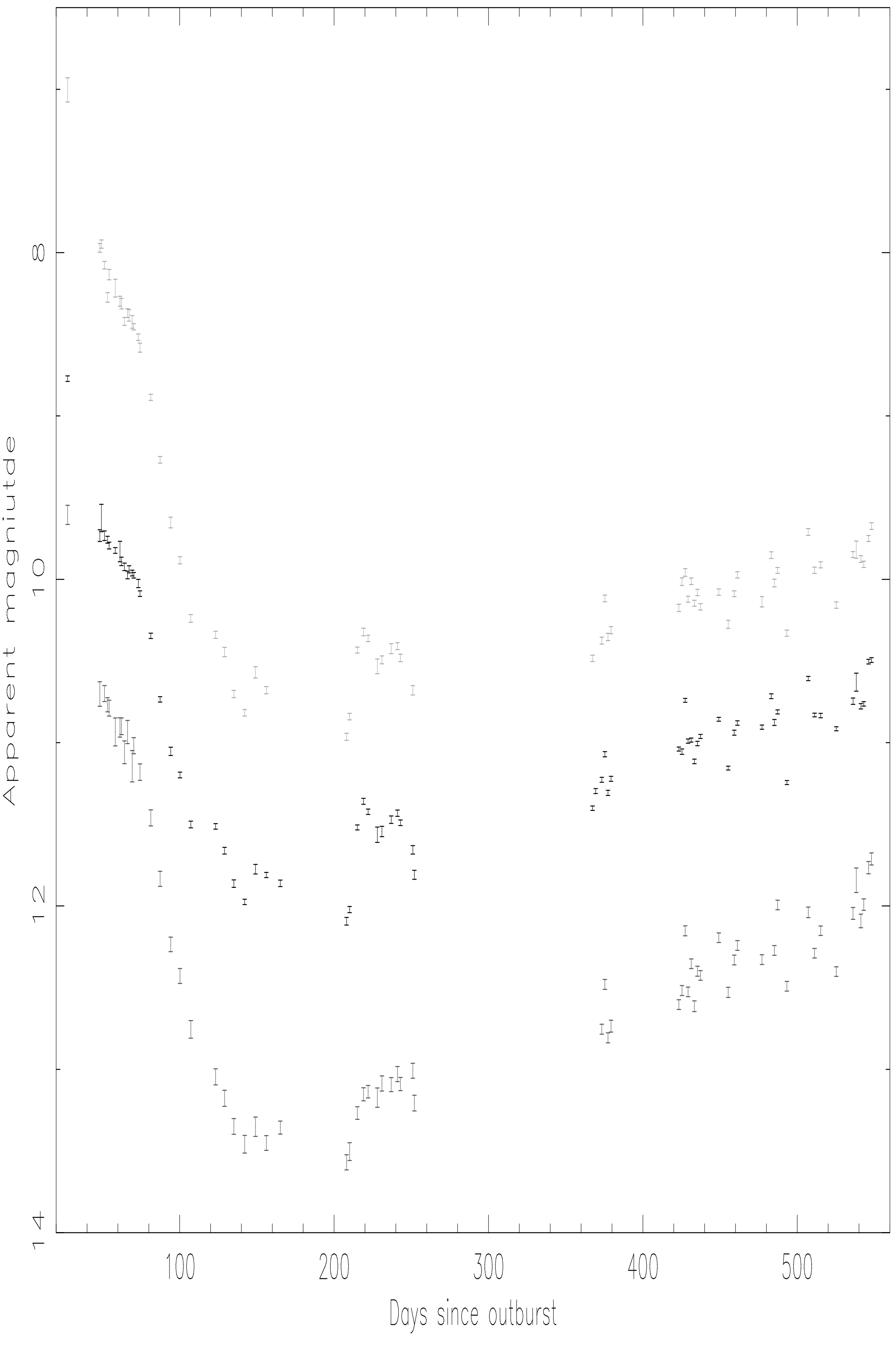

Figure 4.5: r′ (upper), V (middle), and B (lower) lightcurves of RS Oph following the 2006 outburst from Darnley et al. (2008).

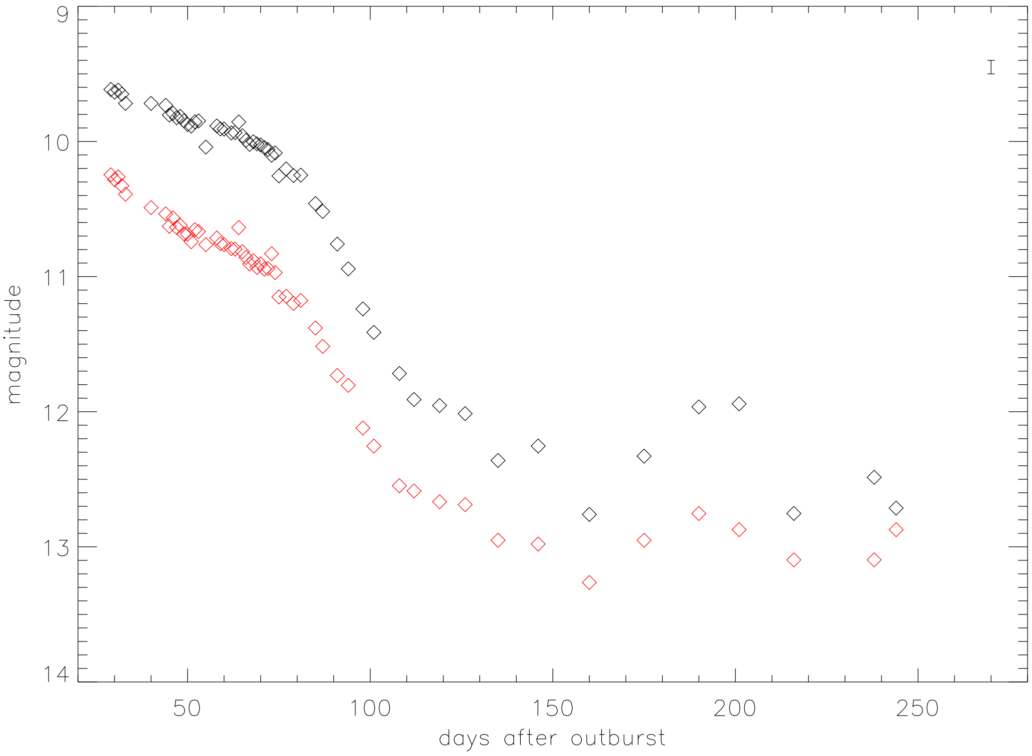

Figure 4.6: u′ (black) and B (red) band lightcurves from UVOT data. A representative error bar is shown in the top right of the figure.

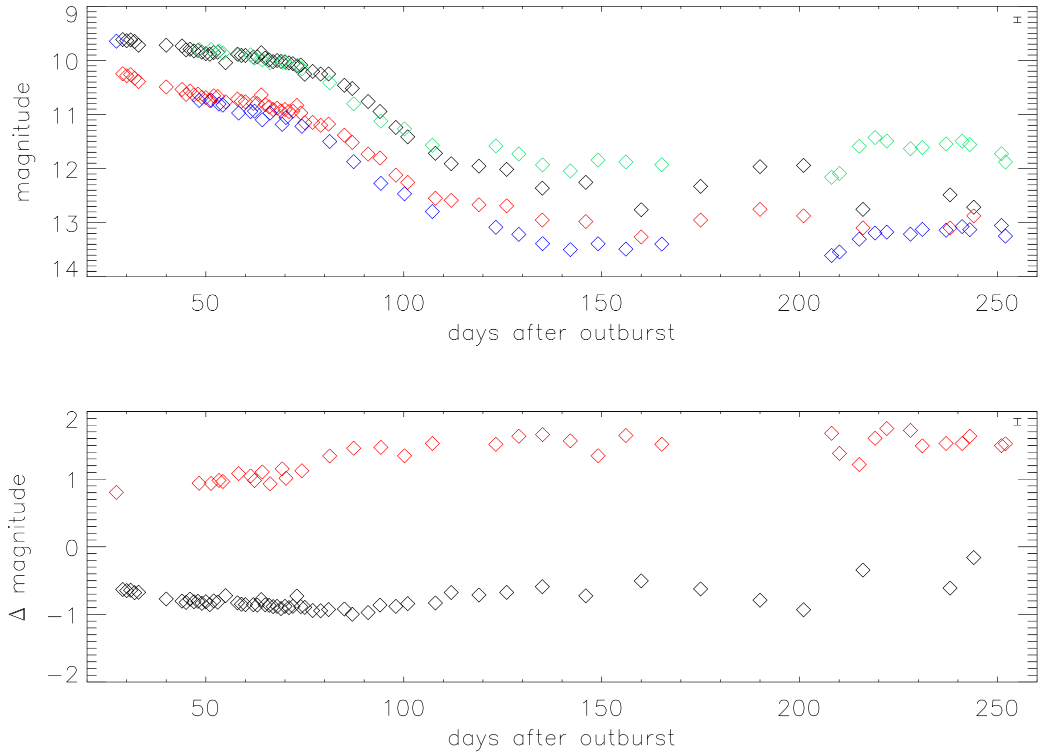

Figure 4.7: Top: u′ (black) and B (red) band lightcurves from UVOT data and V (green) and B (blue) band LT lightcurves from Darnley et al. (2008). Bottom: LT B-V (red) and UVOT u′-B (black) curves. A representative error bar is shown in the top right of the figure.

These lightcurves, shown in Figure 4.6, show a similar profile to the LT lightcurves. There is an initial decline followed by a plateau phase, then a final decline to minimum. The UVOT lightcurves show a minimum at ∼160 days followed by a recovery; the LT lightcurves have a gap in the data between days ∼165 - ∼205 making the date of the minimum difficult to determine. The UVOT and LT curves can be seen together in Fig 4.7; the B band curves can be seen to be similar with the plateau phase ending at ∼80 days, although the UVOT curve is consistently fainter by ∼0.1 mag; the reason for this is likely to be instrumental. The B curves begin to diverge slightly at ∼100 days, with the two curves looking least similar at ∼200 days. The behaviour of the u′ curve is remarkably similar to that of the V band curve, although it appears to begin to decline from the plateau phase slightly sooner than the V curve and diverges more significantly from day ∼100.

The reason for this divergence is unclear, with a possible explanation being that the sensitivity of the detectors becomes lower as the target becomes fainter; unfortunately there is no LT u′ lightcurve to allow further comparison. Also the contribution of background sources to the UVOT spectra will become more significant as the target becomes fainter. Until day ∼100 the shapes of the u′, B and V band lightcurves are similar. Initially the B band curve is ∼1 mag lower than the V curve, i.e. B-V ∼1. The system then becomes redder, approaching B-V ∼2. This change in colour is of note as novae typically become bluer in the post-outburst phase due to the shrinking photosphere at constant bolometric luminosity (Warner 2003), however this is not apparent here for RS Oph. This could be explained by the red giant, which has a significant contribution in the optical, becoming more visible as the photosphere collapses. There is no significant change in the u′-B curve throughout the decline.

There is no consensus explanation for the plateau phase, although there are a couple of common suggestions as to its origin. X-ray studies of the 2006 outburst of RS Oph showed that the emergence of the super-soft source (SSS, Figure 1.12) is coincident with the start of the plateau phase in the optical (Fig. 1.11), suggesting that the plateau is due to optical depth effects. The beginning of the plateau phase in U Sco (∼10 days, Fig 1.6) occurs around the same time that the ejecta become optically thin (see Chapter 2). However for RS Oph it is not clear when the ejecta become optically thin (Banerjee et al. 2009). As the ejecta transitions from being optically thick to optically thin, more material contributes to the luminosity of the target, making it appear brighter. At the same time the material is expanding and the SED peak is moving to higher energies. Therefore the target appears fainter in the optical. These two processes will cancel each other out to some extent, resulting in a change in the decline rate; Hachisu & Kato (2000) attribute the plateau phase to the emergence of the irradiated companion from the receding photosphere. If the SSS is coming from a central region of the binary, such as the surface of the WD (Ness & Starrfield 2009), then it will initially be undetected due to the optically thick nature of the ejecta. As the ejecta become optically thin the SSS will emerge. Therefore the SSS emerging at the same time the plateau phase begins may be due to optical depth effects rather than an underlying link (Balman et al. 1998). An alternative suggestion by Ness et al. (2008) is that the rise of the SSS is due to recombination rather than an optical depth change in the ejecta, which could not be responsible for such a rapid rise in the soft X-ray flux.

4.1.4 Spectroscopy

As mentioned in Section 4.1.1, the 1985 outburst of RS Oph was well observed; by comparing the UVOT observations with observations of the 1985 outburst, both the outbursts and the datasets can be compared, giving an indication of the quality of the UVOT data. Bohigas et al. (1989) observed RS Oph ∼200 days after the optical peak, around the time of the post outburst minimum; the observation taken by

Bohigas et al. (1989) and the UVOT observation at the closest time (day 206) are shown in Fig. 4.8. In both spectra the continuum can be seen to reach a minimum at ∼4000Å with many, although not all, of the same lines being present and the general continuum shape being similar. There is also a clear difference in resolution.

Spectra covering the weeks leading up to the post-outburst minimum (Fig. 4.9) show the decline in strength of emission lines. The evolution of the 2006 outburst throughout the post-outburst minimum can be seen in Fig. 4.10; the variations in the wavelength calibration can clearly be seen, as well as variations in the continuum shape; it is not clear if the changes in the continuum are intrinsic or due to changes in the contribution of the different orders of the grism. Unfortunately no observations were taken in the weeks following the minimum; the first observations after the minimum were taken in February 2007 (Fig. 4.11). In these spectra there are very few features, with the strong transient features being due to background sources. There is also a clear rise in the continuum to the red which is not present in the earlier spectra. Fig. 4.9 again shows that although there is some level of consistency in the wavelength calibration there can be significant differences between any given spectra. Each phase of the outburst and decline is represented in the spectra shown throughout this chapter, from the initial observations following the optical maximum, to the post-outburst minimum and beyond.

Since there is uncertainty regarding the wavelength calibration of each individual spectrum it is difficult to be confident of line identifications. By combining each spectrum taken during the decline to minimum each line should appear at its rest wavelength, assuming that the line centres are randomly distributed around the rest wavelength. The spectra are combined via a simple summation of all the spectra, summing the flux at each wavelength to produce one very high signal-to-noise spectrum. However, this will result in significant broadening of the lines. The non-dereddened and dereddened ($E_{B-V} = 0.73$, Snijders 1987) summed spectra

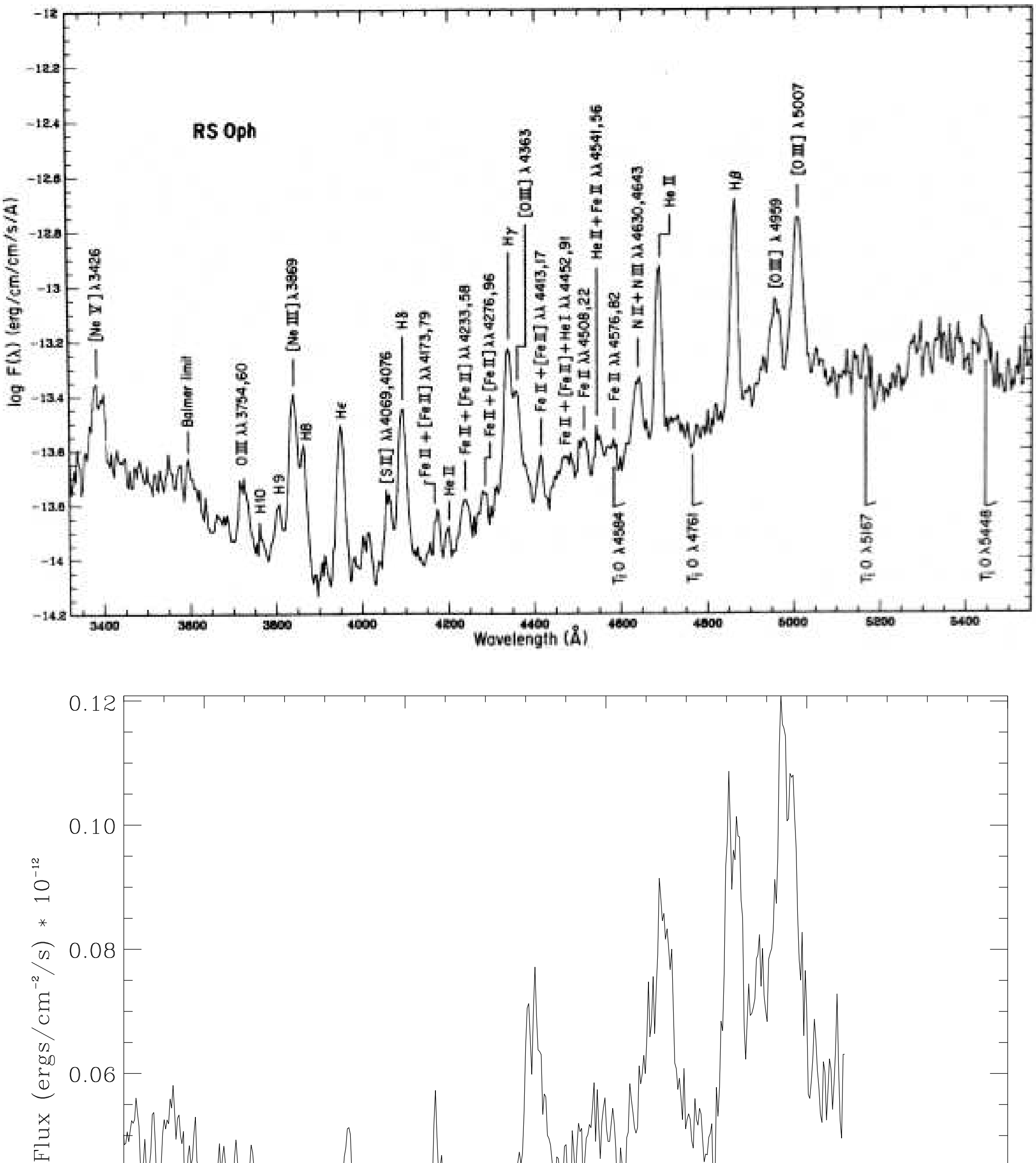

Figure 4.8: Upper: Spectrum of RS Oph 201 days after the maximum of the 1985 outburst taken using the 2.12 metre telescope at the Observatorio Astronomico Nacional by Bohigas et al. (1989). Lower: UVOT spectrum of RS Oph 206 days after the maximum of the 2006 outburst.

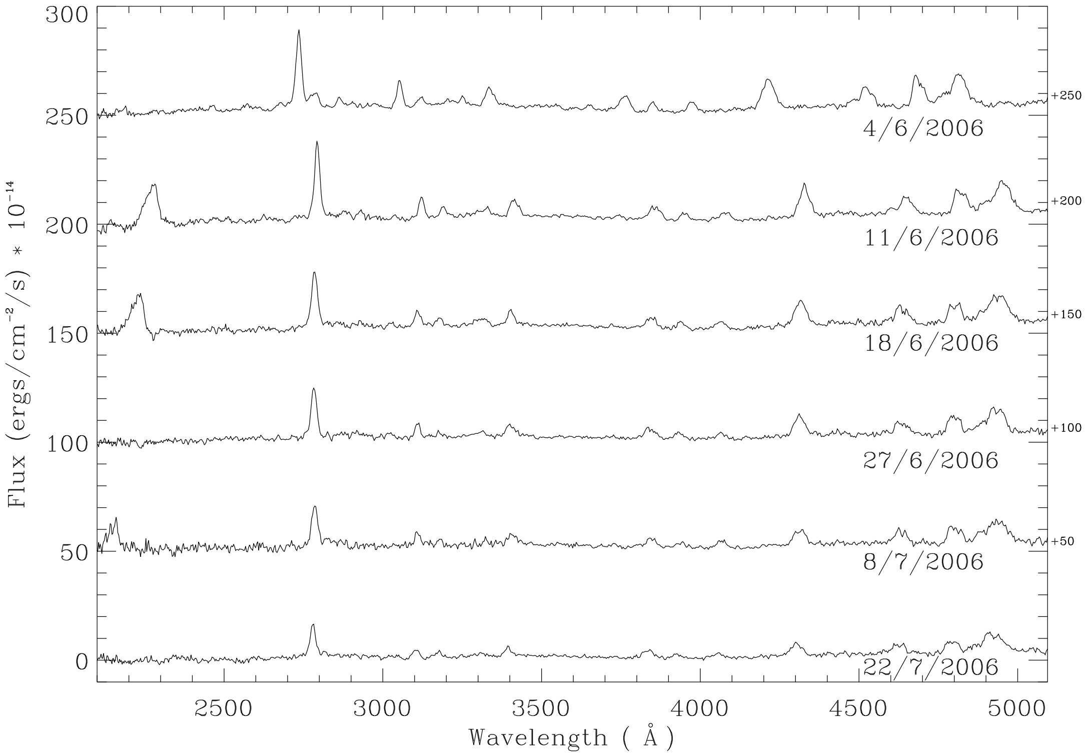

Figure 4.9: UVOT spectra of RS Oph leading up to the post-outburst minimum. Spectra are offset as indicated to the right of the figure.

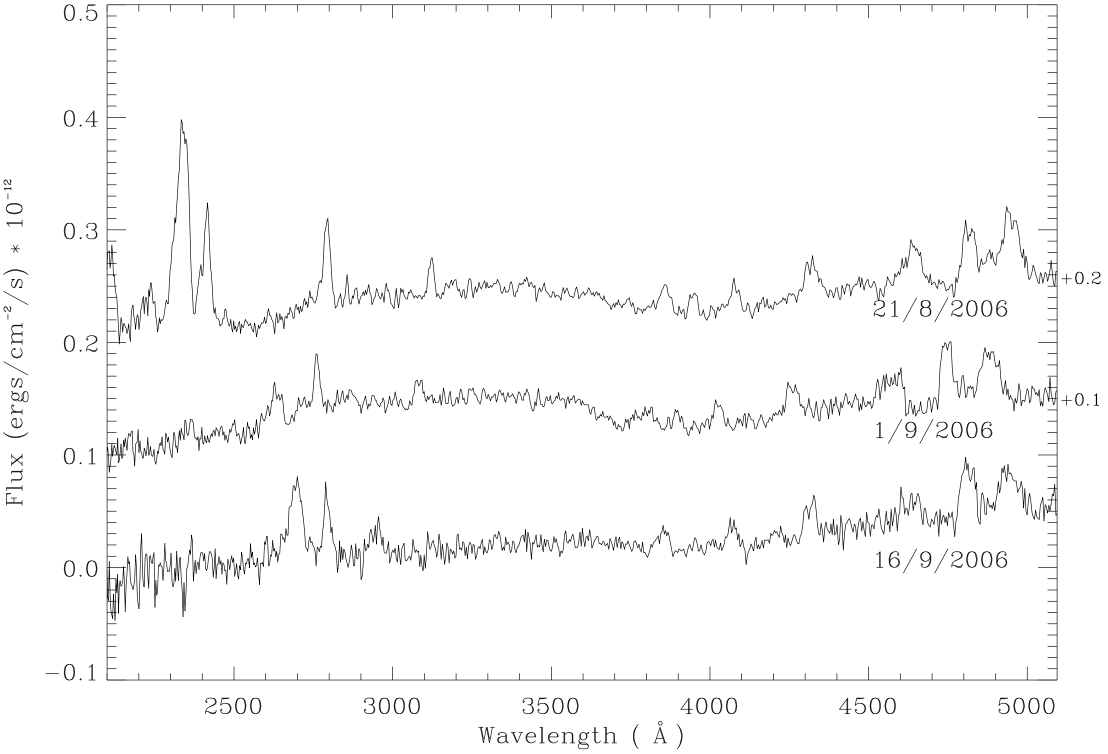

Figure 4.10: UVOT spectra of RS Oph during the post-outburst minimum. Spectra are offset as indicated to the right of the figure.

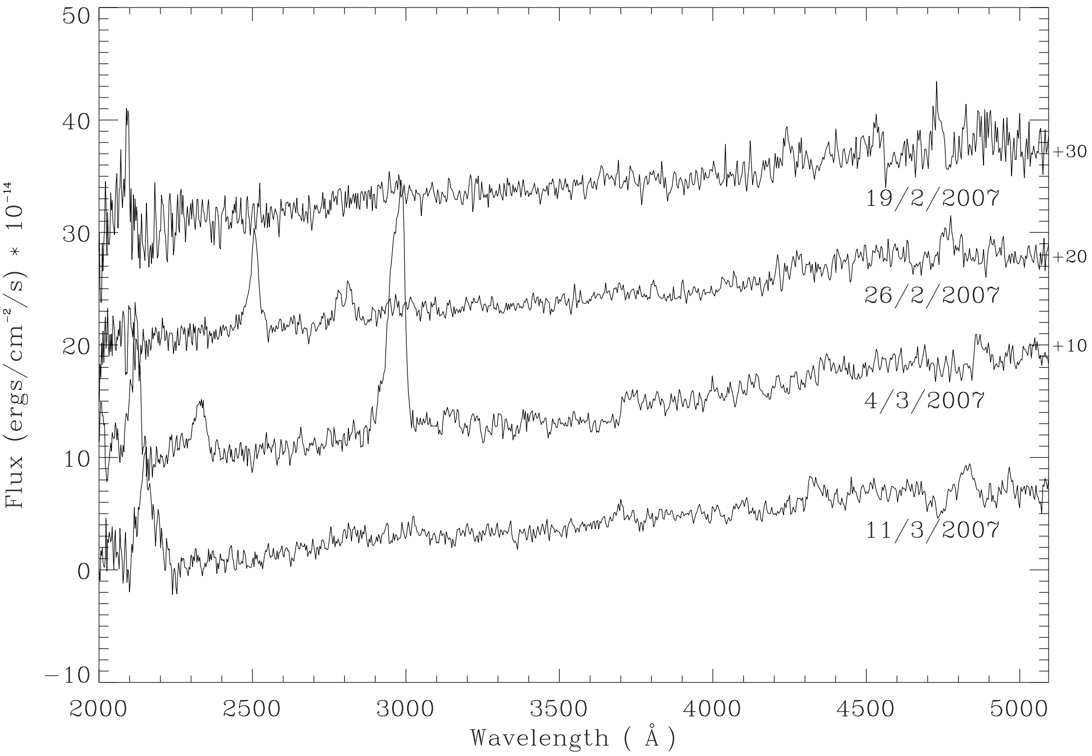

Figure 4.11: UVOT spectra of RS Oph following the post-outburst minimum, taken on 19/2/2007, 26/2, 4/3, 11/3. Transient emission features are due to background sources. Spectra are offset as indicated to the right of the figure.

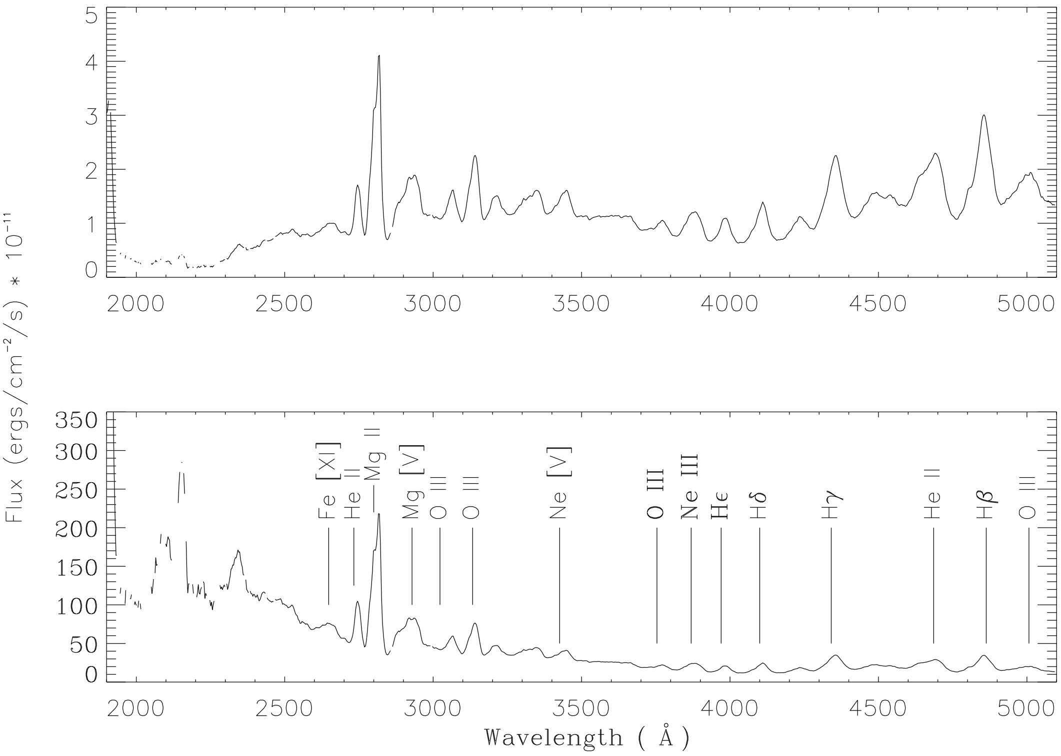

Figure 4.12: Top: Summed non-dereddened spectrum of RS Oph. Bottom: Summed dereddened spectrum of RS Oph. Rest wavelengths of emission lines are indicated by vertical lines.

can be seen in Figure 4.12, with the 2200Å dip, a well known interstellar feature, clearly present in the non-dereddened spectrum and clearly absent in the dereddened spectrum. The summed spectra were created by adding all the spectra taken following the outburst in 2006. Although this causes the temporal information to be lost, it results in the most accurate line identifications given the uncertainties in the wavelength calibration. Several features can be seen to be consistent with the rest wavelength of common emission features, including many identified in the 1985 outburst spectra by Shore et al. (1996). Gaps in the data are due to saturation of the detector.

4.1.5 Summary of results on RS Oph

Swift/UVOT observed the 2006 outburst of RS Oph from ∼30-250 days after the optical peak. The UV/optical spectra taken by UVOT were used to create $u\prime$ and B band lightcurves of the decline of RS Oph which were then used in conjunction with published LT lightcurves to analyse the decline. The colour of the system during the decline was found to evolve from B-V$\simeq$1 in the initial decline phase to B-V$\simeq$2 at the post-outburst minimum. The spectrum of the 2006 outburst ∼200 days after the peak is shown to be similar to the spectrum at a similar time after the 1985 outburst. Emission lines, initially strong after the outburst, are mostly still present by the post-outburst minimum but are largely undetected by the time observations resumed in 2007.

4.2 T Pyxidis

The recurrent nova T Pyxidis was discovered to be in outburst on 2011 April 14.2931 (Waagan et al. 2011). Following the rise there was an initial period of variability followed by a decline as can be seen in Figure 4.13; a brief plateau period began on day ∼150 followed by a long decline. SALT RSS[6] spectra of T Pyx were proposed by the author and obtained in service mode in the late decline phase of the 2011 eruption of T Pyx on days 588-685, as shown in Figure 4.13 and detailed in Table 4.3. The spectra were reduced using standard procedures in IRAF (see Chapter 2) and flux calibrated using an observation of the standard star EG21 taken with the second observation of T Pyx. Unfortunately an observation of the standard was not taken at the time of the other observations, however since the instrument setup was identical in each case and there was no significant change in airmass this is not considered to be a serious issue; the resulting uncertainty from any setup

---

[6] http://www.salt.ac.za/technical-info/instruments/rss/rss-observers-guide-pdf/

and airmass changes is estimated to be small in comparison to the flux calibration uncertainty. The calibration is only valid as a pixel-to-pixel calibration, absolute flux calibration is not possible due to the effective area of the telescope changing during exposures. The spectral resolving power is ∼1000.

4.2.1 Overview of spectra

The four spectra are displayed in Figure 4.14, with the averaged dereddened (E_{B-V} = 0.5, Shore et al. (2011)) spectrum shown in Figure 4.15. Gaps in the data are due to the SALT detector consisting of three segments which do not cover a continuous wavelength range. The strongest lines at ∼5000Å are due to [O III] 4959Å and 5007Å. [O III] 4363Å is also present, with all three lines showing a double-peaked profile which is also seen in spectra taken a year after outburst in April 2012; these profiles are consistent with a bi-polar outflow (Shore et al. 2013b). This double peaked profile is also present in [N II] 5755Å for both these observations and in April 2012 (Shore et al. 2013b). Other lines present include He I 5875Å and H Balmer lines, which do not show a double-peaked profile. All identified lines and their strengths relative to Hβ are shown in Table 4.4; the apparent weakness of Hγ is likely due to blending with [O III] 4363Å.

From these line strengths the abundances in the ejecta during the late decline phase can be determined, as shown in Table 4.5. The total N(He)/N(H) abundance is derived using Equation 2.1 to be 0.161 ± 0.013, approximately twice the solar value (Asplund et al. 2009), and in very good agreement with the model of Contini & Prialnik (1997). The electron temperature and density are assumed to be 2×10^4 K and 10^5 respectively (Shore et al. 2013b).

Date	Start time	Exposure time (s)	RSS configuration	Grating
22/11/2012	00:18:05	1792	Longslit	PG0900
17/12/2012	23:17:31	600	Longslit	PG0900
28/01/2013	19:47:16	2785	Longslit	PG0900
27/02/2013	00:07:42	1350	Longslit	PG0900

Table 4.3: Observing log.

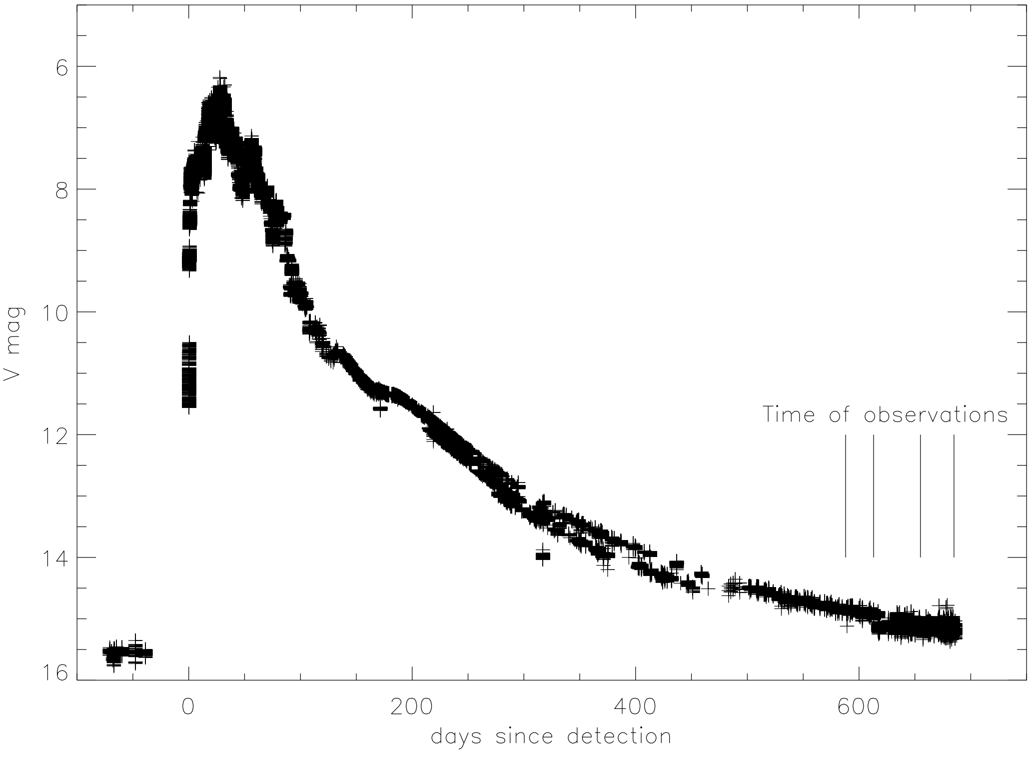

Figure 4.13: V band AAVSO lightcurve of the 2011 eruption of T Pyxidis. Day zero is taken to be at April 14.29.

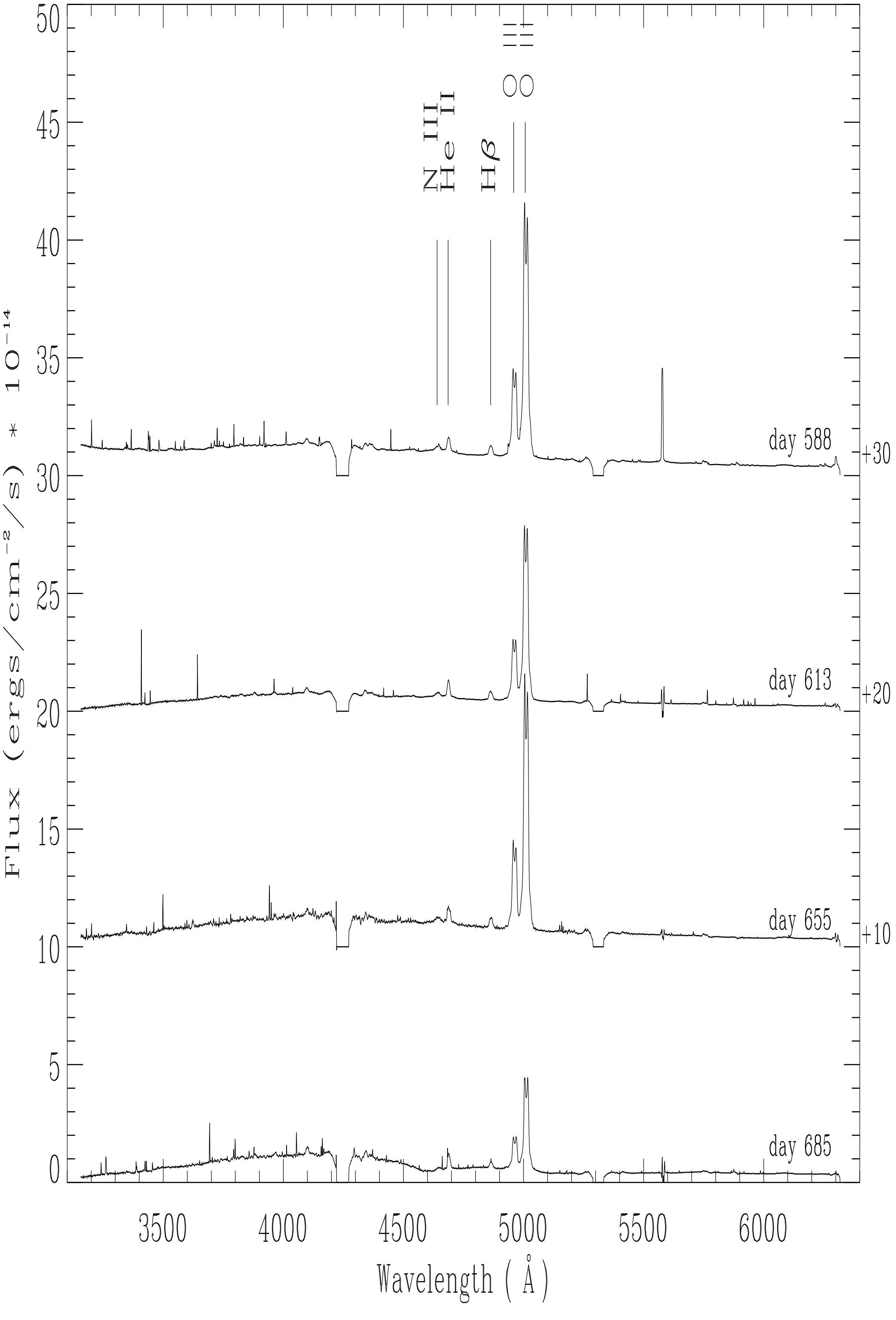

Figure 4.14: SALT spectra of T Pyx, offset as indicated to the right of the figure.

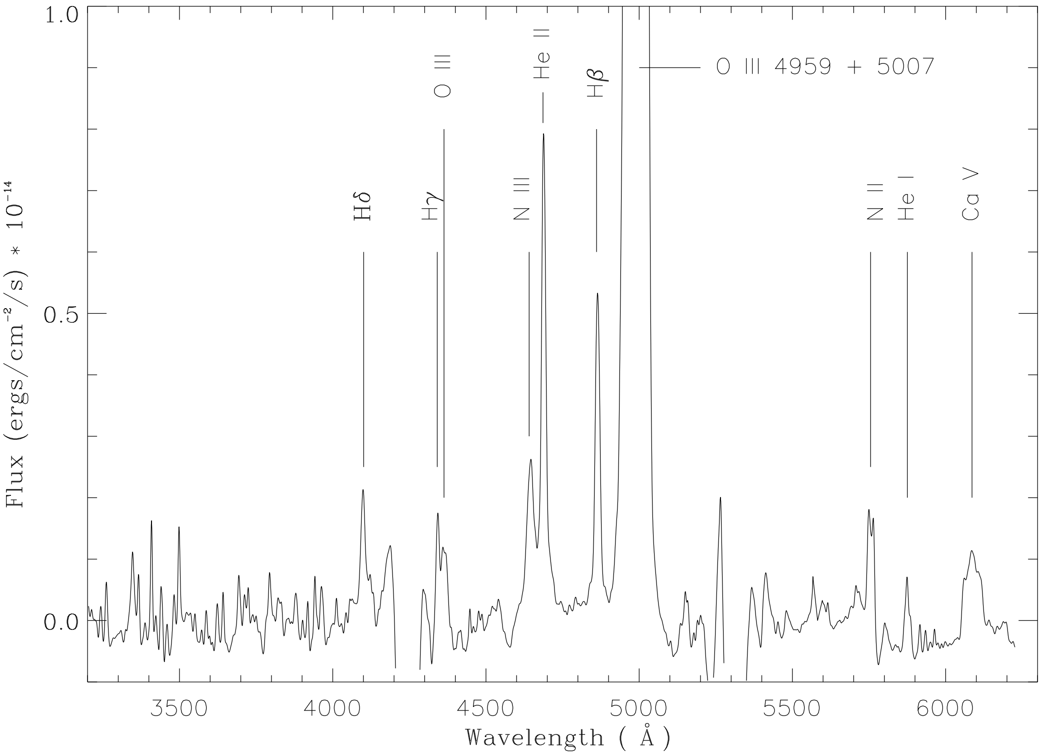

Figure 4.15: Averaged, dereddened, continuum-subtracted spectrum of T Pyx, smoothed with a Gaussian profile of FWHM 1.18Å.

Emission line	Line flux (relative to Hβ)
Hδ	0.35 ± 0.03
Hγ	0.25 ± 0.02
Hβ	1.00
N III 4641Å	0.50 ± 0.01
He II 4686Å	1.25 ± 0.002
[O III] 4363Å	0.43 ± 0.03
[O III] 4959Å	10.11 ± 0.16
[O III] 5007Å	32.24 ± 1.50
[N II] 5755Å	0.56 ± 0.04
He I 5875Å	0.30 ± 0.04
[Ca V] 6086Å	0.82 ± 0.07

Table 4.4: Line strengths for T Pyx relative to Hβ.

Lines used	Ion abundance
He I 5875 / Hδ	0.053 ± 0.008
He I 5875 / Hβ	0.059 ± 0.007
He II 4686 / Hδ	0.100 ± 0.007
He II 4686 / Hβ	0.110 ± 0.002

Table 4.5: Ion abundances during late decline phase of T Pyx.

4.2.2 Summary of results on T Pyx

SALT spectroscopy of the late decline phase of T Pyx has shown that the strongest lines during this phase are due to [O III], He II, and H Balmer emission. Some of these lines have a double-peaked line profile, with others having single peaked line profiles, indicating that these lines are not all formed in the same place. The helium abundance is shown to be approximately twice the solar value. Although an absolute flux calibration is not possible with SALT, pixel-to-pixel calibration still allows some useful analysis to be undertaken. Since T Pyx is relatively bright, V$\sim$15 at the time of these observations, the short observing window allowed by SALT was not an issue.

4.3 Conclusion

The 2006 outburst of RS Oph was observed by Swift/UVOT from $\sim$30 days after the optical peak until the post-outburst minimum at day $\sim$215. The u$'$ lightcurve follows the Liverpool Telescope V band curve closely until day $\sim$100 at which point there is a slight divergence. The UVOT B band curve also follows the LT B band curve closely until day $\sim$100. Each curve shows an initial decline followed by a plateau phase and a final decline. B-V increases throughout the decline, with u$'$-B showing no significant change. The UVOT spectrum on day 206 shows similarities to the IUE spectrum taken at a similar time, with a similar continuum and line spectrum. The emission line strengths decrease as the lightcurve approaches minimum, with the lines being largely gone by the time observations resume in 2007. During the decline from peak the strongest emission lines are due to Mg, O, Ne, He, and H, consistent with identified lines from the outburst in 1985. There are clear issues with the UVOT spectra which make a more complex analysis of the emission spectrum throughout the decline impossible. However as both the wavelength and flux calibrations improve this dataset will become fully exploitable.

CHAPTER 4

Following the 2011 outburst of T Pyx, SALT optical spectra of the system during the late decline phase were obtained. The strongest features in these spectra are due to [O III], with He and H Balmer lines also present. From these spectra the helium abundance by number was found to be N(He)/N(H)= 0.161 ± 0.013.

Chapter 5

Conclusions and Future Work

5.1 U Scorpii

In Chapter 2 the 2010 outburst of U Sco was investigated, with the reddening of the system, the helium abundance of the ejecta, and the velocity of the ejecta being determined. The reddening was found to be $E_{B-V} = 0.17 \pm 0.14$, consistent with previous estimates (e.g. Barlow et al. (1981)) which range from $0.09 - 0.36$. The helium abundance in the ejecta of the outburst was determined to be He/H $= 0.122 \pm 0.018$, indicating that the ejecta are not significantly enriched relative to solar (He/H $= 0.085$, Asplund et al. 2009), contrary to previous works, and that the material accreted in the inter-outburst period is not enriched. Given that such a wide range of values for the helium abundance have been determined, both for different outbursts and in studies of the same outburst, this is a subject that will have to be revisited when the next outburst occurs. In order to derive an accurate value, it is essential that in future works the methodologies which resulted in a range of values being determined are not repeated. For an accurate He abundance determination, both He I and He II lines must be observed, preferably multiples of each. These observations must take place after the ejecta has become optically thin. As new instruments with better resolution and wavelength coverage become available, estimates of line fluxes will become more accurate, especially in terms of broad component flux, allowing for more accurate abundance determinations. Deriving the abundances of elements other than helium should also be an aim for future studies. The ejecta were found to be emitted at velocities of up to ∼10000 $\mathrm{km s^{-1}}$ with emission lines showing broad and narrow components. Determinations of the terminal velocity of the ejecta will become more accurate as the resolution of instruments improves. For now, better signal to noise must be achieved in order for this to be better investigated.

In Chapter 3 the nature of U Sco in quiescence was investigated, with several outstanding questions being addressed. The system was found to return to photometric quiescence before it returns to spectroscopic quiescence; VLT spectra obtained ∼18 months after the 2010 outburst show several spectral lines not present in the spectra of Johnston & Kulkarni (1992) despite the system having returned to the pre-outburst V magnitude by this time. SALT spectra taken ∼30 months after outburst appear much more similar to the spectra of Johnston & Kulkarni (1992) with a flatter continuum and He II 4686Å being the strongest of the few lines present. The spectral class of the secondary has also been investigated, with the best fits to the VLT spectra suggesting a class of $\mathrm{F7}^{+5}_{-6}$, although the effect of irradiation from the hot component must also be considered. The SALT spectra, taken 848 and 909 days after the 2010 outburst, were compared to stars in the atlas of Sánchez-Blázquez et al. (2006) and suggest a hot G star or a cool F star respectively. The accretion disc in U Sco has been shown to take at least 18 months to fully re-establish, as the VLT spectra all show a significant rise in the continuum at shorter wavelengths which is not prominent in the SALT spectra taken at later times. This is interpreted as being due to the disc becoming more luminous as it re-establishes itself after outburst, resulting in the peak of the emission moving into the UV and the contribution in the optical becoming less significant. Although it is not possible without UV observations to say if the disc is fully re-established by ∼30 months after outburst, it appears that by ∼18 months after outburst it is not. The mass accretion rate at the time of the VLT observations is found to be $\sim 10^{-9}\,\mathrm{M}_{\odot}\,\mathrm{yr}^{-1}$, inconsistent with the rates derived from the strength of the He II 4686Å line, indicating that the disc is not in the steady state by ∼18 months after outburst.

In order to determine the difference between orbital phase variations and long-term variations in U Sco, more observations are needed. Phase resolved spectroscopy, preferably over several periods, would help to determine the variations due to irradiation of the companion, the hot spot, and eclipses. Spectra taken over several months would allow the longer term variations, which are likely due to activity in the accretion disc, to be better investigated. The variations in the quiescent lightcurve of ∼1 mag suggest that the continuum level will also undergo significant variation. Spectra taken at phase 0.0 would be particularly helpful as at this time the disc is largely obscured by the companion and so the spectrum should be dominated by the companion; conversely the spectrum should have the maximum contribution from the disc at phase 0.5.

More sophisticated models could be used for the fitting procedure; the model atmospheres used in this work do not account for the entirety of the physics at work in U Sco. A radiative transfer code, such as Tlusty (Hubeny & Lanz 1995), is one option for including more physics.

5.2 RS Ophiuchi

RS Oph last went into outburst in 2006, following which extensive UV observations were obtained with Swift/UVOT. These observations began ∼30 days after the optical peak and continued until after the post-outburst minimum. These observations were used to produce lightcurves of the decline by folding the spectra through filter response functions and integrating the total light. These lightcurves can be seen in

Chapter 4 where they are compared to contemporaneous Liverpool Telescope observations; the UVOT curves mirror the LT curves until day ∼100 at which point they begin to diverge. B-V increases from ∼1 to ∼2 from day ∼50 to day ∼100, with the u′-B curve showing no significant change. The change in colour of the system can be ascribed to the increasing contribution of the red giant as the ejecta disperses and the photosphere of the WD shrinks.

As both the wavelength and flux calibration of UVOT improve, the full potential of this dataset will become exploitable. An accurate wavelength calibration will make line identifications much safer, allowing abundance analyses to be performed. An accurate flux calibration will allow the behaviour leading up to and during the post outburst minimum to be investigated. Line profiles and velocities can be used to characterise the geometry of the ejecta, with the rise and fall of emission lines of different ionisations detailing the evolution of the spectrum through the phases defined by Williams et al. (1991).

Future work on RS Oph, besides further study of the UV regime and studies of the 2006 outburst, should focus on characterising the dust formed in RS Oph and constraining the nature of the red giant companion, building on the work done by Rushton et al. (2010); Pavlenko (2008) and Evans et al. (2007b). Further study of the X-ray behaviour, both from shocks between the ejecta and the red giant wind and the super-soft source, should also be a priority.

5.3 T Pyxidis

The 2011 outburst of T Pyx was well observed from the radio (Nelson et al. 2012) to the X-ray (Balman 2012) and optical (Shore et al. 2011, 2013b), with some of these observations still ongoing. These spectra could be used to form part of a multi-wavelength analysis of the late time decline of T Pyx, and also a study following the optical spectroscopic evolution of T Pyx from outburst to final decline. Since there are several emission lines present it should be possible to determine the reddening to the system, which is still poorly constrained, and also perform a full abundance analysis. The helium abundance has been determined to be N(He)/N(H)= 0.161 ± 0.013. In principle it should also be possible to perform a similar analysis for T Pyx as was undertaken in Chapter 3 for U Sco in order to characterise the accretion disc; this analysis is simplified by the lack of a significant contribution in the optical from the companion (Uthas et al. 2010).

Since the recurrence period of T Pyx appears to be increasing, and the gap between the two most recent outbursts was 45 years, it is unlikely that there will be another outburst for some time. Fortunately, T Pyx is a slow nova and the 2011 outburst was very well observed, so there is a wealth of data available for anyone wishing to study this system. The nova community should also make an effort to continue to monitor T Pyx for several years, both in order to track the long decline to minimum and to observe the system in quiescence. As noted when discussing U Scorpii, in order to better understand the outbursts of recurrents it is necessary to observe them in quiescence. Since T Pyx is not very faint, V$\sim$15.5, this should not be too much of a challenge and would greatly increase our understanding of this system.

5.4 The bigger picture

In this thesis studies of the recurrent novae U Scorpii, RS Ophiuchi, and T Pyxidis have demonstrated that recurrents play an important role in binary evolution, enrichment of the interstellar medium (ISM), and accretion physics. From T Pyx, with a period of hours and a main sequence companion, to RS Oph, with a period of over a year and a red giant companion, recurrent novae encompass a wide range of binary systems which form in a variety of ways. Understanding the short and variable recurrence periods of these objects is a challenge to theorists, and observers must continue to monitor recurrents for several years after outburst in order to better understand the quiescent behaviour which drives the outbursts.

Recurrent novae are useful systems for testing the physics of accretion discs, with either wind accretion or Roche-lobe overflow being responsible for accretion from system to system. Understanding these processes, with help from extensive observations and modelling in quiescence, is essential if the recurrence periods are to be explained. Accretion processes in novae cover huge discs in symbiotic systems with orbital periods of over a year, as in the case of RS Oph, and tiny discs in systems with orbital periods of a few minutes like T Pyx. Understanding how the same physics can be behind accretion in both of these systems, and in other systems where there are complex effects due to magnetic fields, is the challenge for theorists in the coming years.

Recurrent novae make a significant contribution to the ISM, as demonstrated by the spectra and abundance studies in this thesis and published literature. Each system differs in its contribution based on the nature of the white dwarf and the material accreted from the companion. Therefore, properly characterising both the primary and companion in these systems is essential when trying to understand their contribution to the ISM.

Recurrent novae are amongst the most promising candidates for SNe Ia progenitors. Although it is not clear if the underlying WDs in these systems are CO dwarfs, and it is uncertain whether the WDs are gaining or losing mass after each outburst cycle, if these two conditions are met then the high mass of the white dwarfs in most recurrents make them the ideal candidates.

References

Adamakis, S., Eyres, S. P. S., Sarkar, A., & Walsh, R. W. 2011, *Mon. Not. Roy. Astron. Soc.*, 414, 2195

Amôres, E. B. & Lépine, J. R. D. 2005, *Astron. J.*, 130, 659

Andrade, A. A. & Friedjung, M. 1989, *Astron. Astrophys.*, 224, 187

Anupama, G. C. & Dewangan, G. C. 2000, *Astron. J.*, 119, 1359

Appenzeller, I. & Oestreicher, R. 1988, *Astron. J.*, 95, 45

Arp, H. C. 1956, *Astron. J.*, 61, 15

Ashok, N. M., Banerjee, D. P. K., Varricatt, W. P., & Kamath, U. S. 2006, *Mon. Not. Roy. Astron. Soc.*, 368, 592

Asplund, M., Grevesse, N., Sauval, A. J., & Scott, P. 2009, *Ann. Rev. Astron, Astrophys.*, 47, 481

Bailey, S. 1920b, Harvard Bull., 734

Baker, J. G. & Menzel, D. H. 1938, *Astrophys. J.*, 88, 52

Balman, S. 2012, ArXiv e-prints, 2012arXiv1208.6120B

Balman, S., Krautter, J., & Oegelman, H. 1998, *Astrophys. J.*, 499, 395

Banerjee, D. P. K., Das, R. K., & Ashok, N. M. et al including Maxwell, M. P. 2010, *Mon. Not. Roy. Astron. Soc.*, 408, L71

Banerjee, D. P. K., Das, R. K., & Ashok, N. M. 2009, *Mon. Not. Roy. Astron. Soc.*, 399, 357

Barlow, M. J., Brodie, J. P., Brunt, C. C., et al. 1981, *Mon. Not. Roy. Astron. Soc.*, 195, 61

Barnsley, R. M., Smith, R. J., & Steele, I. A. 2012, Astronomische Nachrichten, 333, 101

Barry, R. K., Mukai, K., Sokoloski, J. L., et al. 2008, Astronomical Society of the Pacific Conference Series, Vol. 401, On the distance of RS Oph (Astronomical society of the pacific), 52–62

Bath, G. T. & Pringle, J. E. 1981, *Mon. Not. Roy. Astron. Soc.*, 194, 967

Bode, M. F. & Evans, A. 2008, Classical Novae, 2nd Edition. Edited by M.F. Bode and A. Evans. Cambridge Astrophysics Series, No. 43, Cambridge: Cambridge University Press, 2008.

Bode, M. F., Harman, D. J., O'Brien, T. J., et al. 2007, *Astrophys. J. Letters*, 665, L63

Bode, M. F., O'Brien, T. J., Osborne, J. P., et al. 2006, *Astrophys. J.*, 652, 629

Bode, M. F., Osborne, J. P., Page, K. L., et al. 2009, The Astronomer's Telegram, 2025, 1

Bohigas, J., Echevarria, J., Diego, F., & Sarmiento, J. A. 1989, *Mon. Not. Roy. Astron. Soc.*, 238, 1395

Bonnell, I. A. 1994, *Mon. Not. Roy. Astron. Soc.*, 269, 837

Bonnell, I. A. 2001, in The Formation of Binary Stars, ed. H. Zinnecker & R. Mathieu, Proc. IAU Symposium 200 (Astronomical Society of the Pacific), 23

Brandi, E., Quiroga, C., Mikołajewska, J., Ferrer, O. E., & García, L. G. 2009, *Astron. Astrophys.*, 497, 815

Burstein, D. & Heiles, C. 1982, *Astron. J.*, 87, 1165

Capaccioli, M., della Valle, M., Rosino, L., & D'Onofrio, M. 1989, *Astron. J.*, 97, 1622

Cassatella, A., Hassall, B. J. M., Harris, A., & Snijders, M. A. J. 1985, in ESA Special Publication, Vol. 236, Recent Results on Cataclysmic Variables. The Importance of IUE and Exosat Results on Cataclysmic Variables and Low-Mass X-Ray Binaries, ed. W. R. Burke, 281–284

Castor, J. I. & van Blerkom, D. 1970, *Astrophys. J.*, 161, 485

Ciardullo, R., Tamblyn, P., Jacoby, G. H., Ford, H. C., & Williams, R. E. 1990, *Astron. J.*, 99, 1079

Cohen, J. G. 1985, *Astrophys. J.*, 292, 90

Contini, M. & Prialnik, D. 1997, *Astrophys. J.*, 475, 803

Darnley, M. J., Black, D. T. R., Bode, M. F., et al. 2008, in Astronomical Society of the Pacific Conference Series, Vol. 401, RS Ophiuchi (2006) and the Recurrent Nova Phenomenon, ed. A. Evans, M. F. Bode, T. J. O'Brien, & M. J. Darnley, 355

Darnley, M. J., Bode, M. F., Kerins, E., et al. 2006, *Mon. Not. Roy. Astron. Soc.*, 369, 257

Diaz, M., Williams, R., Luna, G., Moraes, M., & Takeda, L. 2012, *Memorie della Societ Astronomia Italiana*, 83, 758

Diaz, M. P., Williams, R. E., Luna, G. J., Moraes, M., & Takeda, L. 2010, *Astron. J.*, 140, 1860

Dinerstein, H. & Hoffleit, D. 1973, Information Bulletin on Variable Stars, 845, 1

Dobrzycka, D. & Kenyon, S. J. 1994, *Astron. J.*, 108, 2259

Downes, R. A. & Duerbeck, H. W. 2000, *Astron. J.*, 120, 2007

Drake, J. J., Laming, J. M., Ness, J.-U., et al. 2009, *Astrophys. J.*, 691, 418

Drake, J. J. & Orlando, S. 2010, *Astrophys. J. Letters*, 720, L195

Dürbeck, H. W., Dümmler, R., Seitter, W. C., Leibowitz, E. M., & Shara, M. M. 1993, The Messenger, 71, 19

Erro, L. E. 1949, IAU Circular, 1208, 1

Evans, A., Gehrz, R. D., Helton, L. A., et al. 2012, *Mon. Not. Roy. Astron. Soc.*, 424, L69

Evans, A., Kerr, T., Yang, B., et al. 2007a, *Mon. Not. Roy. Astron. Soc.*, 374, L1

Evans, A., Krautter, J., Vanzi, L., & Starrfield, S. 2001, *Astron. Astrophys.*, 378, 132

Evans, A., Woodward, C. E., Helton, L. A., et al. 2007b, *Astrophys. J. Letters*, 671, L157

Eyres, S. P. S., O'Brien, T. J., Beswick, R., et al. 2009, *Mon. Not. Roy. Astron. Soc.*, 395, 1533

Fujimoto, M. Y. 1982a, *Astrophys. J.*, 257, 767

Fujimoto, M. Y. 1982b, *Astrophys. J.*, 257, 752

Gaposchkin, C. H. P. 1957, The galactic novae. (Interscience Publishers)

Gehrels, N., Chincarini, G., Giommi, P., et al. 2004a, *Astrophys. J.*, 611, 1005

Gehrels, N., Chincarini, G., Giommi, P., et al. 2004b, *Astrophys. J.*, 611, 1005

Gehrz, R. D., Grasdalen, G. L., & Hackwell, J. A. 1985, *Astrophys. J. Letters*, 298, L47

Gehrz, R. D., Truran, J. W., Williams, R. E., & Starrfield, S. 1998, *Pub. Astron. Soc. Pac.*, 110, 3

Gil-Pons, P., García-Berro, E., José, J., Hernanz, M., & Truran, J. W. 2003, *Astron. Astrophys.*, 407, 1021

Godon, P. & Sion, E. M. 2005, *Mon. Not. Roy. Astron. Soc.*, 361, 809

Greenhouse, M. A., Grasdalen, G. L., Woodward, C. E., et al. 1990, *Astrophys. J.*, 352, 307

Gromadzki, M., Mikolajewski, M., Tomov, T., et al. 2006, *Acta Astronomica*, 56, 97

Hachisu, I. 2003, in Astronomical Society of the Pacific Conference Series, Vol. 303, Symbiotic Stars Probing Stellar Evolution, ed. R. L. M. Corradi, J. Mikolajewska, & T. J. Mahoney, 261

Hachisu, I. & Kato, M. 2000, *Astrophys. J. Letters*, 536, L93

Hachisu, I. & Kato, M. 2012, *Baltic Astronomy*, 21, 68

Hachisu, I., Kato, M., & Luna, G. J. M. 2007, *Astrophys. J.*, 659, L153

Hachisu, I., Kato, M., Nomoto, K., & Umeda, H. 1999, *Astrophys. J.*, 519, 314

Hack, M., Selvelli, P., Bianchini, A., & Duerbeck, H. W. 1993, NASA Special Publication, 507, 413

Han, Z. & Podsiadlowski, P. 2004, *Mon. Not. Roy. Astron. Soc.*, 350, 1301

Hanes, D. A. 1985, *Mon. Not. Roy. Astron. Soc.*, 213, 443

Hassall, B. J. M. 1985, *Mon. Not. Roy. Astron. Soc.*, 216, 335

Hayasaki, K. & Okazaki, A. T. 2004, *Mon. Not. Roy. Astron. Soc.*, 350, 971

Hernanz, M. & Tatischeff, V. 2012, *Baltic Astronomy*, 21, 62

Heywood, I., O'Brien, T. J., Eyres, S. P. S., Bode, M. F., & Davis, R. J. 2005, *Mon. Not. Roy. Astron. Soc.*, 362, 469

Hirosawa, K., Narumi, H., Kanai, K., & Renz, W. 2006, Central Bureau Electronic Telegrams, 399, 1

Hjellming, R. M., van Gorkom, J. H., Seaquist, E. R., et al. 1986, *Astrophys. J.*, 305, L71

Horne, K., Marsh, T. R., Cheng, F. H., Hubeny, I., & Lanz, T. 1994, *Astrophys. J.*, 426, 294

Hounsell, R., Bode, M. F., Hick, P. P., et al. 2010, *Astrophys. J.*, 724, 480

Howarth, I. D. 1983, *Mon. Not. Roy. Astron. Soc.*, 203, 301

Howarth, I. D., Murray, J., Mills, D., & Berry, D. S. 2004, Starlink User Note 50

Hubeny, I. & Lanz, T. 1995, *Astrophys. J.*, 439, 875

Hummer, D. G. & Storey, P. J. 1987, *Mon. Not. Roy. Astron. Soc.*, 224, 801

Ichikawa, S. & Osaki, Y. 1992, *Pub. Astron. Soc. Japan*, 44, 15

Iijima, T. 2002, *Astron. Astrophys.*, 387, 1013

Iijima, T. 2009, *Astron. Astrophys.*, 505, 287

Imamura, K. & Tanabe, K. 2012, *Pub. Astron. Soc. Japan*, 64, L9

Jacoby, G. H., Hunter, D. A., & Christian, C. A. 1984, *Astrophys. J. Suppl.*, 56, 257

Jeans, J. H. 1928, Astronomy and cosmogony

Johnston, H. M. & Kulkarni, S. R. 1992, *Astrophys. J.*, 396, 267

Jovanović, P., Popović, L. Č., Stalevski, M., & Shapovalova, A. I. 2010, *Astrophys. J.*, 718, 168

Jurdana-Šepić, R., Ribeiro, V. A. R. M., Darnley, M. J., Munari, U., & Bode, M. F. 2012, *Astron. Astrophys.*, 537, A34

Kafka, S. & Williams, R. 2011, *Astron. Astrophys.*, 526, A83

Kasliwal, M. M., Cenko, S. B., Kulkarni, S. R., et al. 2011, *Astrophys. J.*, 735, 94

Kingdon, J. & Ferland, G. J. 1995, *Astrophys. J.*, 442, 714

Kurucz, R. L. 1979, *Astrophys. J. Suppl.*, 40, 1

Kurucz, R. L. 1992, in The Stellar Populations of Galaxies, ed. B. Barbuy & A. Renzini, Proc. IAU Symposium 149 (Kluwer Academic Publishers), 225

Lederle, C. & Kimeswenger, S. 2003, *Astron. Astrophys.*, 397, 951

Liller, W. & Mayer, B. 1987, *Pub. Astron. Soc. Pac.*, 99, 606

Luna, G. J. M., Montez, R., Sokoloski, J. L., Mukai, K., & Kastner, J. H. 2009, *Astrophys. J.*, 707, 1168

Lynden-Bell, D. & Pringle, J. E. 1974, *Mon. Not. Roy. Astron. Soc.*, 168, 603

MacDonald, J., Fujimoto, M. Y., & Truran, J. W. 1985, *Astrophys. J.*, 294, 263

Mason, E. 2011, *Astron. Astrophys.*, 532, L11

Mason, E., Ederoclite, A., Williams, R. E., Della Valle, M., & Setiawan, J. 2012, *Astron. Astrophys.*, 544, A149

Mason, E., Orio, M., Mukai, K., et al. 2013, *Mon. Not. Roy. Astron. Soc.*, 436, 212

Mason, E., Skidmore, W., Howell, S. B., et al. 2000, *Mon. Not. Roy. Astron. Soc.*, 318, 440

Maxwell, M. P., Rushton, M. T., Darnley, M. J., et al. 2012, *Mon. Not. Roy. Astron. Soc.*, 419, 1465

Mayo, S. K., Wickramasinghe, D. T., & Whelan, J. A. J. 1980, *Mon. Not. Roy. Astron. Soc.*, 193, 793

McLaughlin, D. B. 1960, in Stellar Atmospheres, ed. J. L. Greenstein (University of Chicago Press), 585

Mihalas, D., Hummer, D. G., Mihalas, B. W., & Daeppen, W. 1990, *Astrophys. J.*, 350, 300

Montes, D., Ramsey, L. W., & Welty, A. D. 1999, *Astrophys. J. Suppl.*, 123, 283

Moore, K. & Bildsten, L. 2012, *Astrophys. J.*, 761, 182

Morgan, G. E., Ringwald, F. A., & Prigge, J. W. 2003, *Mon. Not. Roy. Astron. Soc.*, 344, 521

Munari, U., Zwitter, T., Tomov, T., et al. 1999, *Astron. Astrophys.*, 347, L39

Nelson, T., Chomiuk, L., Roy, N., et al. 2012, ArXiv e-prints, 2012arXiv1211.3112N

Ness, J., Starrfield, S., van Rossum, D. R., & Schönrich, R. 2008, Astronomical Society of the Pacific Conference Series, Vol. 401, The X-ray Spectra from the Shock and the White Dwarf: Two Laboratories in One Spectrum, ed. A. Evans, M. F. Bode, T. J. O'Brien, & M. J. Darnley, 274

Ness, J.-U., Schaefer, B. E., Dobrotka, A., et al. 2012, *Astrophys. J.*, 745, 43

Ness, J.-U. & Starrfield, S. 2009, in Astronomical Society of the Pacific Conference Series, Vol. 404, The Eighth Pacific Rim Conference on Stellar Astrophysics: A Tribute to Kam-Ching Leung, ed. B. Soonthornthum, S. Komonjinda, K. S. Cheng, & K. C. Leung, 77

Ness, J.-U., Starrfield, S., Beardmore, A. P., et al. 2007, *Astrophys. J.*, 665, 1334

Nomoto, K. & Kondo, Y. 1991, *Astrophys. J.*, 367, 19

O'Brien, T. J., Bode, M. F., Porcas, R. W., et al. 2006, *Nature*, 442, 279

Oppenheimer, B. D. & Mattei, J. A. 1993, Journal of the American Association of Variable Star Observers (JAAVSO), 22, 105

Orio, M., Behar, E., Gallagher, J., et al. 2012, *Mon. Not. Roy. Astron. Soc.*, 361

Osborne, J. P., Page, K. L., Beardmore, A. P., et al. 2011, *Astrophys. J.*, 727, 124

Osterbrock, D. E. & Ferland, G. J. 2006, Astrophysics of Gaseous Nebulae and Active Galactic Nuclei (University Science Books)

Pagnotta, A., Schaefer, B. E., Xiao, L., Collazzi, A. C., & Kroll, P. 2009, *Astron. J.*, 138, 1230

Patterson, J., Kemp, J., Shambrook, A., et al. 1998, *Pub. Astron. Soc. Pac.*, 110, 380

Patterson, J. & Raymond, J. C. 1985, *Astrophys. J.*, 292, 550

Pavlenko, Y. V. 2008, *Astron. Astrophys.*, 485, 541

Pavlenko, Y. V., Woodward, C. E., Rushton, M. T., Kaminsky, B., & Evans, A. 2010, *Mon. Not. Roy. Astron. Soc.*, 404, 206

Peimbert, M. & Torres-Peimbert, S. 1987, *Revista Mexicana de Astronomia y Astrofisica*, 15, 117

Pickering, E. 1905, Harvard Coll. Obs. Circ., 99

Pickering, E. 1913, Harvard Coll. Circ., 179

Plaut, L. 1958, Leiden Ann, 21

Pogson, N. 1865, Astronomische Nachrichten, 64, 170

Press, W. H., Teukolsky, S. A., Vetterling, W. T., & Flannery, B. P. 1992, Numerical recipes in FORTRAN. The art of scientific computing (Cambridge University Press)

Reinmuth, K. 1925, Astronomische Nachrichten, 225, 385

Ribeiro, V. A. R. M., Bode, M. F., Darnley, M. J., et al. 2009, *Astrophys. J.*, 703, 1955

Rivinius, T., Štefl, S., & Baade, D. 2006, *Astron. Astrophys.*, 459, 137

Robinson, K., Bode, M. F., Skopal, A., Ivison, R. J., & Meaburn, J. 1994, *Mon. Not. Roy. Astron. Soc.*, 269, 1

Roming, P. W. A., Kennedy, T. E., Mason, K. O., et al. 2005, *Space Sci. Rev.*, 120, 95

Rosino, L., Bianchini, A., & Rafanelli, P. 1982, *Astron. Astrophys.*, 108, 243

Rupen, M. P., Mioduszewski, A. J., & Sokoloski, J. L. 2008, *Astrophys. J.*, 688, 559

Rushton, M. T., Kaminsky, B., Lynch, D. K., et al. 2010, *Mon. Not. Roy. Astron. Soc.*, 401, 99

Saha, M. N. 1921, Royal Society of London Proceedings Series A, 99, 135

Sánchez-Blázquez, P., Peletier, R. F., Jiménez-Vicente, J., et al. 2006, *Mon. Not. Roy. Astron. Soc.*, 371, 703

Sarna, M. J., Ergma, E., & Gerskevits, J. 2006, ACTAA, 56, 65

Savoury, C. D. J., Littlefair, S. P., Dhillon, V. S., et al. 2011, *Mon. Not. Roy. Astron. Soc.*, 415, 2025

Schaefer, B. E. 1990, *Astrophys. J. Letters*, 355, L39

Schaefer, B. E. 2005, *Astrophys. J. Letters*, 621, L53

Schaefer, B. E. 2010, *Astrophys. J. Suppl.*, 187, 275

Schaefer, B. E. 2011, *Astrophys. J.*, 742, 112

Schaefer, B. E., Harris, B. G., Dvorak, S., Templeton, M., & Linnolt, M. 2010, IAU Circular, 9111, 1

Schaefer, B. E., Pagnotta, A., LaCluyze, A. P., et al. 2011, *Astrophys. J.*, 742, 113

Schaefer, B. E. & Ringwald, F. A. 1995, *Astrophys. J. Letters*, 447, L45

Schlegel, D. J., Finkbeiner, D. P., & Davis, M. 1998, *Astrophys. J.*, 500, 525

Sekiguchi, K., Feast, M. W., Whitelock, P. A., et al. 1988, *Mon. Not. Roy. Astron. Soc.*, 234, 281

Selvelli, P., Cassatella, A., Gilmozzi, R., & González-Riestra, R. 2008, *Astron. Astrophys.*, 492, 787

Shafter, A. W., Darnley, M. J., Hornoch, K., et al. 2011, *Astrophys. J.*, 734, 12

Shahbaz, T., Livio, M., Southwell, K. A., & Charles, P. A. 1997, *Astrophys. J. Letters*, 484, L59

Shakura, N. I. & Sunyaev, R. A. 1973, *Astron. Astrophys.*, 24, 337

Sharp, J., Kozub, R. L., Smith, M. S., Scott, J., & Lingerfelt, E. 2004, in APS Division of Nuclear Physics Meeting Abstracts, C67

Shore, S. N. 2008, in Astronomical Society of the Pacific Conference Series, Vol. 401, RS Ophiuchi (2006) and the Recurrent Nova Phenomenon, ed. A. Evans, M. F. Bode, T. J. O'Brien, & M. J. Darnley, 19

Shore, S. N., Augusteijn, T., Ederoclite, A., & Uthas, H. 2011, *Astron. Astrophys.*, 533, L8

Shore, S. N., De Gennaro Aquino, I., Schwarz, G. J., et al. 2013a, *Astron. Astrophys.*, 553, A123

Shore, S. N., Kenyon, S. J., Starrfield, S., & Sonneborn, G. 1996, *Astrophys. J.*, 456, 717

Shore, S. N., Schwarz, G. J., De Gennaro Aquino, I., et al. 2013b, *Astron. Astrophys.*, 549, A140

Snijders, M. A. J. 1987, *Astrophys. Space Sci.*, 130, 243

Sokoloski, J. L., Crotts, A. P. S., Lawrence, S., & Uthas, H. 2013, *Astrophys. J. Letters*, 770, L33

Sokoloski, J. L., Luna, G. J. M., Mukai, K., & Kenyon, S. J. 2006, *Nature*, 442, 276

Sokoloski, J. L., Rupen, M. P., & Mioduszewski, A. J. 2008, *Astrophys. J. Letters*, 685, L137

Starrfield, S. 2008, in Classical Novae, ed. M. F. Bode & A. Evans (Cambridge University Press), 39–60

Starrfield, S., Iliadis, C., Timmes, F. X., et al. 2012, Bulletin of the Astronomical Society of India, 40, 419

Sterzik, M. F. & Durisen, R. H. 1998, *Astron. Astrophys.*, 339, 95

Suleimanov, V., Meyer, F., & Meyer-Hofmeister, E. 1999, *Astron. Astrophys.*, 350, 63

Szkody, P., Sion, E. M., Gänsicke, B. T., & Howell, S. B. 2002, in Astronomical Society of the Pacific Conference Series, Vol. 261, The Physics of Cataclysmic Variables and Related Objects, ed. B. T. Gänsicke, K. Beuermann, & K. Reinsch, 21

Takei, D., Drake, J. J., Tsujimoto, M., et al. 2013, *Astrophys. J. Letters*, 769, L4

Thoroughgood, T. D., Dhillon, V. S., Littlefair, S. P., Marsh, T. R., & Smith, D. A. 2001, *Mon. Not. Roy. Astron. Soc.*, 327, 1323

Torres, S., García-Berro, E., Krzesiński, J., & Kleinman, S. J. 2013, in Astronomical Society of the Pacific Conference Series, Vol. 469, 18th European White Dwarf Workshop., ed. J. Krzesiński, G. Stachowski, P. Moskalik, & K. Bajan, 109

Townsley, D. M. 2008, in Astronomical society of the pacific conference series, Vol. 401, RS Ophiuchi (2006) and the recurrent nova phenomenon, 131–138

Townsley, D. M. & Bildsten, L. 2003, *Astrophys. J. Letters*, 596, L227

Townsley, D. M. & Bildsten, L. 2005, *Astrophys. J.*, 628, 395

Uthas, H., Knigge, C., & Steeghs, D. 2010, *Mon. Not. Roy. Astron. Soc.*, 409, 237

Vaytet, N. M. H., O'Brien, T. J., Page, K. L., et al. 2011, *Astrophys. J.*, 740, 5

Waagan, E., Linnolt, M., Bolzoni, S., et al. 2011, Central Bureau Electronic Telegrams, 2700, 1

Wade, R. A. 1987, in IAU Colloq. 95: Second Conference on Faint Blue Stars, ed. A. G. D. Philip, D. S. Hayes, & J. W. Liebert, 685–688

Walder, R., Folini, D., & Shore, S. N. 2008, *Astron. Astrophys.*, 484, L9

Walter, F. M., Battisti, A., Towers, S. E., Bond, H. E., & Stringfellow, G. S. 2012, *Pub. Astron. Soc. Pac.*, 124, 1057

Walter, M. 1867, *Mon. Not. Roy. Astron. Soc.*, 27, 316

Warner, B. 1989, in Classical Novae, ed. M. F. Bode & A. Evans (Wiley), 1–16

Warner, B. 2003, Cataclysmic Variable Stars, p. 592. ISBN 052154209X. Cambridge, UK: Cambridge University Press.

Webbink, R. F. 1984, *Astrophys. J.*, 277, 355

Webbink, R. F., Livio, M., Truran, J. W., & Orio, M. 1987, *Astrophys. J.*, 314, 653

Williams, R. E. 1990, in Lecture Notes in Physics, Vol. 369, IAU Colloq. 122: Physics of Classical Novae, ed. A. Cassatella & R. Viotti, 215

Williams, R. E., Hamuy, M., Phillips, M. M., et al. 1991, *Astrophys. J.*, 376, 721

Williams, R. E., Sparks, W. M., Gallagher, J. S., et al. 1981, *Astrophys. J.*, 251, 221

Woodward, C. E., Helton, L. A., Evans, A., & van Loon, J. T. 2008, in Astronomical Society of the Pacific Conference Series, ed. A. Evans, M. F. Bode, T. J. O'Brien, & M. J. Darnley, Vol. 401, 260

Worters, H. L., Eyres, S. P. S., Rushton, M. T., & Schaefer, B. 2010, IAU Circular, 9114, 1

Yamanaka, M., Uemura, M., Kawabata, K. S., et al. 2010, *Pub. Astron. Soc. Japan*, 62, L37

Yaron, O., Prialnik, D., Shara, M. M., & Kovetz, A. 2005, *Astrophys. J.*, 623, 398

Zamanov, R. K. 2011, Bulgarian Astronomical Journal, 17, 59

Zamanov, R. K., Boeva, S., Bachev, R., et al. 2010, *Mon. Not. Roy. Astron. Soc.*, 404, 381

Chapter 6

Publications